

**REPUBLIC OF TURKEY  
YILDIZ TECHNICAL UNIVERSITY  
GRADUATE SCHOOL OF NATURAL AND APPLIED SCIENCES**

**A HIGH ACCURATE POSITIONING AND MANIPULATION  
TECHNIQUE FOR UNTETHERED MICROROBOTS**

**ALİ ANIL DEMİRÇALI**

**MSc. THESIS  
DEPARTMENT OF MECHATRONICS ENGINEERING  
PROGRAM OF MECHATRONICS ENGINEERING**

**ADVISER  
ASSIST. PROF. DR. HÜSEYİN ÜVET**

**İSTANBUL, 2017**

**REPUBLIC OF TURKEY**  
**YILDIZ TECHNICAL UNIVERSITY**  
**GRADUATE SCHOOL OF NATURAL AND APPLIED SCIENCES**

**A HIGH ACCURATE POSITIONING AND MANIPULATION  
TECHNIQUE FOR UNTETHERED MICROROBOTS**

A thesis submitted by Ali Anıl DEMİRÇALI in partial fulfillment of the requirements for the degree of **MASTER OF SCIENCE** is approved by the committee on 23/05/2017 in Department of Mechatronics Engineering, Mechatronics Engineering Program.

**Thesis Adviser**

Assist. Prof. Dr. Hüseyin ÜVET  
Yıldız Technical University

**Approved By the Examining Committee**

Assist. Prof. Dr. Huseyin UVET  
Yıldız Technical University

Prof. Dr. Haydar LIVATYALI  
Yıldız Technical University

Prof. Dr. Ali KOSAR  
Sabanci University



This study was supported by the project number 113E584 of the Scientific and Technological Research Council of Turkey, TÜBİTAK 1001.

## ACKNOWLEDGEMENTS

---

I wish to acknowledge the following people for their role in the completion of this thesis: My parents, Kadriye and Arif ENGİN DEMİRÇALI for always supporting my choices in life, My supervisor, Ass. Prof. Dr Hüseyin ÜVET and co-adviser Ass. Prof. Dr. Kadir ERKAN for their guidance, constructive proofreading, Prof. Dr. Ali Koşar for giving equipment used in experimental works and helpfulness, My colleague Eng. Tunç Köse for his perseverance and benevolence, My grandfather Selami Açıkgöz and uncle Abdullah Akkızal for their place in my heart forever. Thank you for helping me produce a MSc. thesis I can be proud of.

May, 2017

Ali Anıl DEMİRÇALI

## TABLE OF CONTENTS

---

	Page
LIST OF SYMBOLS .....	vii
LIST OF FIGURES .....	viii
LIST OF TABLES .....	xii
ABSTRACT.....	xiv
ÖZET .....	xvi
CHAPTER 1	
INTRODUCTION .....	1
1.1 Literature Review.....	1
1.2 Objective of the Thesis .....	3
1.3 Hypothesis.....	3
CHAPTER 2	
MICROROBOT DESIGN, SIMULATION AND PRODUCTION.....	5
2.1 Microrobot Material Choice .....	5
2.2 Microrobot Design .....	6
2.3 Microrobot Mathematical Modeling.....	9
2.4 Microrobot Experimental Setup Selection.....	11
2.4.1 Mesh Selection .....	13
2.4.2 CFD Analysis .....	13
2.4.3 Lifting Magnet Selection for Required Force.....	15
2.4.4 Experimental Setup with Equipments .....	17
2.5 Micro Stage Control Interface .....	18
2.6 Micro Robot Production .....	21
2.6.1 First Prototype Production.....	21
2.6.2 Processing Of Surface Coating With Flow Nickel Plating Method.....	31
2.6.3 Micro Fluid Type Production and Microrobot Integration.....	41
2.6.4 Completion of Micro-fluid Chip Design with Plasma Process.....	48
2.6.5 Permanent Magnet Surface Coating .....	50

2.6.6	Microrobot Fabrication .....	51
CHAPTER 3		
	FEM ANALYSIS .....	53
3.1	Definiation of Analysis .....	53
3.2	Z-axis Lifting Magnet Force Calculation via COMSOL.....	55
3.3	Frequency Characteristic .....	57
3.4	Head Tilt Analysis .....	59
CHAPTER 4		
	EXPERIMENTAL STUDIES .....	62
4.1	Levitation characterization.....	63
4.2	Phase difference characterization .....	65
4.3	Pre-defined Trajectory Tracking.....	66
4.4	Head Bending Reaction .....	68
CHAPTER 5		
	DISCUSSION and CONCLUSION .....	69
CHAPTER 6		
	FUTURE WORKS .....	72
	REFERENCES .....	73
	CURRICULUM VITAE.....	75

## LIST OF SYMBOLS

---

$F_B$	Buoyant force
$A_x$	Cross sectional area of X-axis
$A_y$	Cross sectional area of Y-axis
$A_z$	Cross sectional area of Z-axis
$F_{g,x}$	Diamagnetic force X-axis component
$F_{g,y}$	Diamagnetic force Y-axis component
$F_{g,z}$	Diamagnetic force Z-axis component
$c_d$	Drag coefficient
$F_{D,x}$	Drag force X-axis component
$F_{D,y}$	Drag force Y-axis component
$F_{D,z}$	Drag force Z-axis component
$\rho_f$	Fluid density
$g$	Gravitational acceleration
$F_r$	Gravitational force
$B$	Inner Diameter of Microrobot
$H$	Magnetic field strength
$B$	Magnetic flux density
$F_{m,x}$	Magnetic force X-axis component
$F_{m,y}$	Magnetic force Y-axis component
$F_{m,z}$	Magnetic force Z-axis component
$\chi$	Magnetic insulation coefficient
$M$	Magnetization vector
$A$	Outer Diameter of Microrobot
$\mu_r$	Relative permeability
$\rho_r$	Robot density
$m_r$	Robot mass
$V_r$	Robot volume
$C$	Thickness of the Microrobot
$v$	Velocity
$V_p$	Volume of a particle

## LIST OF FIGURES

---

	Page
Figure 2.1	Materials and dimensions used in the experimental setup are shown. Ring type lifter magnet, microrobot and its permanent magnet are aligned in the same center with lifter magnet while pyrolytic graphite is placed on the bottom surface. .... 6
Figure 2.2	The stabilizer magnet (A) has properties of neodymium (N52 grade) with 1.43 Tesla. To transport living cells in a liquid environment, the microrobot has symmetrical 4 half-moon shape carrier slots and 1 central magnet hole for the stabilizer magnet. The Su-8 polymer used as microrobot material which can be well suits for future nano-fabrication process has a a thickness of 200 $\mu$ m. .... 6
Figure 2.3	The effect of pyrolytic graphite thickness varying in 1-10 mm on diamagnetic force was calculated. Since the diamagnetic force behaves more linearly in the range of 3-7 mm, material thickness in this range can be selected to get better levitation performance. .... 9
Figure 2.4	According to the position of the lifting magnet on the Z-axis, the mechanical contactless movement of the micro-robot on pyrolytic graphite is shown schematically. <b>F<sub>m</sub></b> : Lifting magnet force, <b>F<sub>dia</sub></b> : Diamagnet force, <b>F<sub>B</sub></b> : Buoyant force, <b>F<sub>r</sub></b> : Gravitational force and <b>F<sub>D</sub></b> : Drag Force is shown..... 10
Figure 2.5	The mesh structure used in FSI analysis is shown. The microrobot is placed in the water-filled container with 4x4x2 mm outer surface. The effects of different surface stress force, <b>F<sub>D</sub></b> , acting on a microrobot surface are calculated. For a more accurate and precise result, the microrobot has been assigned a minimum width of 0.2 mm, and a thickness of 2 times the thickness of a max 0.4 mm mesh. A maximum of 0.5 mm was selected for the container. It is also applied to the system at regular refinement level 2. It can be seen that the mesh-size values should be very close and the direct solver method should be used to have more accurate results. .... 13
Figure 2.6	Stresses on the robot surface and speed lines around it are shown. When looking at the speed lines, values of 0-7 mm/s are represented by the upper bar. Light blue-green colors were observed more intensively and a speed of 3-4 mm/s was observed. When the effect on the robot is examined, it is seen that the lower bar is 16.6-348 Pa and the feature is more at corner and intersection points. The reason is that the surface area, where in the corner is smaller, increasing the pressure force. At the same time, the different formation of the intersection point of su8-magnet hardness affects the



	homogeneous distribution in stresses. So, intersection point of su8-magnet has more stress.....	14
Figure 2.7	Microrobot behavior was observed as a result of different stresses and velocities due to Time-Dependent analysis. As can be seen, a constant <b>cd</b> coefficient characteristic is obtained after a certain period of time. This value is calculated as <b>cd</b> = 7.6811; (3), <b>FD</b> will change depending on the speed. <b>FD, max</b> = 0.125 $\mu$ N when the robot speed is selected as $\pm 2$ mm / s, depending on the micro stage speed to be used mostly in magnetic levitation setup. At the same time, it is seen that the value of the force that varies parabolically in this range is negligible because it is about 1/1000 of the diamagnetic force. ....	14
Figure 2.8	According to the simulation results, it is calculated that the force generated for the maximum stage speed of 5 mm/s is 0.781 $\mu$ N .....	15
Figure 2.9	The effect of the change of the dimensions of the ring-type lifting magnet is shown. The lifting magnet, which is a more linear characteristic in the range of 25-45 mm according to graph, exhibits exponential behavior according to its size outside this range.....	16
Figure 2.10	The magnetic force characteristic of the selected lifting magnet and pyrolytic graphite is a phenomenon that exponentially decreases as the microrobot moves away as expected. As a result of the selection criteria, <b>Fnet</b> on micro robot was determined as 16.04 $\mu$ N according to Table 2. The result that the micro-robot could be levite in the range of 50-60 mm according to lifting magnet-pyrolytic graphite distance in the X-axis has emerged.....	17
Figure 2.11	The control of the Micro Stage, which performs the motion as a ring magnet 3 axis linear, was realized through an interface created with C#. Camera image is transferred on the same interface. The reading of the data of the laser distance sensor is taken through the laser's own interface.....	18
Figure 2.12	Relationship between voltage-speed of motor. ....	19
Figure 2.13	Connection of Stage Interface-1 .....	19
Figure 2.14	Manuel Control Interface of Microrobot via Computer .....	20
Figure 2.15	Whole system interface including with camre panel, image processing menu, manuel and button control properties .....	20
Figure 2.16	Microrobot first prototype design.....	22
Figure 2.17	Slag Layer and Roughness Produced on the Surface of a Cutting Particle by Carbon Laser.....	23
Figure 2.18	First Nickel-Based Micro-Robot Arm Produced by Laser Cutting.....	24
Figure 2.19	First Nickel-Based Micro-Robot Arm Deformations.....	24
Figure 2.20	Optimal Cutting Parameters Nickel-Based Micro-Robot Arm Produced by Laser Cutting .....	25
Figure 2.21	Glazing process to reduce burrs and cavities of Nickel-based Micro-robot arm produced by laser cutting .....	26
Figure 2.22	An image belonging to the micro robotic after grinding.....	27
Figure 2.23	Micromechanical machining precision and micro-finger milling pocket with a diameter of 6mm - 200 microns.....	28
Figure 2.24	Detailed images taken after turning the micro-robot arm by processing the polymer material fixed with metal layer adhesive in order to balance during CNC machining .....	29
Figure 2.25	Detailed images taken after withdrawing with acetone from the fixed micro-robot wrist.....	30

Figure 2.26	Detailed views of the final state of the micro robot arm obtained by machining with CNC in micro precision.....	30
Figure 2.27	Nickel Plating on Polymer Material.....	33
Figure 2.28	Preparation of Diluted HCl Solvent for Polymeric Material Cleaning .....	33
Figure 2.29	Preparation of Diluted HCl Solvent for Polymeric Material Cleaning .....	34
Figure 2.30	Weighing of Sensitive Level Chemicals .....	34
Figure 2.31	PdCl <sub>2</sub> and SnCl <sub>2</sub> solutions in a magnetic stirrer.....	35
Figure 2.32	PdCl <sub>2</sub> and SnCl <sub>2</sub> solubles after magnetic stirring and acid addition.....	35
Figure 2.33	Pictures of sodium hypophosphite and nickel sulfate salt.....	36
Figure 2.34	Measurement of the pH of the current-free nickel-plating bath prepared by pHmeter .....	37
Figure 2.35	Coating of the polymer micro-robot arm in a current-free nickel plating chamber at 80 ° C .....	37
Figure 2.36	Images obtained from the front and back surfaces of the polymer microrobot after the currentless nickel plating process.....	38
Figure 2.37	Products that occur together with the formation of the plasma phase.....	39
Figure 2.38	Changes that can be made by plasma processing on the surface. (A) Material scraping from the surface, (b) Adding material to the surface, (c) Changing the physical and chemical properties of the surface.....	39
Figure 2.39	Polypropylene chemical structure .....	40
Figure 2.40	Chemical structures formed on polypropylene surface after oxygen plasma treatment .....	40
Figure 2.41	After oxygen etch with plasma, the pore-free etched surface is covered..	40
Figure 2.42	Diagram showing the process of extracting the desired patterns onto the PDMS using the replica method [21] .....	41
Figure 2.43	The functions of the masks pattern processing process[23-24] .....	42
Figure 2.44	Drawing file prepared for mask writing .....	42
Figure 2.45	Spin coating working principle[25].....	43
Figure 2.46	Spin coater used in coating of photoresist on wafer in Laboratory.....	43
Figure 2.47	Process of obtaining desired patterns after Develop process .....	44
Figure 2.48	Weighing of the curing agent with PDMS at a ratio of 10: 1.....	45
Figure 2.49	Mixing process to homogeneously disperse the curing agent in PDMS... ..	45
Figure 2.50	Emptying the air inside the PDMS with the desiccator.....	46
Figure 2.51	Image of the solution from the desiccator .....	46
Figure 2.52	Pouring of PDMS prepared on master mold placed in Petri dish .....	47
Figure 2.53	Placing the Petri dish in the oven .....	47
Figure 2.54	Sliding glass with PDMS on which patterns are processed .....	48
Figure 2.55	Plasma apparatus used for bonding PDMS with glass slide .....	48
Figure 2.56	Covalent bond between PDMS and glass after plasma treatment.....	49
Figure 2.57	Image of completed microfluidic chip .....	50
Figure 2.58	Microscopic image of microfluidic chip channels .....	50
Figure 2.59	FTIR spectrum of magnet coated with PDA. Peak between wavelength of 500-1650 cm <sup>-1</sup> indicates N-H vibrations and peak between wavelength of 3200-3600 cm <sup>-1</sup> indicates hydroxyl groups in the structure. This proves successful coating of magnet surface. ....	51
Figure 3.1	Fabrication process of microrobot.....	52
Figure 3.2	The effect of levitation height and lifting magnet distance on net force is calculated. The flux density in the magnet is shown by the [T] unit with the bar on the left side. The distributions of the flux density in the lifting magnet and robot arm are given in detail to the right. The density of the magnets is	

in the range of 0.7-0.9 T in the corners and middle regions of the magnets themselves. The force lines are frequent in that region because of being more dense in the corner areas. Since the magnet poles are placed in N-S-N-S, it is shown that the corresponding force lines are upwards in the Z-axis..... 54

Figure 3.3 According to the analysis made, force graphs are obtained on the micro robot z-axis in the range of 54-58 mm. As expected, a parabolic characteristic has been achieved and the force decreases as the distance increases. At the same time, the Levitation distance in the X-axis showed a decreasing characteristic as the distance increased and a rupture of 0.25-0.3 mm was observed depending on the lifting magnet distance..... 55

Figure 3.4 According to the parabolic surface graph obtained from the analysis made, when the "Lift Magnet Distance" indicated by Y axis and the "Levitation Height" indicated by X axis increase, the net force generated on the microrobot is reduced. Max: 51.89  $\mu$ N and min: 8.11  $\mu$ N force values were calculate ..... 56

Figure 3.5 It has been shown that the X and Y axis forces are in the 1/1000 ratio according to the force value generated in the Z-axis. Since the acting forces on the X and Y axes of the microrobot are very small (0.06  $\mu$ N), there is no effect on it during the Z-axis levitation. .... 56

Figure 3.6 Exerted forces on a Z-axis..... 58

Figure 3.7 Linearization of forces induced by vertical distance change ..... 58

Figure 3.8 (a) Positive angular orientation, (b) Constant, (c) Negative angular orientation. All combinations related to the three cases are calculated parametrically. As can be seen, the flux density is increased in the edge direction where the lifting magnet bends and the force lines become more intense. As expected, the force lines are not symmetrical when compared to (b) in the inclined state. By this feature, it is desired to prevent head tilting by acting on undesired torque in negative direction in microrobot..... 59

Figure 3.9 I. shows the torque changes in (a) Y axis, (b) Z axis. As expected, a symmetrical and linear surface characteristic with respect to the 0° axis line is obtained. Delay distance shows the effects of misalignment, and has the effect of increasing torque at the same head tilt. Also, I. (b) torque change on Z axis is shown. II. (a) on the Y axis, (b) on the Z axis. When the micro-robot receives a positive angle value of 8°, lifting magnets are calculated to be -1.96°, that is, when a negative angle is given, the robotic-affecting torques are 0 for each axis. The corresponding surface characteristic is the same as when the micro-robot is angled, and the torque values are close to each other..... 60

Figure 3.10 The control of the Micro Stage, which performs the motion as a ring magnet 3 axis linear, was realized through an interface created with C#. Camera image is transferred on the same interface. The reading of the data of the laser distance sensor is taken through the laser's own interface. .... 63

Figure 4.1 The experiment was observed by recording the position data with the laser distance sensor in each movement step. The microrobot has been shown to operate at a maximum stabilization level of 333  $\mu$ m in the current system. Subsequently, the resultant force acting on the microrobot was acting in the upward direction, indicating that the robot departed from the stable region and moved upwards under the influence of the magnetic force. .... 64

Figure 4.2	Prior to the critical region where the lifter magnet effect increased, the microrobot showed a levitation elevation with linear characteristics similar to the simulation results.....	64
Figure 4.3	Depending on the microstage speed change, the delay is shown. The red line belongs to the laser which is sent from the center of the lifter magnet. Acceleration has been shown to increase with delay as expected.....	65
Figure 4.4	At higher velocities of about 1.4mm / s, the phase difference is characterized by an exponential increasing trend and at lower speeds with linearized phase difference characterization as expected. It is obvious that the phase difference falls below 150 $\mu$ m as the same linear change is likely to continue even at small speeds of 0.5mm / s. This is an indication that non-delayed positioning can be performed by neglecting the phase difference at the speed requirements of the nanometer range, which will be needed especially in lab-on-a-chip applications. ....	66
Figure 4.5	The sinusoidal and circular orbit levitation elevation has been successfully tracked to remain constant. A) shows the sinusoidal trajectory followed by the signal input given as amplitude $A = 4$ mm and $t = \pi/2$ . B) a circular orbit with a radius of 2 mm was followed.....	67
Figure 4.6	The robot has started to move at the same height from the point of the block. Then it is raised upwards by being levitated on the Z axis precisely. By passing over the micro robot as parallel to the obstacle; At point D, it is lowered again in the Z axis.....	67
Figure 4.7	The cause of the head tilt reaction is to suspend the directional changes of the vector field forces acting on the microrobot. The head tilt angle is a parameter proportional to the phase difference. The increase in phase difference also causes an increase in head tilt angle. As can be seen in Figure 4., in the experimental studies performed, the head tilt angle of 7 $^{\circ}$ is displayed.....	68

## LIST OF TABLES

---

	Page
Table 2.1 System Model Parameters .....	7
Table 2.2 Calculated parameters in equ. (20-22).....	12
Table 2.3 Constant Force Values .....	15
Table 2.4 Optimum cut parameters.....	25
Table 2.5 Ratios of Components Used in Solution During Bath Preparation .....	36
Table 3.1 Forces action on Microrobot z-axis .....	57

## ABSTRACT

---

# A HIGH ACCURATE POSITIONING AND MANIPULATION TECHNIQUE FOR UNTETHERED MICROROBOT

Ali Anıl DEMİRÇALI

Department of Mechatronics Engineering

MSc. Thesis

Adviser: Assist.Prof. Dr. Hüseyin ÜVET

In this study, a microrobot manipulation technique with high precision positional ability to move in a liquid environment with diamagnetic levitation has been presented. Untethered manipulation of microrobots by means of externally applied magnetic forces has been emerging as a promising field of research, particularly due to its potential for medical and biological applications. Purpose of the presented method is to eliminate friction force between surface of the substrate and microrobot so that a high accuracy motion can be achieved. With the proposed method, precise (nano) positioning of levitated microrobot on the pyrolytic graphite is demonstrated. The applicability of the proposed technique has been successfully proved by supporting it with the mathematical model, FEM analysis and experimental results. The magnetic force, which is required to levitate microrobot at a stabilized position, was determined. According to the varying force value depending on the position of the lifter magnet on z-axis, the levitation height of microrobot in the liquid was determined by FEM analysis and also shown by the experimental results. According to experimental results, the microrobot can follow to desired trajectory with high accuracy at variable speeds and levitation heights. Due to the positioning accuracy at nano-level, desired locomotion can be achieved in pre-specified trajectories (sinusoidal or circular). Instead of using strong electromagnets or bigger permanent magnets, microrobots can move in 3-dimensional space in a liquid environment with the presented manipulation technique.

**Keywords:** Diamagnetic levitation, FEM analysis, Microorobot, Lab-on-a-chip



---

**YILDIZ TECHNICAL UNIVERSITY**  
**GRADUATE SCHOOL OF NATURAL AND APPLIED SCIENCES**

---

**MEKANİK TEMASSIZ MİKRO ROBOT İÇİN YÜKSEK  
DOĞRULUKLU KONUMLANDIRMA VE MANİPÜLASYON  
TEKNIĞİ**

Ali Anıl DEMİRÇALI

Mekatronik Mühendisliği Anabilim Dalı

Yüksek Lisans Tezi

Tez Danışmanı: Yrd.Doç. Dr. Hüseyin ÜVET

Bu çalışmada, diamagnetic levitasyonla sıvı ortamda yüksek hassasiyet pozisyonel hareket kabiliyeti olan bir mikrodobot manipülasyon tekniği sunulmuştur. Mikro robotların, harici olarak uygulanan manyetik kuvvetler aracılığıyla bağımsız manipülasyonu, özellikle tıbbi ve biyolojik uygulamalar için potansiyeli nedeniyle umut verici bir araştırma alanı olarak ortaya çıkmaktadır. Sunulan yöntemin amacı, yüksek hassasiyetli bir hareket elde etmek için alt tabaka yüzeyi ile mikro çubuk arasındaki sürtünme kuvvetini ortadan kaldırmaktır. Önerilen yöntemle, pirolitik grafit üzerinde levitaded mikrodobanın hassas (nano) konumlandırılması gösterilmiştir. Önerilen tekniğin uygulanabilirliği, matematiksel model, FEM analizi ve deney sonuçları ile desteklenerek başarıyla kanıtlanmıştır. Mikro robotu dengelenmiş bir konumda havadan geçirmek için gereken manyetik kuvvet belirlendi. Z eksenindeki kaldırıcı mıknatısın konumuna bağlı olarak değişen kuvvet değerine göre, sıvı içindeki mikro roobotun havaya kaldırma yüksekliği FEM analizi ile belirlendi ve ayrıca deney sonuçları gösterildi. Deney sonuçlarına göre, mikrodobot, değişken hızlarda ve havatlama yüksekliklerinde yüksek doğrulukla istenen yörünge izleyebilir. Nano düzeydeki konumlandırma hassasiyeti sayesinde, önceden belirlenmiş yörüngelerde (sinüzoidal veya dairesel) istenilen hareket elde edilebilir. Güçlü elektromıknatıslar veya daha büyük daimi mıknatıslar kullanmak yerine, sunulan mikro manipülasyon tekniği ile mikro platformlar sıvı bir ortamda 3 boyutlu uzayda hareket edebilirler.

**Anahtar Kelimeler :** Diyamanyetik levitasyon, FEM analizi, Mikro robot, Lab-on-a-chip





### INTRODUCTION

#### 1.1 Literature Review

Untethered manipulation and magnetically actuated microrobots are used in mostly biological and medical applications such as cell manipulation, drug delivery, diagnostics, biosensing, chemical synthesis, biopsy, microparticle transport, etc., with minimal damage to the desired site [1-6]. Furthermore, many of them have recently been developed for in vitro applications including helical swimmers, microgrippers, and soft microparticles [7-9]. In the liquid environments, their fields of application are especially in biomedical engineering for better micro object manipulation without physical linkage or connections [10-12]. When considering the effect of liquid conditions, the magnetic force to be applied and the precision of motion using microrobots in such applications can be more advantageous than other applications [2].

The micro level robot has been designed, it is seen that due to the diminishing dimensions, the flow regime of the liquid environment may change. At this level, the fact that the environment exhibits laminar flow characterization causes  $Re$  (Reynolds Number) not to be ignored. Arai and his team considered the effects of Reynolds on microrobot size reduction in a microfluidic environment [13]. Nelson and his team have worked on "sub-mm sized untethered microrobots inside body fluids with external magnetic fields". In addition to the Reynolds effects, the team described the drag force effects in the microfluidics during the movement of the robot [14]. Moreover, Nelson and his team have performed precise position control with 3 electromagnets. In the work they produce by the inspiration of bacterial manipulation, they have observed drag force and Low-Reynolds effects [7]. Metin Sitti and his team also performed microrobot control in a

contactless manner, and errors in movement accuracy were observed. These errors are due to the experimental uncertainty in the measured values of the friction coefficients and the adhesive force [15]. Khamesee and his team have done a precise position control with a model of friction force. [16] However, there are problems with control sensitivity due to frictional force with the surface of the microrobot. Arai and his team have achieved successful results by applying ultrasonic vibrations [17]. However, the ultrasonic tactics also reduce positioning accuracy because they can move in other objects in the environment, sizes are varying in few microns. Pelrine and his team have worked on microrobot swarm structure using diamagnetic levitation [18], although in many microrobot studies large electromagnets or 4 permanent magnets are preferred on a single microrobot. Because the study was not done in a fluidic environment, the viscous effects of the fluid were not observed. In our study, diamagnetic levitation is applied to the microrobot in the fluid and 2 permanent magnets are used as stabilizer and lifter. In this regard, the new manipulation technique applied contributes to the literature.

The aim of the proposed new method is to improve the microrobot manipulation technique, which can be driven in a liquid with high accuracy by detaching microrobots relation from the bottom surface of the liquid medium container. No huge electromagnets or large permanent magnets are needed as because of the fact that the friction force between the bottom surface of the container and microrobot is removed. By using pyrolytic graphite and taking advantage of the diamagnetic forces, the microrobot can have more stable motion characteristic. Thus, nano-accurate manipulations can be performed and a precise control can be achieved.

For a nano-accurate motion, drag force must be calculated [7, 14]. The drag force coefficient expressions may be seen in formulas that can be simplified in the corresponding axis when the geometric structure is spherical, disk-shaped, etc., [7, 14, 15, 19]. However, the proposed solutions and analysis techniques are not presented for different geometries or more complex geometric structures. For this reason, our solution method for the structures with complex geometry is calculated by CFD (Computational Fluid Dynamics) analysis and the drag force effect is shown. Motion characteristics, along with the possible movements on the X-Y-Z axes, have been demonstrated with 6-axis control analyzes by applying different scenarios. All cases were handled separately in the analyzes and the changes on the microrobot motion were given.

## **1.2 Objective of the Thesis**

The aim of the thesis work is to develop a new manipulation technique on the production and micro-contactless high precision control of the microrobot commonly used in the health sector. The micro-robot targeted for production will be able to move mechanically without contact, working under the influence of magnetic and diamagnetic field. The lack of mechanical contact with the surface will reduce the energy requirement, allowing the system to shrink in size. As the energy requirement is low, the size of the magnets to be used together will be reduced, so that the use of large electromagnets and permanent magnets will not be necessary as in other applications. The micro robot arm has been designed for studies such as single cell operations (cell-cloning, artificial-fertilization, artificial-skin) or single cell analyzes (cancer, anemia) which are studied intensively in medical and biomedical fields. It is optimized to allow placement in lab-on-a-chip (microchips with microfluidic channels and chambers). For the first time in the literature, micro-fluid precision position and trajectory control have been studied in a microfluidic liquid by levitation force, diamagnetic force and mechanical non-contact manipulation technique. According to analyzes made for more stable and vibration-free operation, a new levitate technique was studied on the base surface using pyrolytic graphite. Thus, the interaction of the micro-robot arm with the surface in the microfluidic chip is cut off and the friction is removed. Instead of spending large electromagnets and high power consumption, as in other works, the magnitude of the magnet has been reduced and friction has been reduced to a minimum, leaving no energy to dissipate. Developed and developing; Feedback algorithms, control methods and analyzes will be an innovative solution to medical and biomedical fields.

## **1.3 Hypothesis**

The unique value of the thesis work is to provide a new solution to the human health and treatment methods in the related fields, starting from the active use of increasing medical and biomedical applications. In addition, with the new manipulation technique used, cell operations will be more easily performed thanks to the microrobot, which provides more stable and precise levitation on the pyrolytic graphite. However, the smaller size of the magnets used for the system with lower energy requirements is a key feature. Thanks to this technique, which is used in the literature firstly, the friction force between the microrobot surface and the surface is removed to provide mechanical non-contact

movement. More precise (nano) control is provided as a result of these properties obtained. Thus, various motion trajectories such as circumferential and sinusoidal were followed and micro-robot precise position control was successfully performed. By virtue of the design minimizing the drag force effect in the environment, the viscous effects of the medium are least affected.



### MICROROBOT DESIGN, SIMULATION AND PRODUCTION

#### 2.1 Micro Robot Material Choice

The precise calculation of a magnetic force acting on a microrobot is necessary to determine its levitation characteristic. This calculation process can be done in 3 ways as theoretically, experimentally or numerically (Finite Element Method, FEM). A FEM analysis, that we used COMSOL<sup>®</sup> ver 5.2, provides an advantage in the implementation of different case studies. Before starting the full FEM analysis, the choice of which material to use and the choice of its dimension are important factors. The entire experimental setup is shown in Figure 2.1. According to our proposed experimental setup to be used in COMSOL<sup>®</sup> program, the microrobot levitation system, which can be moved non-mechanical contact under the exited of magnetic and diamagnetic forces, was tested in a liquid medium (DI Water). A diamagnetic pyrolytic graphite is placed on the bottom surface of a DI water container. On the graphite surface, the su-8 polymer-based microrobot with a permanent N-52 grade magnet at its center was placed. The lifter magnet was selected as a ring type considering the future real experimental work to utilize laser or vision sensors to create a position feedback control mechanism. The lifter magnet was positioned above z-axis of the container.

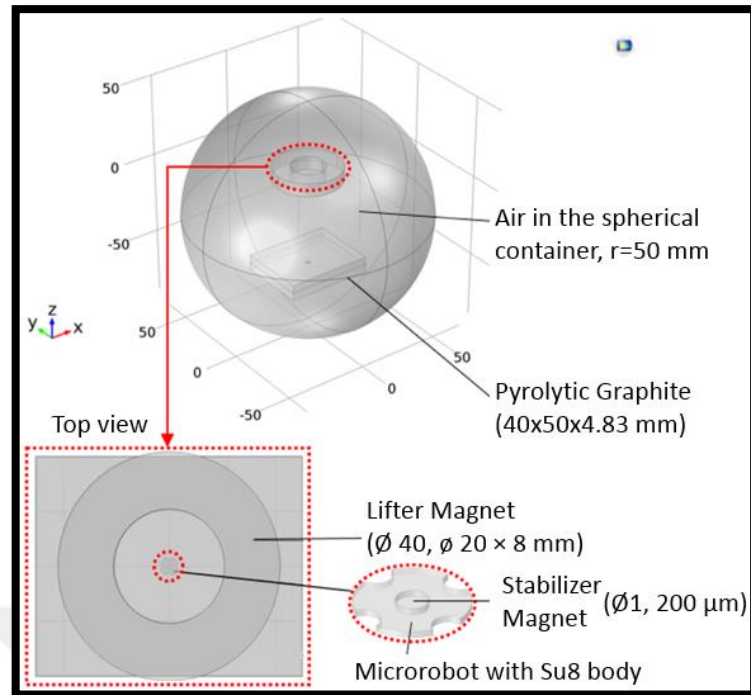


Figure 2.1 Materials and dimensions used in the experimental setup are shown. Ring type lifter magnet, microrobot and its permanent magnet are aligned in the same center with lifter magnet while pyrolytic graphite is placed on the bottom surface.

## 2.2 Microrobot Design

After selection of the materials for each simulation object, the microrobot was designed according to target application area such as cell manipulation, diagnostic etc. Thus, in this study, we choose the microrobot with four carrier slots (Figure 2) for effective cell transfer. Because of its symmetrical nature, it can be more suitable for such applications. A permanent magnet with a diameter of 1 mm, and a thickness of 0.2 mm was placed at center of the microrobot, that has an outer diameter of 3 mm, to maintain desired levitation Figure 2.2

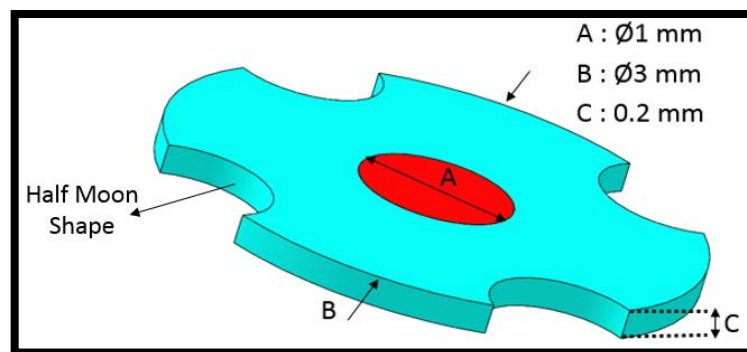


Figure 2.2 The stabilizer magnet (A) has properties of neodymium (N52 grade) with 1.43 Tesla. To transport living cells in a liquid environment, the microrobot has

symmetrical 4 half-moon shape carrier slots and 1 central magnet hole for the stabilizer magnet. The Su-8 polymer used as microrobot material which can be well suits for future nano-fabrication process has a a thickness of 200 $\mu$ m.

According to the designed microrobot in SOLIDWORKS 3D program, the pyrolytic graphite thickness and the size of the ring type lifting magnet are required. Since, the force which is created by each magnets are very depending on the sizes itself. Firstly, graphite thickness and magnet dimensions shall be determined. According to the results, regions with more linear behavior are preferred and more stable behavior can be obtained. In addition, it is appropriate to choose linear behavior characteristics so that the system is less affected by possible external factors. Model parameters are given in Table

Table 2.1 System Model Parameters

Symbol	Quantity	Units
$F_B$	Buoyant force	N
$F_g$	Diamagnetic force	N
$F_D$	Drag force	N
$F_m$	Magnetic force	N
$F_r$	Gravitational force	N
$B$	Magnetic flux density	T
$H$	Magnetic field strength	A/m
$M$	Magnetization vector	A/m
$\chi$	Magnetic insulation coefficient	-
$\mu_r$	Relative permeability	-
$V_p$	Volume of a particle	$m^3$
$m_r$	Robot mass	kg
$g$	Gravitational acceleration	$m/s^2$
$V_r$	Robot volume	$m^3$
$\rho_f$	Fluid density	$kg/m^3$
$\rho_r$	Robot density	$kg/m^3$

To calculate the diamagnetic force, the material used can be assumed to be uniformly distributed. Thus, the force of per unit volume  $dv$ , in the magnetic field of the floating magnet can be expressed,



$$d\mathbf{f} = \mathbf{M}_d(\nabla\mathbf{B})d\mathbf{v} \quad (2.1)$$

where  $M_d$  is the magnetization at the location of the diamagnetic material in the magnetic field of the floating magnet respectively. Since the  $\chi_d$  value is very small,  $M_d$  can be expressed as,

$$\mathbf{M}_d = \frac{\chi_d}{\mu_0} \mathbf{B} \quad (2.2)$$

The expression (2.1) is substituted to (2.2) and the integral can be taken for all the diamagnetic material. In this way, the force between the diamagnetic material and the permanent magnet can be calculated as integral form as follows:

$$F_{d,x} = \frac{\chi_d}{\mu_0} \iiint_V \left( B_x \frac{\partial B_x}{\partial x} + B_y \frac{\partial B_y}{\partial x} + B_z \frac{\partial B_z}{\partial x} \right) d\mathbf{v} = \frac{\chi_d}{2\mu_0} \iiint_V \left( \frac{\partial \|\mathbf{B}\|^2}{\partial x} \right) d\mathbf{v} \quad (2.3)$$

$$F_{d,y} = \frac{\chi_d}{\mu_0} \iiint_V \left( B_x \frac{\partial B_x}{\partial y} + B_y \frac{\partial B_y}{\partial y} + B_z \frac{\partial B_z}{\partial y} \right) d\mathbf{v} = \frac{\chi_d}{2\mu_0} \iiint_V \left( \frac{\partial \|\mathbf{B}\|^2}{\partial y} \right) d\mathbf{v} \quad (2.4)$$

$$F_{d,z} = \frac{\chi_d}{\mu_0} \iiint_V \left( B_x \frac{\partial B_x}{\partial z} + B_y \frac{\partial B_y}{\partial z} + B_z \frac{\partial B_z}{\partial z} \right) d\mathbf{v} = \frac{\chi_d}{2\mu_0} \iiint_V \left( \frac{\partial \|\mathbf{B}\|^2}{\partial z} \right) d\mathbf{v} \quad (2.5)$$

If the diamagnetic force components in X, Y, Z directions are simplified according to Ostrogradsky's divergence law [20] as  $F_{d,x}$ ,  $F_{d,y}$ ,  $F_{d,z}$ ,

$$F_{d,x} = \frac{\chi_d}{\mu_0} \oint_S \|\mathbf{B}\|^2 n_x ds \quad (2.6)$$

$$F_{d,y} = \frac{\chi_d}{\mu_0} \oint_S \|\mathbf{B}\|^2 n_y ds \quad (2.7)$$

$$F_{d,z} = \frac{\chi_d}{\mu_0} \oint_S \|\mathbf{B}\|^2 n_z ds \quad (2.8)$$

For a microrobot, whose dimensions are held constant, sizes of the lifter magnet and the pyrolytic graphite used are important because, due to their size effects, the magnetic and diamagnetic forces exerted on the microrobot may change. Before starting to model experimental setup in COMSOL<sup>®</sup>, the dimensions of the lifter magnet and the pyrolytic graphite should be defined. In our work, parametric analyzes in their different sizes were made and by comparing the dimension effects of them, the region where the magnetic forces are linear was selected to achieve more stable levitation characteristics. We choose 5 mm thickness of the pyrolytic graphite due to its thickness of 3-7 mm had a better linear force performance as shown in figure 2.3. Moreover, as seen in figure 2.3 again, while 10-fold increase of thickness in the range of 1-10 mm thickness, the diamagnetic force increases only about 4 times. Thus, the one can be seen that the thickness of the pyrolytic

graphite is not proportional to the diamagnetic force generated. The thickness effect could be eliminated by the selection of the lifter magnet size to increase/decrease the levitation force.

First, the analysis of the diamagnetic force which is effected by the pyrolytic graphite thickness is shown in Figure 2.3.

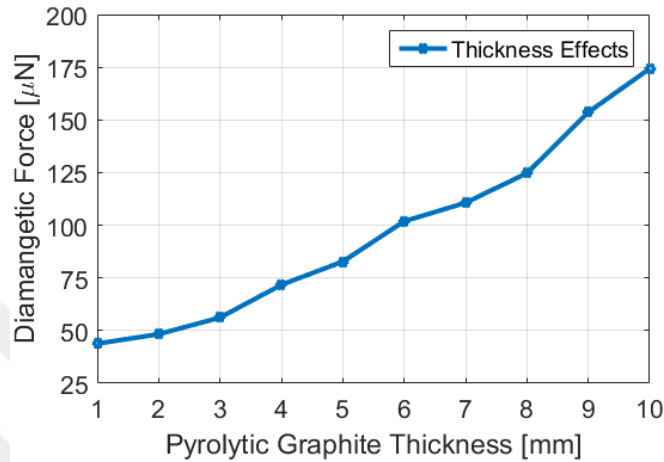


Figure 2.3 The effect of pyrolytic graphite thickness varying in 1-10 mm on diamagnetic force was calculated. Since the diamagnetic force behaves more linearly in the range of 3-7 mm, material thickness in this range can be selected to get better levitation performance.

As a result of the analysis, pyrolytic graphite with a thickness of 4.83 mm was used. The same analysis was carried out this time to determine the lifting magnet size effects. The variation of the magnetic force value, which will vary with the lifting magnet size, should be determined.

### 2.3 Microrobot Mathematical Modeling

The force value required to levitate the micro-robot in the Z-axis should be calculated first in the system given. The forces acting on the micro-robot during the levitation of the equilibrium in the z-axis are shown in Figure 2.5.

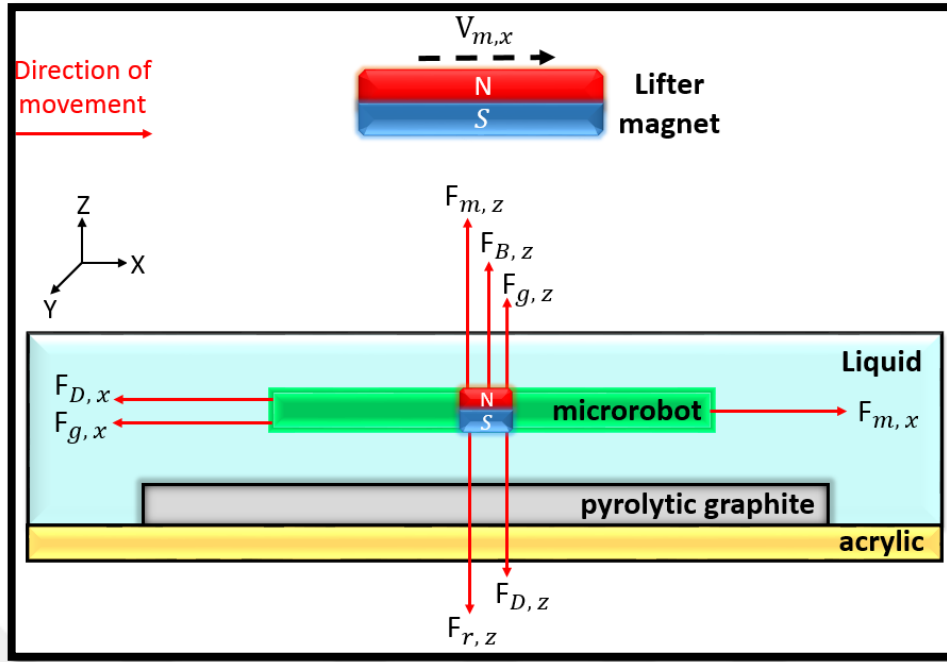


Figure 2.4 According to the position of the lifting magnet on the Z-axis, the mechanical contactless movement of the micro-robot on pyrolytic graphite is shown schematically.  $F_m$ : Lifting magnet force,  $F_{dia}$ : Diamagnet force,  $F_B$ : Buoyant force,  $F_r$ : Gravitational force and  $F_D$ : Drag Force is shown.

Gravitational, Buoyancy, and Drag Forces shown in Figure 2.4, can be expressed individually as,

$$F_r = m_r g \quad (2.9)$$

$$F_B = V_r (\rho_r - \rho_f) g \quad (2.10)$$

$$F_D = \frac{1}{2} c_d \rho_f A v |v| \quad (2.11)$$

Attractive magnetic force induced by lifter magnet,  $F_m$  can be expressed in integral form as [17],

$$F_m = \frac{\mu_r - 1}{2\mu_0 \mu_r} \iiint_V \nabla B^2 dv \quad (2.12)$$

$$F_m = \frac{\mu_r - 1}{2\mu_0 \mu_r} \iint_S B^2 ds \quad (2.13)$$

Alternatively, the differential form is derived by Thomson's formulation as,

$$F_m = \frac{V_p \chi}{2\mu_0 \mu_r} (B \nabla) B \quad (2.14)$$

Boundary conditions such as  $\nabla B^2 > 0$  and  $(\mu_r - 1) < 0$  should be satisfied to ensure stability at the equilibrium point. From this equation, a magnetic field gradient is needed so that a linear force can be generated on the microrobot. The position of the microrobot can be controlled by positioning the magnetic field gradient relative to the microrobot. Where  $n_x, n_y, n_z$  are the surface normal vector component of the diamagnetic material in  $x, y, z$  direction respectively (2.15-2.17). The force between the diamagnetic material and the carrier magnet can be obtained through equations (2.12-2.14). After determination of the permanent and diamagnetic forces which are given in the equation set (2.6-2.8, 2.14), the dynamic model can be expressed by (2.15-2.17) for each relevant axis,

$$\ddot{x} = \frac{1}{2m_r} c_d \rho_f A_x v_x |v_x| + \frac{(F_{m,x} + F_{g,x})}{m_r} \quad (2.15)$$

$$\ddot{y} = \frac{1}{2m_r} c_d \rho_f A_y v_y |v_y| + \frac{(F_{m,y} + F_{g,y})}{m_r} \quad (2.16)$$

$$\ddot{z} = \frac{1}{2m_r} c_d \rho_f A_z v_z |v_z| + \frac{v_r g}{m_r} (\rho_r - \rho_f) - g + \frac{(F_{m,z} + F_{g,z})}{m_r} \quad (2.17)$$

In addition, the net force (2.18) can be collected by a single expression to simplify the sum of the magnetic forces acting on the microrobot as,

$$F_{net} = F_m + F_g \quad (2.18)$$

So far the theoretical model and design of microrobot are completed.

#### 2.4 Microrobot Experimental Setup Selection

There are two other parameters that must be determined before starting the experimental work. The geometric complexity of the experimental set-up makes the solution of the system theoretically complex with the formulation. For this reason, numerical analysis is the foreground for a faster and more accurate solution. However,  $c_d$  and  $F_{net}$  should be calculated by FEM analysis. Drag force coefficient,  $c_d$ , varies depending on the stress exerted on the surface of microrobot. Thus, Number of equation (2.3) is reshaped and  $c_d$  left alone,

$$c_d = \frac{2F_D}{\rho_f A v^2} \quad (2.19)$$

The calculation of the  $c_d$  shown in equation (2.19) requires that the  $F_d$  should be determined first. The measurement of the surface tension of the microrobot was calculated by FEM analysis because of the complexity of the geometric structure and the

difficulty of solving the mathematical formula for each stress interval. Computational fluid dynamics must be applied to  $F_d$  computation of the microrobot moving in an enclosed fluid environment. The problem is resolved in the fluid structure interface module in COMSOL. For  $F_{net}$ 's force, equations (2.6-2.8, 2.14), should be considered together. The levitation equilibrium point of the lifter magnet position must be found. However, for each change interval, the solution of the related equations is quite long and the accuracy rate is lower than necessary ( $\mu\text{N}$ ). Parametric analysis is necessary in order to calculate more precise force, the analysis is done in the magnetic field module in COMSOL. As a result of the analysis,  $F_{net}$  calculation has been completed, depending on the position of the lifter magnet in z-axis. The values of parameters which can be calculated theoretically in equations (2.15-2.17) are shown in table 2.2.

Table 2.2 Calculated parameters in equ. (20-22)

Parameters	Value	Unit
$m_r$	$2.929751 \times 10^{-6}$	kg
$g$	9.81	$\text{m/s}^2$
$\rho_r$	1798.374	$\text{kg/m}^3$
$\rho_f$	998.2071	$\text{kg/m}^3$
$A_x$	$1.229066 \times 10^{-6}$	$\text{m}^2$
$A_y$	$1.229066 \times 10^{-6}$	$\text{m}^2$
$A_z$	$8.15402 \times 10^{-6}$	$\text{m}^2$
$V_r$	$1.61911 \times 10^{-9}$	$\text{m}^3$

By parametric analysis, the lifting magnet size and the range of positioning should be calculated. Observation of the effect of the lifting magnet in different locations is very important in the formation of the system. As can be seen from equation (2.3), the value of  $c_d$  must be calculated. The aim here is to obtain total constant force value which can be calculated according to Equation (2.9-2.11) in the scheme of Figure 3. Thus, the value of the force to be obtained from pyrolytic graphite and lifting magnet can be found. The equilibrium point will be obtained when the magnetic forces are equal to the net of the forces in Equation (2.9-2.11).

### 2.4.1 Mesh Selection

First, FSI analysis was performed to calculate the drag force given in Equation (2.19). In the relevant analysis, the  $c_d$  value was calculated as the result of varying surface stresses and micro-robot speeds. Figure 2.5 shows the experimental setup and mesh construction.

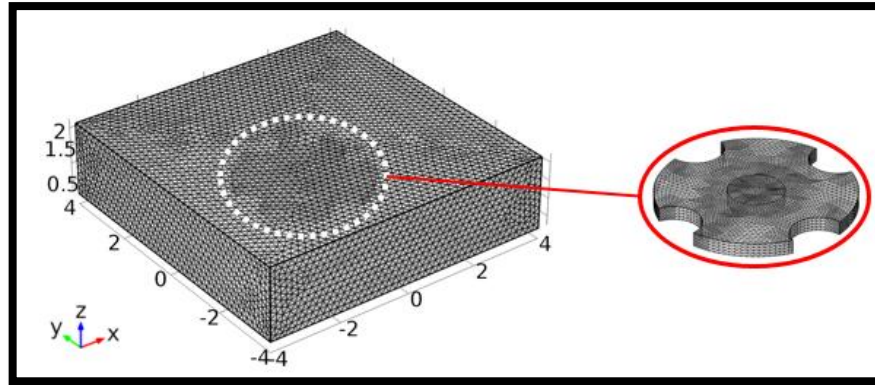


Figure 2.5 The mesh structure used in FSI analysis is shown. The microrobot is placed in the water-filled container with 4x4x2 mm outer surface. The effects of different surface stress force,  $F_D$ , acting on a microrobot surface are calculated. For a more accurate and precise result, the microrobot has been assigned a minimum width of 0.2 mm, and a thickness of 2 times the thickness of a max 0.4 mm mesh. A maximum of 0.5 mm was selected for the container. It is also applied to the system at regular refinement level 2. It can be seen that the mesh-size values should be very close and the direct solver method should be used to have more accurate results.

The best time effective and precise results of the mesh structure is shown in Figure 4 calculation of  $c_d$  parameter in COMSOL<sup>®</sup> FSI analysis. Moreover, corner refinement property of COMSOL<sup>®</sup> can be also used to get more accurate stress values on the corner edges of the microrobot.

### 2.4.2 CFD Analysis

Stress changes and velocity values at the surface of the relevant micro-robot are shown in Figure 2.6.

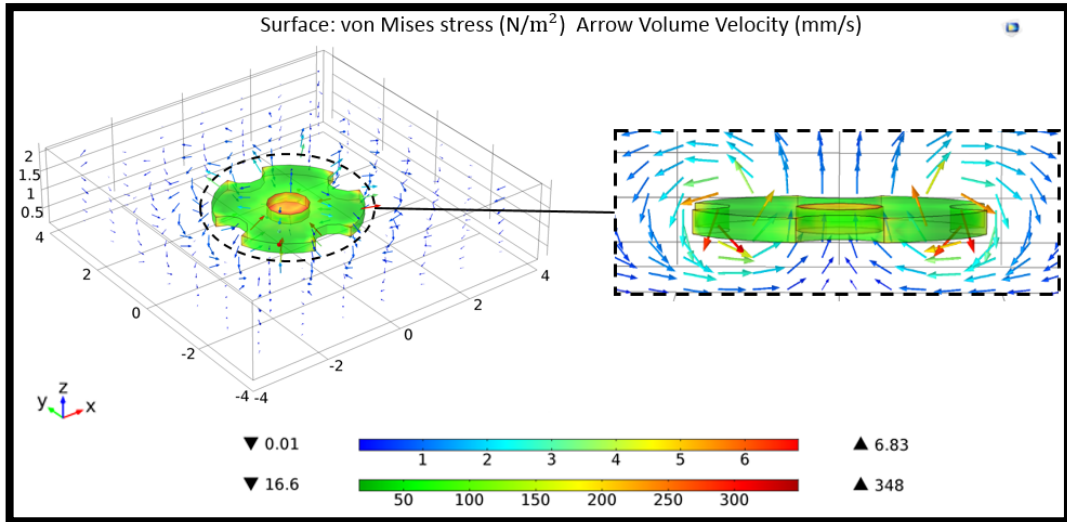


Figure 2.6 Stresses on the robot surface and speed lines around it are shown. When looking at the speed lines, values of 0-7 mm/s are represented by the upper bar. Light blue-green colors were observed more intensively and a speed of 3-4 mm/s was observed. When the effect on the robot is examined, it is seen that the lower bar is 16.6-348 Pa and the feature is more at corner and intersection points. The reason is that the surface area, where in the corner is smaller, increasing the pressure force. At the same time, the different formation of the intersection point of su8-magnet hardness affects the homogeneous distribution in stresses. So, intersection point of su8-magnet has more stress.

The stress values calculated for the analysis are determined for the  $c_d$  value in equation (2.3), and the time dependent  $c_d$  variation graph is shown in Figure 2.7.

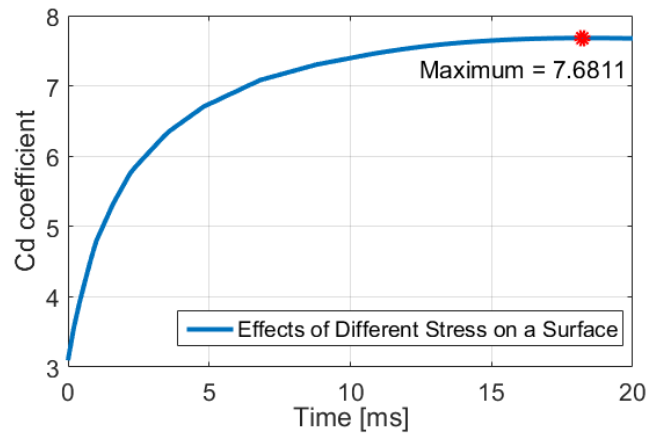


Figure 2.7 Micro-robot behavior was observed as a result of different stresses and velocities due to Time-Dependent analysis. As can be seen, a constant  $c_d$  coefficient characteristic is obtained after a certain period of time. This value is calculated as  $c_d = 7.6811$ ; (3),  $F_D$  will change depending on the speed.  $F_{D,max} = 0.125 \mu\text{N}$  when the robot speed is selected as  $\pm 2 \text{ mm / s}$ , depending on the micro stage speed to be used mostly in magnetic levitation setup. At the same time, it is seen that the value of the force that varies parabolically in this range is negligible because it is about 1/1000 of the diamagnetic force.

According to Figure 2.7,  $c_d$  is calculated and drag force on a surface shall be determined.  $F_{d,z}$  is shown in Figure 2.8.

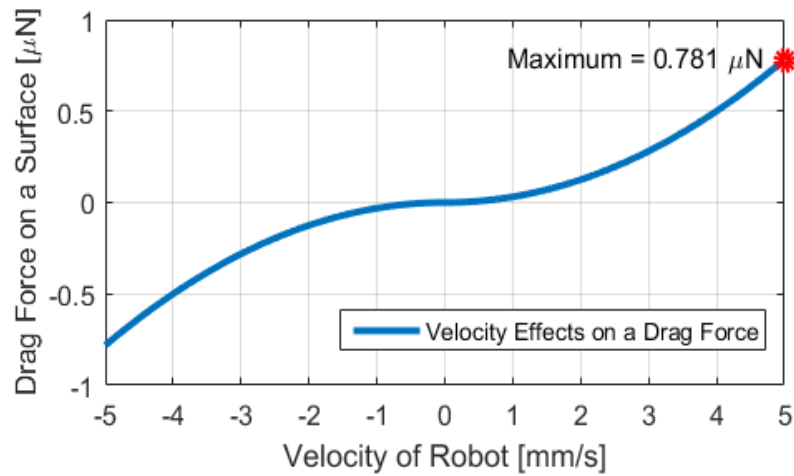


Figure 2.8 According to the simulation results, it is calculated that the force generated for the maximum stage speed of 5 mm/s is 0.781  $\mu\text{N}$

According to the analyzes made, it is necessary to finally calculate the required lifting magnet force value so that the micro robot can levitate.

### 2.4.3 Lifter Magnet Selection for Required Force

When  $F_{\text{net}} = 0$  was obtained by calculating the force values given in equations (2.18), the micro robot showed the range of levitation with the lifting magnet. In Table 2.3, the constant forces  $F_B$  and  $F_r$  are expressed.

Table 2.3 Constant Force Values

Forces	Value	Unit
$F_B$	12.788	$\mu\text{N}$
$F_r$	28.741	$\mu\text{N}$

Accordingly, it is estimated that the net force to be applied should be around 16.04  $\mu\text{N}$ . In the definition of each magnetic force which forms the force  $F_{\text{net}}$  shown in Eq. (2.18), the relation between the magnetic field and the magnetic flux can be expressed,

$$\mathbf{B} = \mu_0(\mathbf{H} + \mathbf{M}) \quad (2.20)$$

where  $\mu_0 = 4\pi 10^{-7}$ . The relationship between magnetization, magnetic field and magnetic flux for a linear isotropic medium can be obtained,



$$\mathbf{B} = \mu_0 \mu_r \mathbf{H} \quad (2.21)$$

From the equations (2.20-2.21), the magnetization vector is expressed in terms of flux density,

$$\mathbf{M} = \frac{\mu_r - 1}{\mu_0 \mu_r} \mathbf{B} \quad (2.22)$$

Thus, Attractive magnetic force induced by lifter magnet,  $F_m$  can be expressed in integral form as

$$F_m = \frac{\mu_r - 1}{2\mu_0 \mu_r} \iiint_V \nabla B^2 dv \quad (2.23)$$

$$F_m = \frac{\mu_r - 1}{2\mu_0 \mu_r} \iint_S B^2 ds \quad (2.24)$$

From this equation, a magnetic field gradient is needed so that a linear force can be generated on the robot. The position of the micro-robot can be controlled by positioning the gradient of the magnetic field within it relative to the micro-robot.

The size of the lifting magnet was determined according to the diamagnetic force generated by pyrolytic graphite, which has a specific thickness. As a variable, the type of magnet with the ratio of inner diameter to outer diameter was 1/2 and the analysis result was given in Figure 2.9.

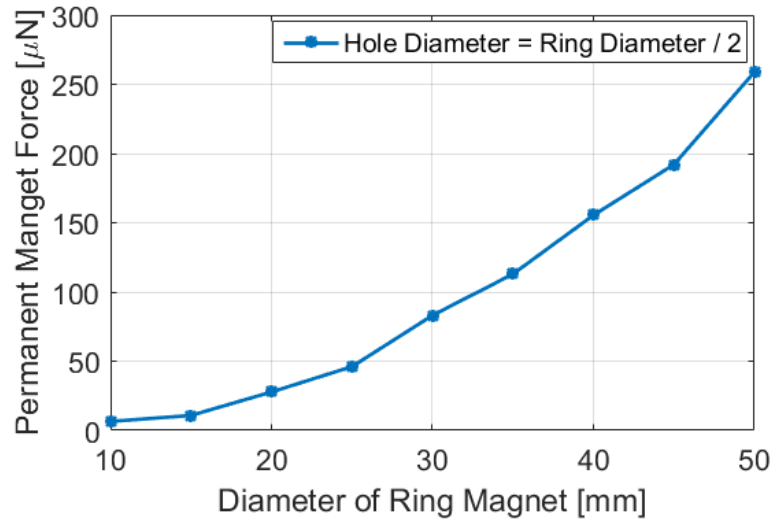


Figure 2.9 The effect of the change of the dimensions of the ring-type lifting magnet is shown. The lifting magnet, which is a more linear characteristic in the range of 25-45 mm according to graph, exhibits exponential behavior according to its size outside this range

The selection criterion in this range would be to select a value that is greater than or equal to 2 times the force generated by pyrolytic graphite at a selected 4.83 mm thickness. It is preferred to use magnets having an outer diameter of 40 mm, an inner diameter of 20 mm and a thickness of 8 mm, which are within the appropriate linear range of the relevant value and which are easier to find. As a result of the analysis according to the variable parameters, a graph of the force generated in the microrobot Z-axis due to the distance between the pyrolytic graphite and the lifting magnet is shown in Figure 2.10

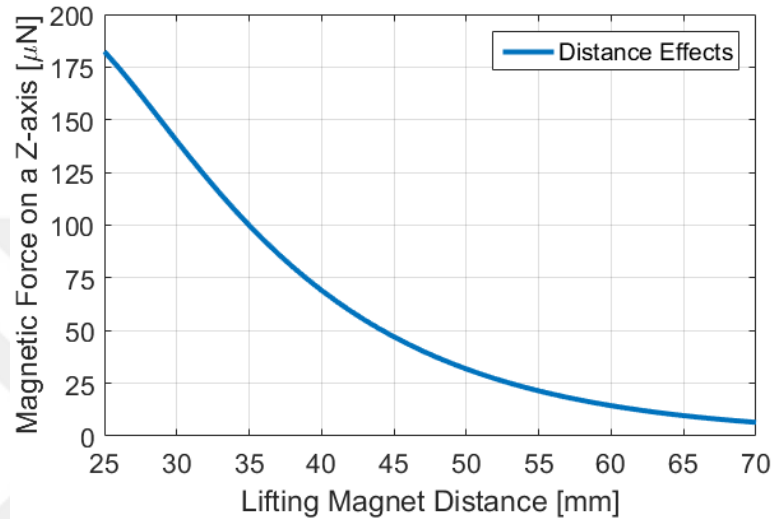


Figure 2.10 The magnetic force characteristic of the selected lifting magnet and pyrolytic graphite is a phenomenon that exponentially decreases as the microrobot moves away as expected. As a result of the selection criteria,  $F_{\text{net}}$  on micro robot was determined as 16.04  $\mu\text{N}$  according to Table 2. The result that the micro-robot could be levitate in the range of 50-60 mm according to lifting magnet-pyrolytic graphite distance in the X-axis has emerged.

#### 2.4.4 Experimental Setup with Equipments

Implementation of experimental setup; it contains a microrobot positioned in a DI water container with pyrolytic graphite on its surface. The ring magnet (lifter-magnet) on which the magnetic force required for levitation is obtained is on the vessel. To achieve stable and micro-precision levitation, it is necessary to position the lifter magnet on the DI water tank parallel and rigid. In order to perform levitation and precise position control at the micro level, a PI Micro Stage (M-126.PD2 / 20x20x20 mm) with 3-axis linear micro-movement sensitivity was placed on the Z axis. A manual micro-stage was used to position the DI water container parallel to the floor and to move the 3 axes when

necessary. Nano-sensitive laser distance sensor (optoNCDT-ILD2300-50) is preferred for instant measurement of levitation height within the system. At the same time, microscope camera-lens system (Olympus SZX-7 and PointGrey GS3-U3) positioned perpendicularly from the side profile to observe the mechanical contact of the microrobot with the pyrolytic graphite surface. The whole experimental setup where the levitation and motion characterization experiments of the microrobot are performed is shown in Figure 2.11.

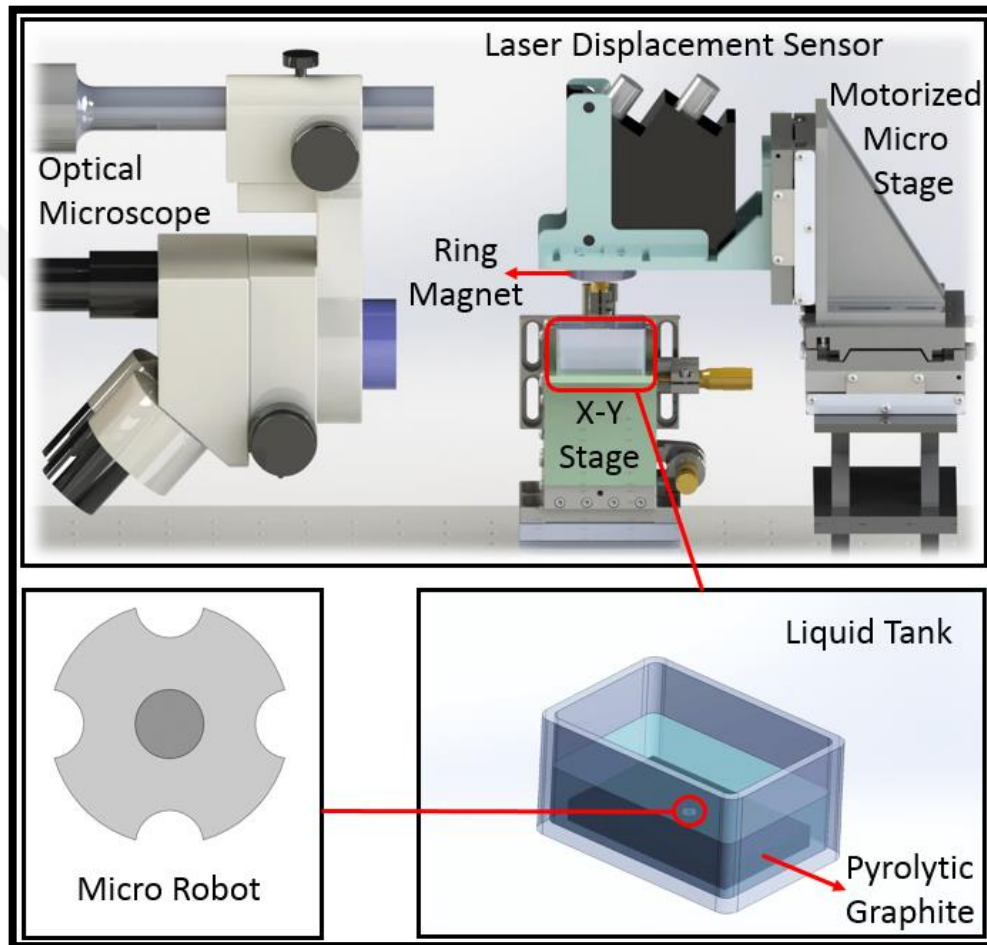


Figure 2.11 The control of the Micro Stage, which performs the motion as a ring magnet 3 axis linear, was realized through an interface created with C#. Camera image is transferred on the same interface. The reading of the data of the laser distance sensor is taken through the laser's own interface.

## 2.5 Micro Stage Control Interface

The microstage used for position control of the lifting magnet is shown according to the experimental setup shown in Figure 11. The micro stage is used as a controller which is capable of precise (nano) positioning in X-Y-Z axes and driven by Dc motors. There are 3 DC motors in the PI stage and these motors operate in the 0-24V voltage range and can

reach 50 mm / s [M126.PD2]. The speed value change of the servo motors according to applied voltage is shown in Figure 2.12.

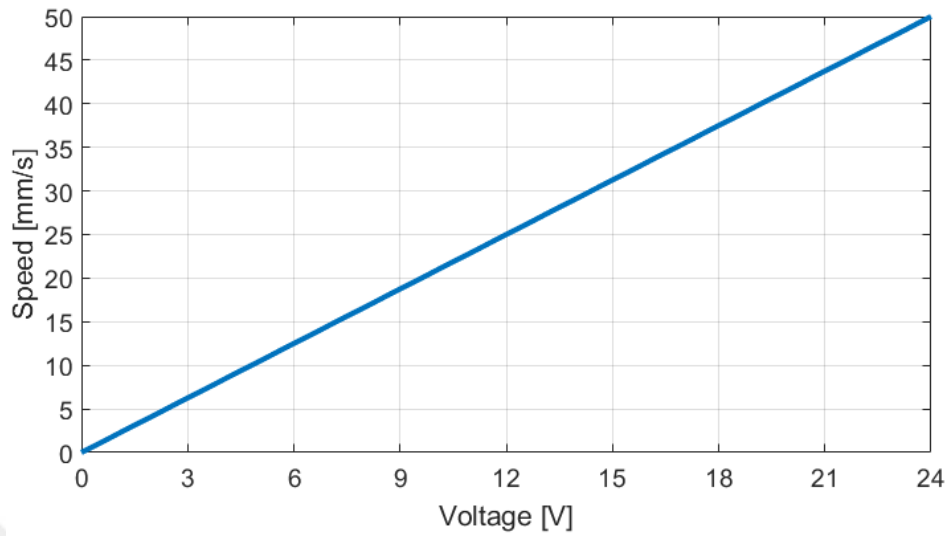


Figure 2.12 Relationship between voltage-speed of motor.

Accordingly, the inverse kinematic operation is performed on the interface prepared in C#, together with the mathematically modeled driver. The first interface for micro-robot control, which is primarily interface-connected, is shown in Figure 2.13.

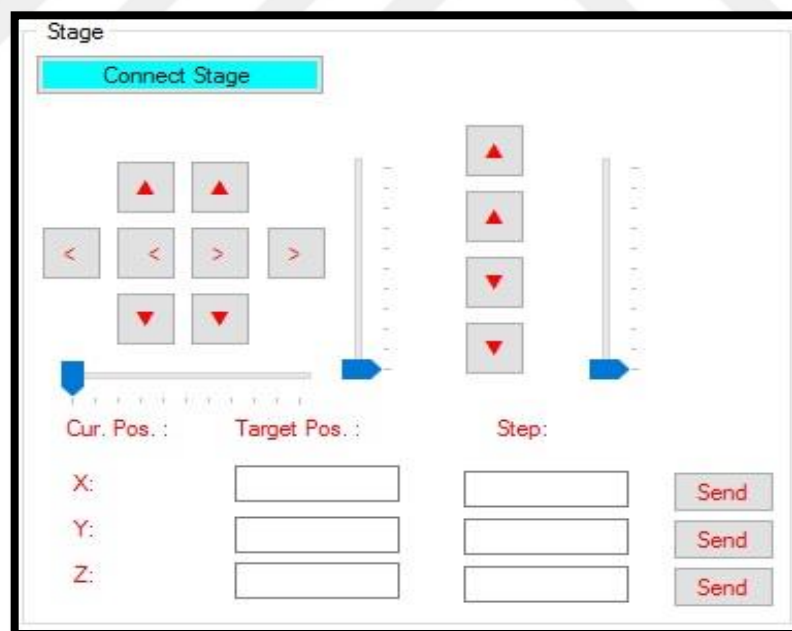


Figure 2.13 Connection of Stage Interface-1

By means of the manually added buttons, microrobot movement at the desired value is made possible. It can also be used in functions that are created in the relevant menu

structure and used in the trajectory tracking tests. The sinusoidal, circular, velocity change effect is shown in Figure 2.14.

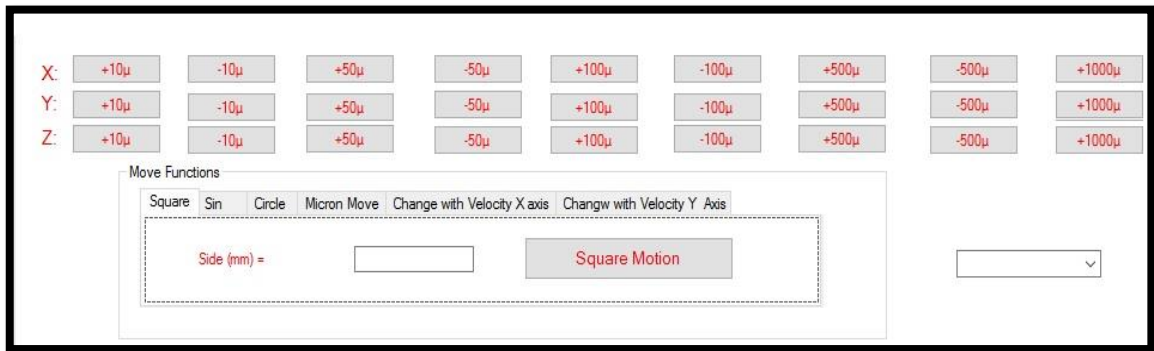


Figure 2.14 Manuel Control Interface of Microrobot via Computer

The interface for the entire system interface and the real-time processing of the view from the camera is shown in Figure 2.15.

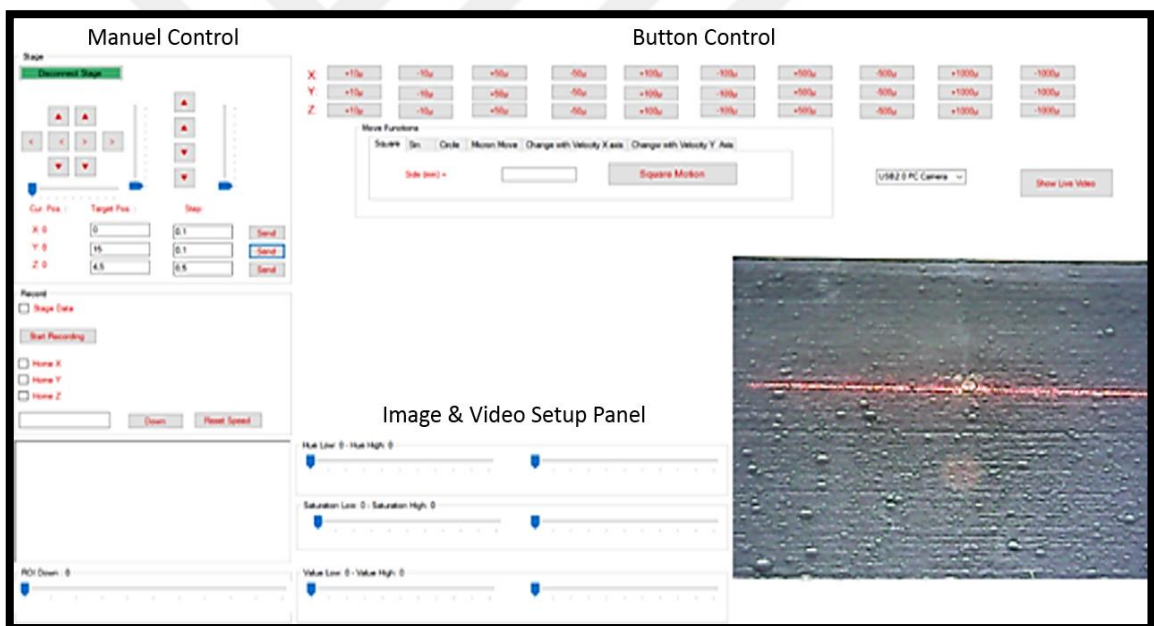


Figure 2.15 Whole system interface including with camre panel, image processing menu, manuel and button control properties

Speed control of the motors is done by pulse width modulation technique. In this technique, the voltage applied to the motor terminals is a square wave of constant frequency. The applied voltage time, in other words, the charge rate increases, the effective voltage increases and the motor speed increases in proportion to this. Effective voltage can be expressed,

$$V_{\text{rms}} = \sqrt{\frac{1}{T} \int_0^T v(t)^2 dt} \quad (2.25)$$

There are 10 $\mu$ , 50 $\mu$ , 100 $\mu$ , 500 $\mu$  and 1000 $\mu$  motion buttons shown in Figure 2.15 which we apply for each axis tool, with precise control of the micro-robot's levitation and x-y plane motion. Thus, the position and movement of the micro-robot on the x-y axis with the levitation height can be controlled at micron level. In order to observe the manipulation capabilities of the micro robot with levitation, images are taken from 2 separate cameras. The image is taken via MJPEG format via Web browser with static IP that we assigned to it from IP camera [DS-2CD2820F, HAIKON]. The IP camera is positioned parallel to the water tank as in figure 2. In this view, the micro-robot's levitation characteristic was observed on the IP camera, depending on the distance of the micro-robotics of the Lifter Magnet, using the micron level motion buttons on the system interface. The other camera provides usb to computer connection. The image of the usb camera is like the one in figure 3 in our own interface. The usb camera is positioned transversely from the top of the cabinet, and the movement capability of the micro-robot on the x-y axis is observed through the movement buttons on the system interface.

## **2.6 Micro Robot Production**

### **2.6.1 First Prototype Production**

#### **2.6.1.1 Nickel Based Micro Robot Solution**

The first prototype, nickel-based micro-robot production, has been described in turn. After the completion of the first design, the studies were directed towards production and integration. In the initial prototype design phase, our goal was to produce a nickel-based micro-robot arm to manipulate cells and objects up to a size of 100  $\mu\text{m}$ . In the context of the designs made in this context, oocytes (oocytes) and oocytes were used as design parameters since the diameter of objects manipulated by the similar micro-robot arm was determined to be about 100  $\mu\text{m}$ . At the same time, the thickness of the nickel-based micro-robot arm to be used during the manipulation process was determined to be 250  $\mu\text{m}$ . For this reason, it is desired to maximize the lifting force by increasing the sinking volume. The end-effector width of the micro-robot arm to manipulate the particles is 250  $\mu\text{m}$  and the length is 1 mm. There are two arms for the center of gravity to remain intact and for multipurpose use. The purpose of the robot arm is to realize different purposes in the future, and the other arm is designed as a pointed end which is designed as a pointed end for clamping and cutting. According to the dimensions of the designed micro-robot arm;

The height of the microfluidic channel in the micro-robot arm was accepted at experiments at this stage as 500  $\mu\text{m}$ . This will provide sufficient space for the 250  $\mu\text{m}$  thick micro-robot arm to not touch the upper and lower walls of the microfluidic channel. A micro-robot arm system has been designed to be used in the petri dish when necessary. The micro-robot arm in the liquid has 4 magnets used to control the 3 axes. The reason for using 4 magnets is to move the micro-robot arm by providing maximum stability and precise orientation, which can be best achieved with the proposed structure. Fixed magnets of 1 mm<sup>3</sup> size, which can be found easily in the market, will be used. As it is seen in the previous report period that magnetic analyzes and simulations were made, The required magnetic force to move the micro-robot arm can be achieved with 1 mm<sup>3</sup> permanent magnets. Due to this reason, in design, the micro-robot arm has 4 1x1 mm region nickel covered with discrete legs (square regions). As a result of the design, a 4 mm wide and 6 mm long nickel based micro robot is shown in Figure 2.16.

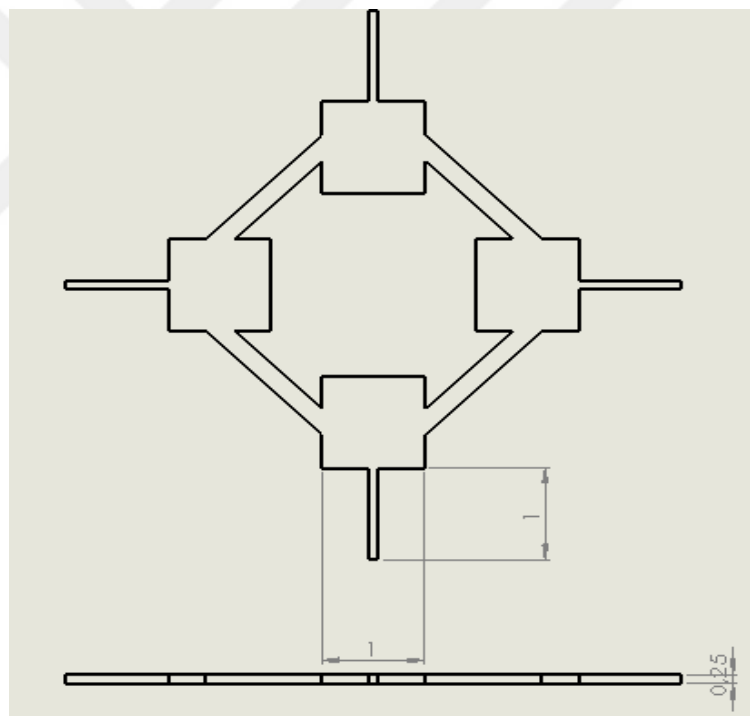


Figure 2.16 Microrobot first prototype design

Solidworks for the production of nickel-based robotic arm has been designed by Advent Research Materials Ltd. Five pieces of Nickel plate 150 mm x 150 mm in thickness 250  $\mu\text{m}$  thick, tempered at 99% purity, were supplied from the company.

In laser cutting devices, the laser beam can be cut by focusing on a very narrow area. In this way, the intensity of power required to break the material can be reached. The material to be cut can be melted in a very short time. When the laser is cut, heat is dissipated on the material by an additional gas applied from the cut edges and at the same time the slag formed in the material is removed by cutting. Figure 17 shows the roughness that occurs on the slag layer and surface formed on the surface of a piece cut by a laser. The laser beam cuts the relevant positions using a CNC-assisted workbench. Parameters determining the cutting quality in the laser cutting device; Laser power, auxiliary gas type and pressure, material thickness and type, cutting speed and type (pulsed or continuous).

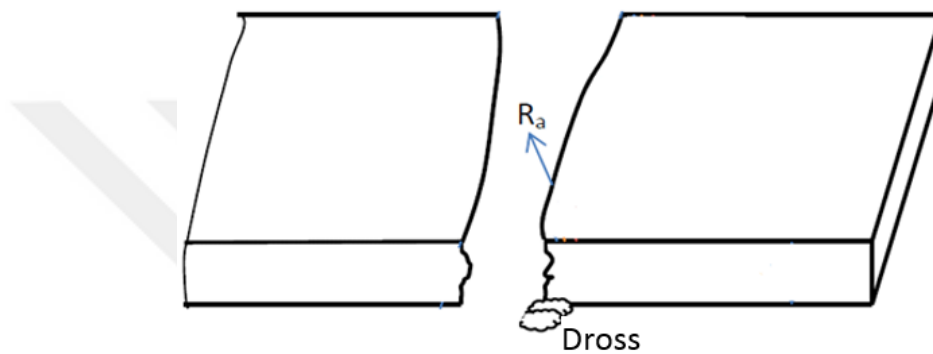


Figure 2.17 Slag Layer and Roughness Produced on the Surface of a Cutting Particle by Carbon Laser

The laser cut was carried out by expert personnel in the Clean Room of Boğaziçi University Kandilli Observatory, Life Science and Technology Application and Research Center. In order to realize the cuts, technical drawings were prepared in the desired file format and work was carried out by accompanied by expert staff in the stage of cutting. The resulting micro robot arm is shown in Figure 2.18, Figure 2.19.





Figure 2.18 First Nickel-Based Micro-Robot Arm Produced by Laser Cutting

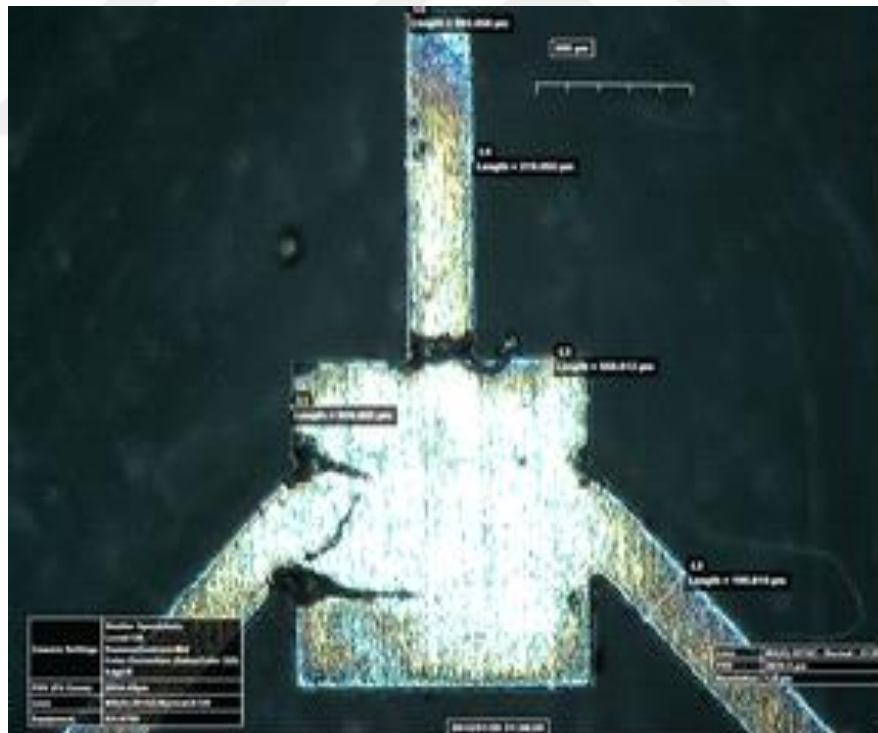


Figure 2.19 First Nickel-Based Micro-Robot Arm Deformations

As can be seen from Figure 2.18-2.19, optimal cutting parameters must be found due to obtain undamaged microrobot and it can be expressed in Figure 2.20.

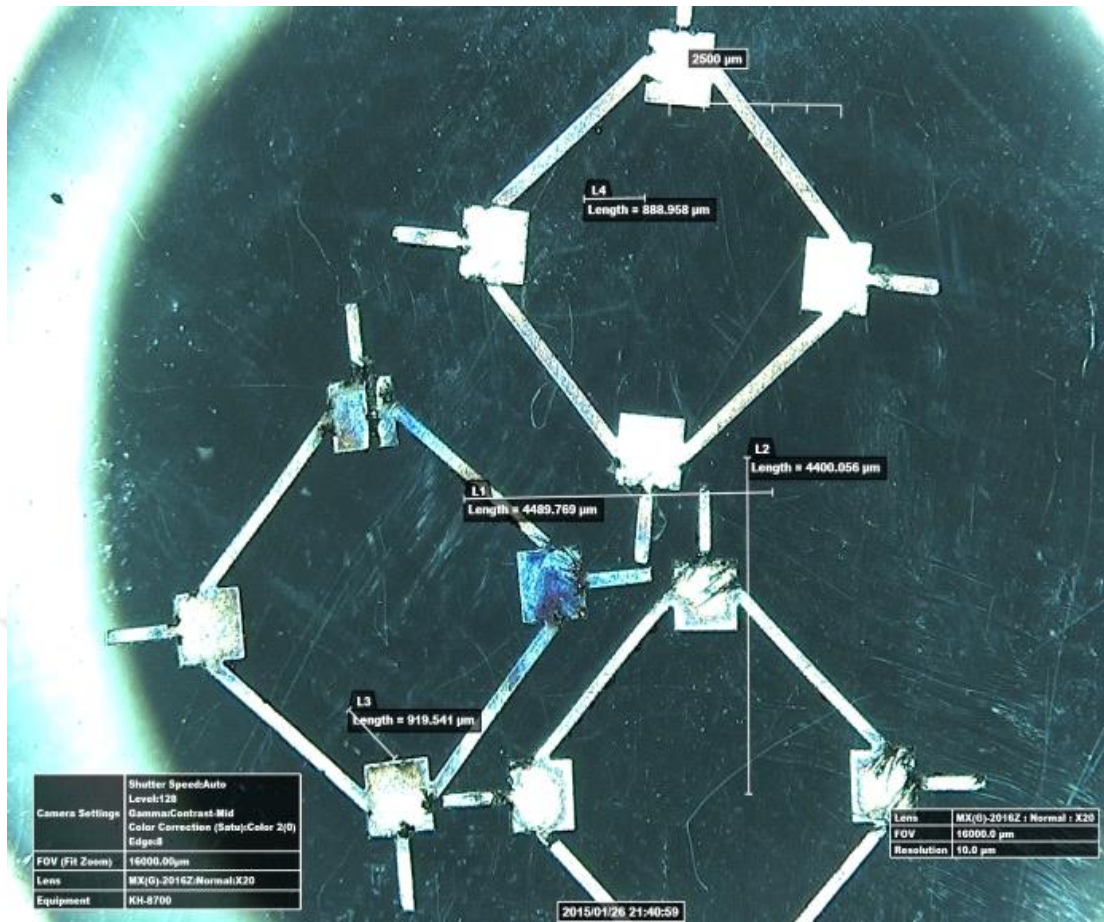


Figure 2.20 Optimal Cutting Parameters Nickel-Based Micro-Robot Arm Produced by Laser Cutting

At the end of the first experiment, as shown in Figure 18, Figure 19, the burrs and cavities were formed due to the thermal effect in sharp passages in the nickel-based micro robot arm produced by laser cutting. Then, parameters were changed and optimum cutting parameters were tried to be caught. As shown in Figure 20, after the optimum cutting parameters are found, the burrs and cavities are considerably reduced. Nickel in the laser cutting process P.A.L.S. Brand 400 W power, 1080 nm wavelength with 4 axis cutting fiber laser is used. In order to reduce the problems that occur during the cutting process due to thermal stresses during the cutting of nickel, the nickel plate is fixed by its edges with an established mechanism. The optimum cut surface during cutting was reached with the parameters given in Table 2.4;

Table 2.4 Optimum cut parameters

Peak Power	: 100 W
Frequency	: 1000 Hz
Puls Width	: 0.60 ms
Speed	: 3 in/s
Proses Gas	: Oxygen
Pressure	: 3 bar

It was decided to remove the small amount of burrs remaining on the micro-robot from the surface by sandblasting. This process was carried out with the use of glazing devices in dental laboratories as shown in Figure 20. Sandblasting is widely used in the surface treatment of industrial pollution and corrosion. Even so, even the micron-sized corrosion on the surface is removed by sandblasting and the desired metal surface is reached. During the sanding process, abrasive materials are sprayed onto the material at high pressure. Materials such as steel balls, alumina balls, silica and quartz can be used as abrasive materials. After machining, the optimum nickel-based micro-robot arm shown in Figure 2.21 is used.



Figure 2.21 Glazing process to reduce burrs and cavities of Nickel-based Microrobot produced by laser cutting



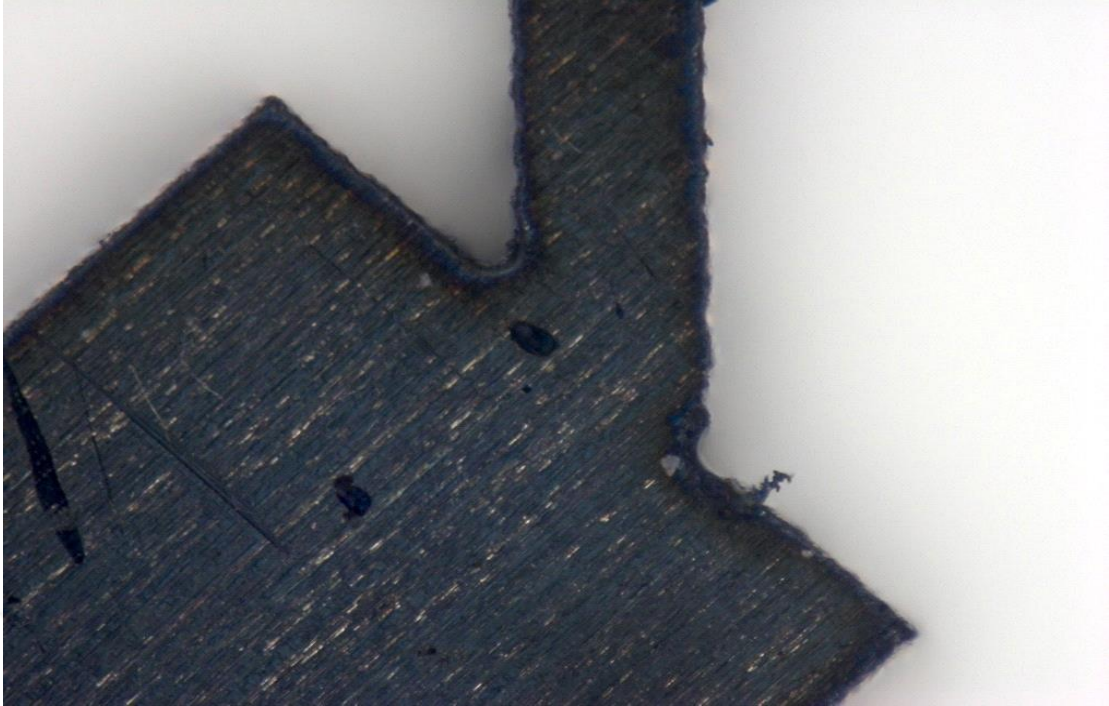


Figure 2.22 An image belonging to the micro robotic after grinding

#### **2.6.1.2 POLYMER MATERIAL SELECTION AND PROCESSING**

The first step in the production of the nickel-plated polymer micro-robot arm is to select the polymer material to be nickel coated. The first property demanded in polymer materials is that the density is lower than the water density and the water absorption is lower. However, another important parameter to be used in the micromanipulation process is the high hardness and young modulus. Considering all these properties expected from the polymer, it has been decided to work with polypropylene material.

Polypropylene has the ability to work in a wide range of temperatures, meeting the expectations in terms of density, hardness, strength and water absorption. The ability to run in a wide temperature range allows us to work in environments that require different operating conditions. However, as can be seen from the table, diluted / concentrated acids, alcohols and alkalis can also be used to protect the chemical structure without deterioration. Subsequent to the selection of the polymer material, the polymer material was processed using carbon laser according to the design. The carbon laser used in cuttings is a device in the Helix model 50 watt power of Epilog brand. In carbon laser cutting devices, the laser beam can be cut by focusing on a very narrow area. During cutting with the carbon laser, the material can not be processed with the desired precision due to the material type, thickness and sharp transitions. As a result of processing the

nickel material described in the previous section with the laser, the quality of the micro-robot arm obtained can not be obtained by processing the polymer material with the laser. Therefore, the search for different production techniques has been entered.

Cutting process of polymer material was carried out by micro-precision mechanical machining in " Micro-CNC " company. In manufacturing technology, demand for production by mechanical processing method increases day by day. The increase in production of micro (0.1-100 $\mu$ m) and meso (100 $\mu$ m-10mm) dimensions by mechanical machining in the market is also effective in this. CNC machine named "Röders rfm 600 mark" was used during cuttings. Micro-mechanical machining can be used to manufacture parts from 10  $\mu$ m to several millimeters. Although micro-mechanical machining is similar to conventional machining operations in conventional mechanical machining methods, micro-machining shapes the material surfaces using miniaturized cutting tools. During cutting, the micro fingertip is capable of three-dimensional machining with high depth ratio. The micro tools shown in Figure 2. 23, which are 1 mm or smaller, are included in the micro-tool classification.



Figure 2.23 Micromechanical machining precision and micro-finger milling pocket with a diameter of 6mm - 200 microns

During cutting, the speed of tooth advancement is much higher than the conventional method. The parameters to be selected directly affect the cutting quality. As shown in

Figure 2. 23, since the microprocessor can not be produced with the desired precision due to the thermal effects in the laser machining method of the polymer, micro-machining by means of CNC machining has been started. During the cutting process, the aluminum plate was rotated at a speed of 7000 rpm at a tip thickness of 6 mm, and the surface of the polymer plate was thinned to a thickness of 250 microns in layers of 100 microns with a feed rate of 2000 mm / min. In Figure 2.24, there are detailed views of the polymer material fixed with a metal layer adhesive after machining and turning into a micro-robot arm in order to balance during CNC machining.

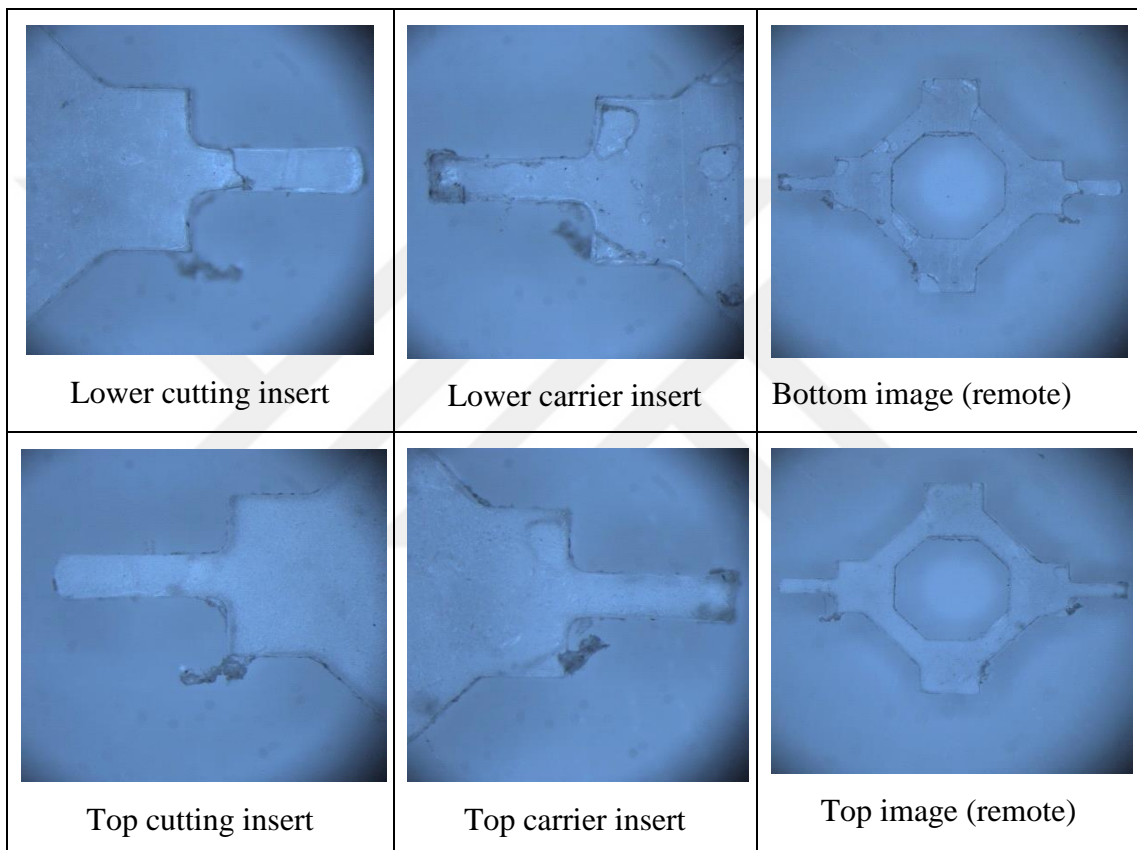


Figure 2.24 Detailed images taken after turning the micro-robot arm by processing the polymer material fixed with metal layer adhesive in order to balance during CNC machining

In Figure 2.25, there is detailed view of the microrobot that has been taken from the fixed surface after being removed with acetone.

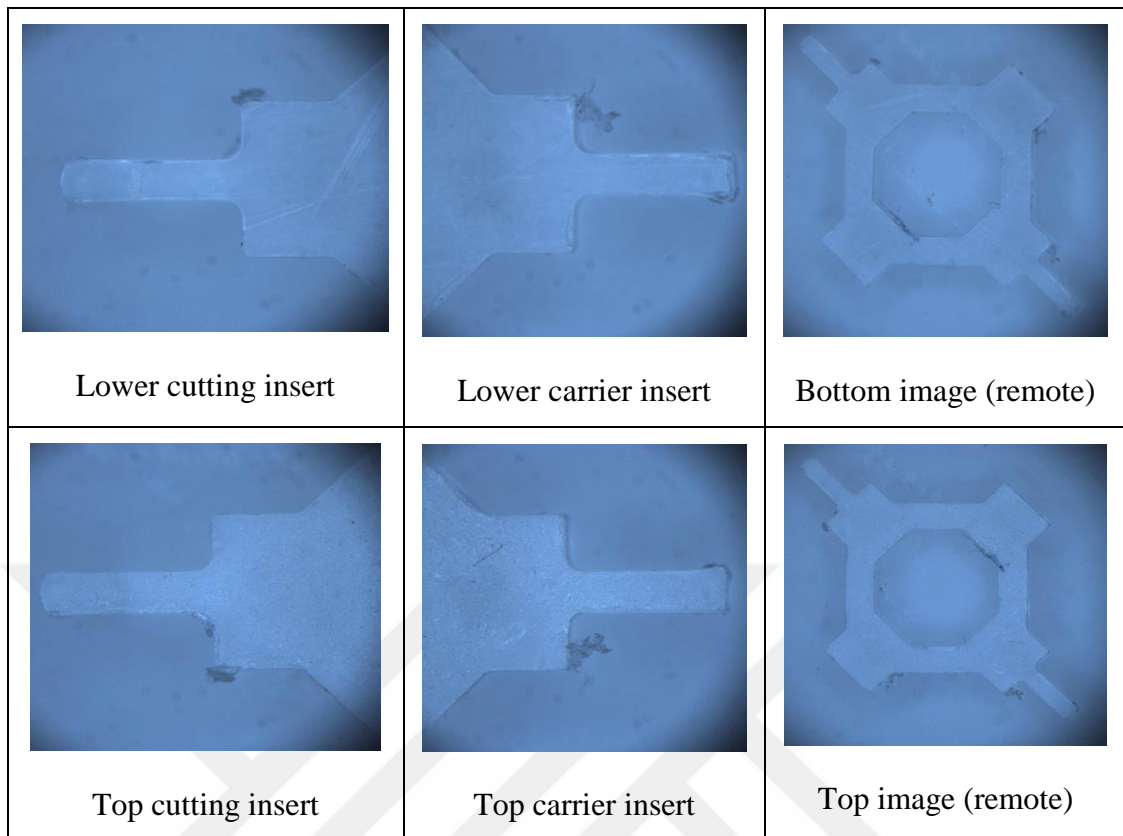


Figure 2.25 Detailed images taken after withdrawing with acetone from the fixed micro-robot wrist

Figure 2.26 shows a detailed view of the final state of the robot arm obtained by CNC machining with micro-precision.

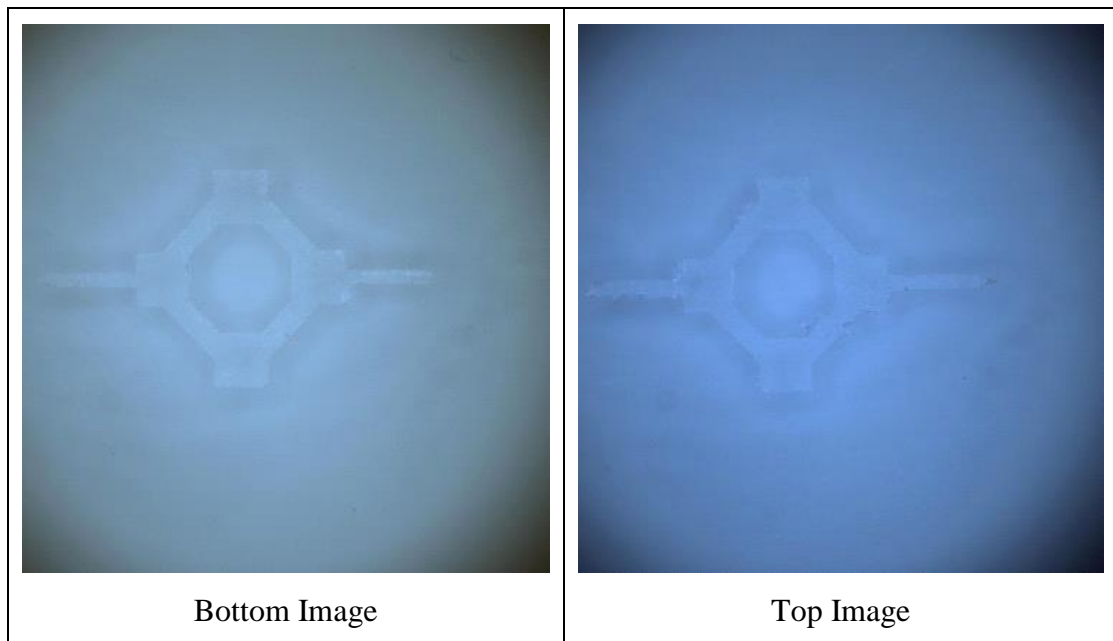
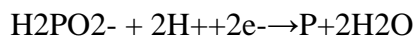
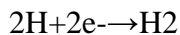
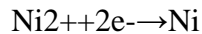
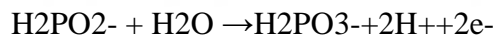


Figure 2.26 Detailed views of the final state of the micro robot arm obtained by machining with CNC in micro precision

## 2.6.2 PROCESSING OF SURFACE COATING WITH FLOW NICKEL PLATING METHOD

The autocatalytic coating process involves the reduction of metal ions to metal in a medium containing a chemical reducing agent. There is no electrode connected to the system. Instead of the anode, metal is supplied from metal salt. The surface of the material to be coated acts as a cathode. Reduction agent acts on the reduction of electrons. The coating process occurs on the catalytic surfaces in the solution. No power source is used during the coating process, but usually the coating solution is heated. Nickel and copper are usually coated during the electroless plating process but there are also applications for covering metals such as cobalt, silver and palladium.

A homogeneous coating layer can be obtained even in the coating of complex parts and the filling of small pores in the structure. The resulting coating has low porosity and mechanical and magnetic properties. In general sodium hypophosphite is used as reducing agent. Phosphorus is also present in the coating composition when hydrophobicity is used during coating. Other metals, such as boron, may also be incorporated into the structure when other types of reducing agents are used. The reactions that will take place during the currentless nickel plating process will be as follows [21].



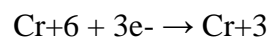
Other stabilizers, accelerators, regulators, surface activation components may also be present, such as an ion source providing a metal in a currentless nickel plating chamber and a reducing agent. By regulating the pH of the solution, the harmful effects of the hydrogen ions generated during the solution reduction process are avoided. Accelerators increase the surface coating speed. The regulators provide control of the autocatalytic reaction.

A few pre-treatments are required to coat the polymer with current-free nickel plating process. These processes are generally in the form of chemical etching, sensitization, activation [22].



### 2.6.2.1 Etching

Since the polymer surface is generally hydrophobic, chemical etching is performed to make the surface hydrophilic. The etchant solution can vary depending on the structure of the polymer to be coated. Before the etching process, the surface should be cleaned with distilled water, then the appropriate time and temperature are selected and kept in the etchant. The etchants are generally composed of strong acids, and the erosive effect on the surface of the polymer along the length of the pouch, along with the cavities. More metal ions can be retained on the etched surface, which in turn results in a stronger bond with the polymer surface. Reduction on the surface when using chrome based markers

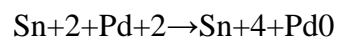


### 2.6.2.2 Sensitization

After the chemical etching process, the  $\text{Sn}^{+2}$  ion is absorbed into the polymer surface. The  $\text{Sn}^{+2}$  ions in the surface will then displace with  $\text{Pd}^{+2}$  ions. After the chemical etching solution, the polymer piece is immersed in the  $\text{SnCl}_2 / \text{HCl}$  solution. The purpose of using HCl is to increase the solubility of  $\text{SnCl}_2$ . The next step after the sensitization process is the activation process.

### 2.6.2.3 Activation

The activation process is intended to form catalytic sites on the polymer material. When the polymer is immersed in the  $\text{PdCl}_2$  solution,  $\text{Pd}^{+2}$  ions and  $\text{Sn}^{+2}$  ions on the surface of the polymer are displaced and the Pd film covers the entire surface.



Reduction of the surface of Pd during the activation process

### 2.6.2.4 Non-current nickel plating phase

The activated polymer part is cleaned and discharged into a non-current nickel bath. Processes such as temperature, pH, mixing directly affect the properties of the coating.

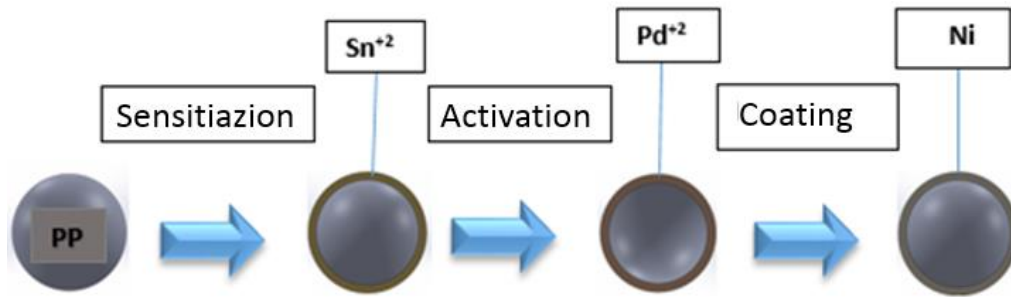


Figure 2.27 Nickel Plating on Polymer Material

Within the scope of the project, non-current nickel plating method has been utilized in coating of micro robot parts produced in CNC by micro processing method. The surface was first cleaned in order to remove the contamination that occurred during the cutting process. For this purpose a low concentration of 37% HCl was used. 50 ml was completed by adding distilled water on a volume of 1000 ml (1 ml) of 37% HCl using a micropipette. The micro robot is left for 4 minutes at room temperature for 10 minutes, then the micro robot removed from the solution is rinsed with distilled water and is shown in Figure 2.28.

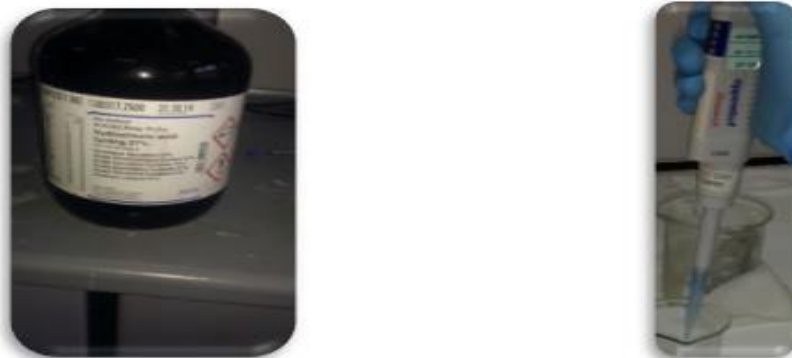


Figure 2.28 Preparation of Diluted HCl Solvent for Polymeric Material Cleaning

After the cleaning process, the micro-robot was immersed in the prepared acid solution to etch the surfaces to make the surface hydrophilic and to hold the metal on the surface. This EtCH solution was prepared with H<sub>2</sub>SO<sub>4</sub>: 100 ml / L K<sub>2</sub>Cr<sub>2</sub>O<sub>7</sub>: 20 g / L and H<sub>2</sub>O: 20 g / L. In the Etch solution, the micro-robot arm was allowed to stand for about 10 minutes and then rinsed with distilled water.



Figure 2.29 Preparation of Diluted HCl Solvent for Polymeric Material Cleaning

After the Etch process, the surface is subjected to surface sensitization to ensure the absorption of  $\text{Sn}^{+2}$  ions to the surface. For this purpose 0.05 g of  $\text{SnCl}_2$  was weighed on a precision scale and then a solution was prepared with 50 ml of distilled water. To increase the solubility of  $\text{SnCl}_2$  in water, 1.80 g of a 37% HCl solution was added. To further accelerate the dissolution process, the solution was stirred at 300 rpm for about 30 minutes in the magnetic stirrer.

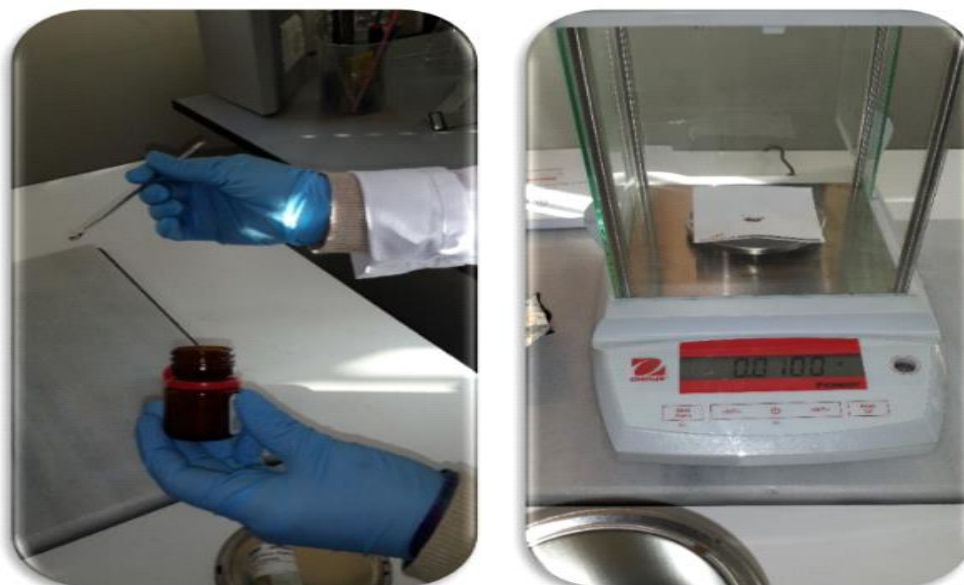


Figure 2.30 Weighing of Sensitive Level Chemicals

For activation, 0.045 g of PdCl<sub>2</sub> was weighed on a precision scale. 3.60 g of 37% HCl again to ensure solubility such as SnCl<sub>2</sub> solution prepared with 100 ml of distilled water. To provide homogeneity of the mixture, the solution was mixed at a speed of 300 rpm in a magnetic stirrer for about 30 minutes.



Figure 2.31 PdCl<sub>2</sub> and SnCl<sub>2</sub> solutions in a magnetic stirrer

The micro-robot was first placed in the SnCl<sub>2</sub> solution for 30 minutes, then transferred to the PdCl<sub>2</sub> solution and the solution was allowed to stand for 30 minutes. The micro robot is then rinsed with distilled water and ready for coating in a current-free nickel plating solution.

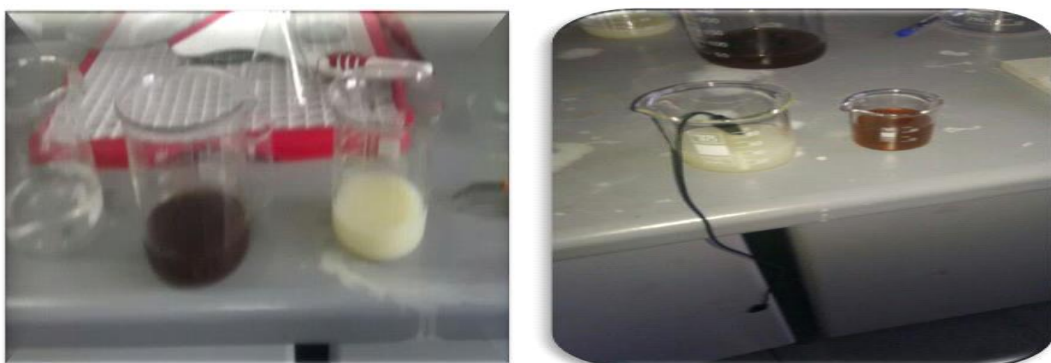


Figure 2.32 Image of PdCl<sub>2</sub> and SnCl<sub>2</sub> solubles after magnetic stirring and acid addition

The components of the current-free nickel-plated blanket to be coated are supplied from Huğlu Kaplama. Nickel sulphate salt, sodium hypophosphite, proprietary EN10 chemistry is used in the process of non-current nickel plating.



Figure 2.33 Pictures of sodium hypophosphite and nickel sulfate salt

The ratios of the components used in the bath during bath preparation are shown in Table 2.5.

Table 2.5 Ratios of Components Used in Solution During Bath Preparation

<b>BATHROOM INSTALLATION</b>	
Nickel Sulphate	27 gr/lt
Sodium Hypophosphite	22 gr/lt
En10 Chemical	45 ml/lt
Regulatory solution	1 ml

A 1 liter bath was prepared for nickel-free plating. First, the 1 liter beaker is filled with  $\frac{3}{4}$  of pure water and then the required 10 chemicals are melted. Nickel phosphate salt and sodium hypophosphite are dissolved in hot water (60-70 °C) in separate containers and 1 liter beaker is added into pure water. The tank is filled with pure water to the working level. After thorough mixing the pH is controlled. It is preferred that the pH is between 7-8. High pH ratios can cause H<sub>2</sub> bubbles to form on the surface, which affects the quality of the coating adversely. As can be seen from the equations given for the solution, the high pH will reduce the proportion of phosphate in the nickel phosphate. However, the reduction of the phosphorus ratio will increase the magnetism of the coating. The prepared currentless nickel plating bath has a low percentage of phosphate but it has been deemed necessary to make pH adjustments in order to improve the required magnetic properties. The pH of the prepared current-free nickel-plating bath was measured as 4 with a pH meter.



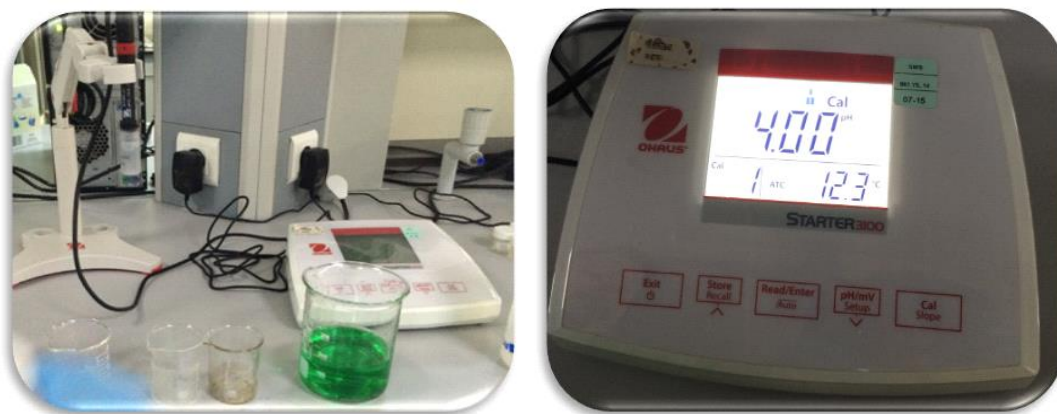


Figure 2.34 Measurement of the pH of the current-free nickel-plating bath prepared by pHmeter

In order to increase the pH while adjusting the pH, 10% ammonia solution is added to the bath to provide instant control by phmeter. In order to lower the pH which is high, 10% sulfuric acid is added. The bath should be mixed with magnetic stirrer and the bath heated while these appliances are made. Since we wanted to bring the pH between 7-8, we added 10% NaOH to the appropriate amount, bringing the pH to 7.98. In order to increase the pH while adjusting the pH, 10% ammonia solution is added to the bath to provide instant control by phmeter. In order to lower the pH which is high, 10% sulfuric acid is added. The bath should be mixed with magnetic stirrer and the bath heated while these appliances are made. For this reason, the pH was increased to pH 7.98 by adding 10% NaOH to the appropriate amount to bring the pH between 7-8.



Figure 2.35 Coating of the polymer micro-robot arm in a current-free nickel plating chamber at 80 ° C

Once the current-free nickel-plated board has been prepared in the desired composition, it is placed on the hotplate as shown above. During the coating process, the temperature was fixed to the thermocouple at 80 ° C and the solution was mixed at a rate of 300 rpm during the coating process. The resulting images of the nickel-plated polymer micro-robot arm obtained after the 5-minute residence coating process are as shown in Figure 2.36.

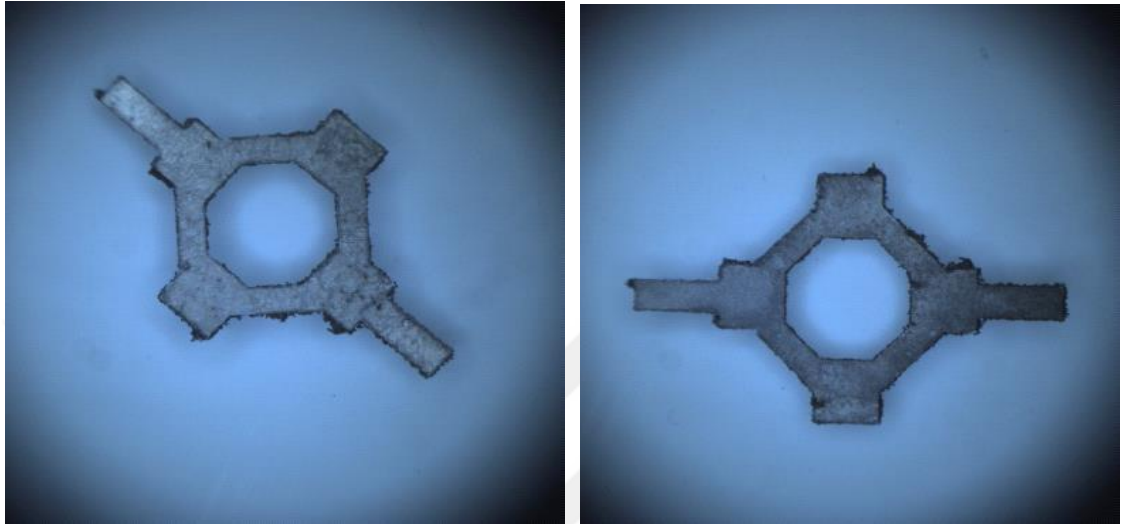


Figure 2.36 Images obtained from the front and back surfaces of the polymer micro-robot arm after the currentless nickel plating process.

As can be seen from the Figure 2.36, the surface state of the polymer micro-robot arm after nickel plating is visible. Since the scraping process on the whole surface can not be realized as desired, there are point voids on the surface. This is due to the inadequate activity of HCl acid. For this reason, oxygen has been used to scratch the surface with plasma. It is called the 4th chemical state of the plasma material. When sufficient additional energy is supplied to the gas phase material, the gas ionizes and reaches the plasma state. When the plasma comes into contact with the surface of the material, various reactions can occur on the surface of the material. The changes in the structure of the reaction end surface make the surface ready for surface treatments such as painting, coating and bonding.

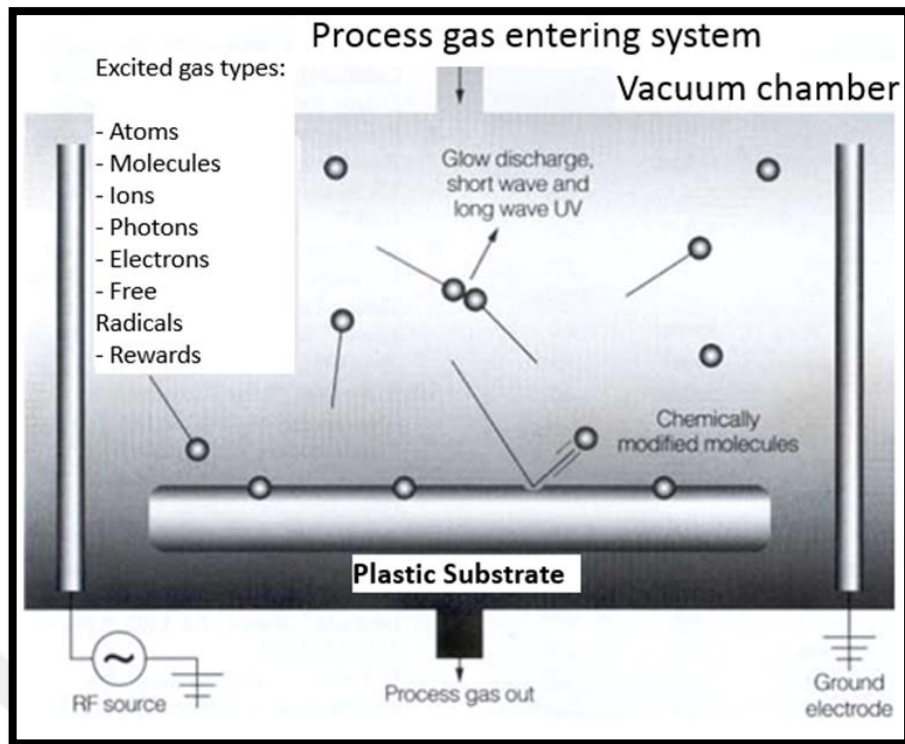


Figure 2.37 Products that occur together with the formation of the plasma phase

During the process of surface modification with plasma, the system is first vacuumed. Subsequently, the gas to be passed to the plasma phase at low pressure is introduced. Gas entering the system; Radio frequency, microwave, direct or alternating current. The energy-loaded plasma phase contains ions, electrons, radicals, halos, and photons in UV with low wavelengths. Plasma components penetrate the polymer surface and change surface properties. Some of the changes that can occur on the surface of the material after plasma processing are shown in Figure 2.38.

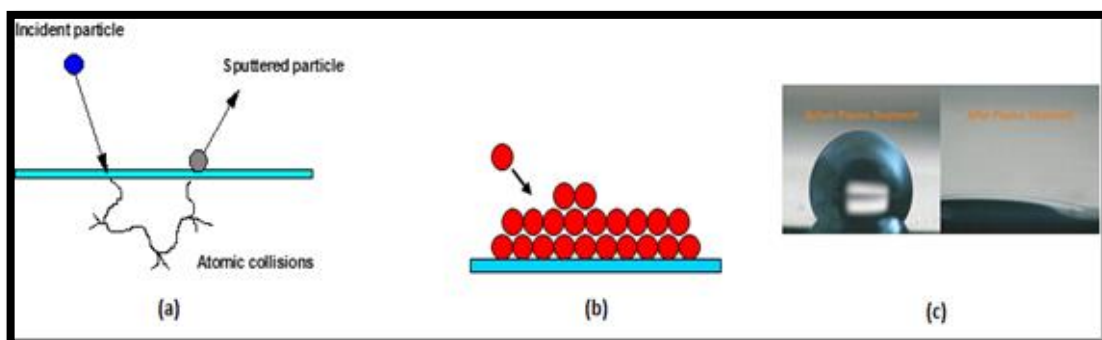


Figure 2.38 Changes that can be made by plasma processing on the surface. (A) Material scraping from the surface, (b) Adding material to the surface, (c) Changing the physical and chemical properties of the surface.



The purpose of our polypropylene plasma treatment is to make the surface both hydrophilic and clean and scratch the surface to be more firm. For this purpose, the polypropylene surface was etched and activated with an oxygen plasma device in the laboratory. O<sub>2</sub> gas at 0.2-0.5 mbar pressure was taken into the system and 100% power was applied for 5 minutes. After the plasma treatment, the previously applied coating procedure was applied. After surface treatment the surface became hydrophilic and the surface chemical structure changed as follows.

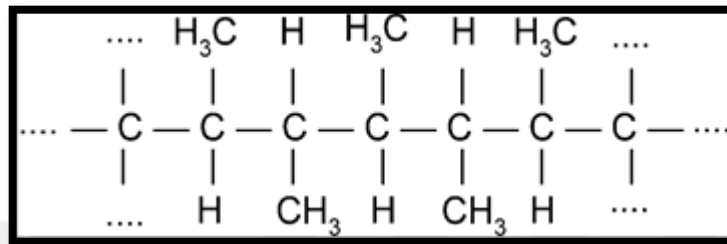


Figure 2. 39 Polypropylene chemical structure

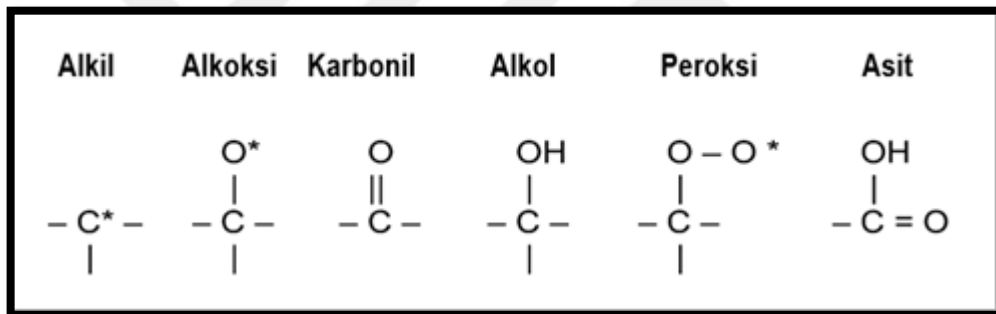


Figure 2.40 Chemical structures formed on polypropylene surface after oxygen plasma treatment

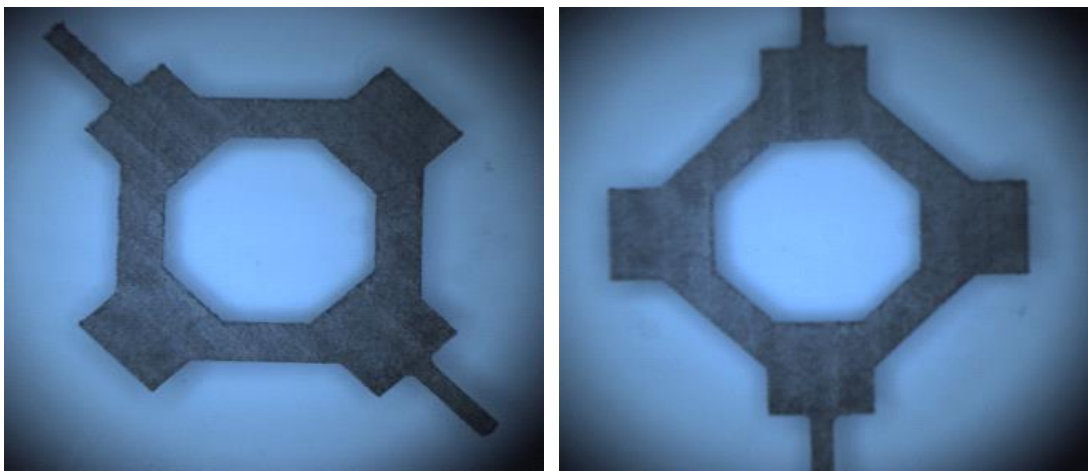


Figure 2.41 After oxygen etch with plasma, the pore-free etched surface is covered

## 2.6.3 MICRO FLUID TYPE PRODUCTION AND MICRO ROBOT INTEGRATION

Basic lithography techniques were used during microfluidic chip production. Basic operations in microfluidic chip production;

- Coating of silicon wafer with photoresist by spin coating method,
- Making masking,
- Removal of the developer related zone,
- PDMS preparation process,

Completion of the microfluidic system by plasma treatment

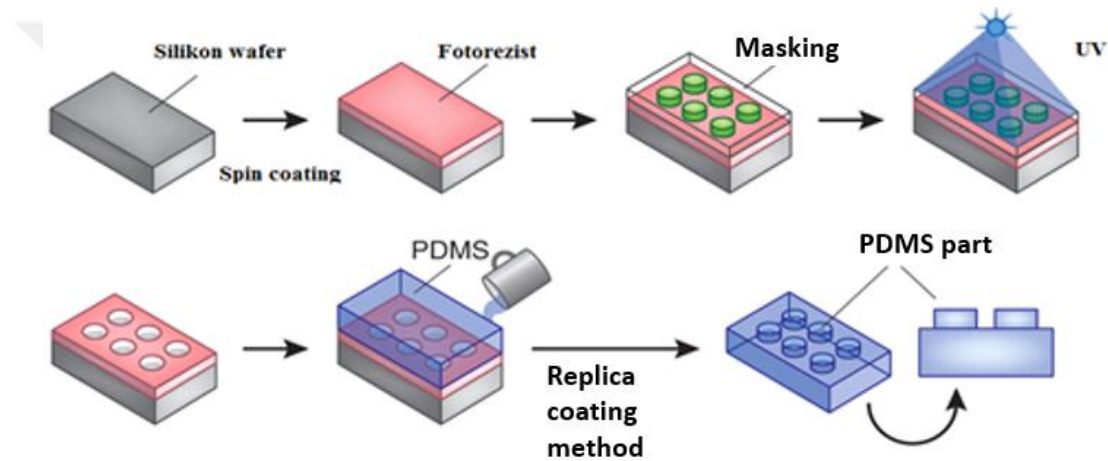


Figure 2.42 Diagram showing the process of extracting the desired patterns onto the PDMS using the replica method [21]

The requirements for this purpose are silicon wafer, photoresist materials, mask fabrication and developer material. The chemicals needed for the preparation of PDMS (SYLGARD 184 Silicone Elastomer Kit, 1,1 Kg) C3 Teknoloji Bilişim Elektronik San. And Tic. Ltd. The Mask production process was realized as a service procurement from ITU Nano Science Technology Research Center. Photoresist materials and wafers are manufactured by Okyay Enerji ArGe Müh. Ltd. Supplied from.

### 2.6.3.1 Masking

In MEMS applications, a radiation source such as UV light is sent onto the patterned photoresist material designed by lithography process. If radiation on the photoresist material is sent to a selected region (by masking) the pattern on the mask can be transferred onto the photoresist material. The characteristics of the areas receiving and

not receiving light will show differences. During the masking process, the patterns that have to be processed on the microfluid are processed on the thin chrome plate. The following Figure 2.43 shows the function of patterning the mask. Mask production operations were realized in the form of service procurement from ITU Nanotechnology Research Center. The design of the micro-fluid drawn by the CAD file is shown in Figure 2.44.

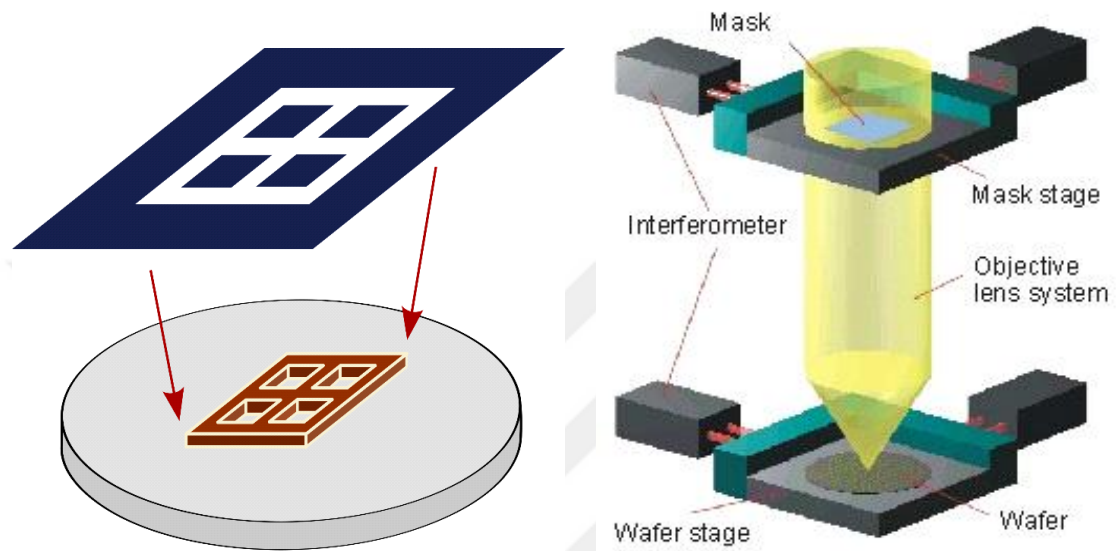


Figure 2.43 The functions of the masks pattern processing process[23-24]

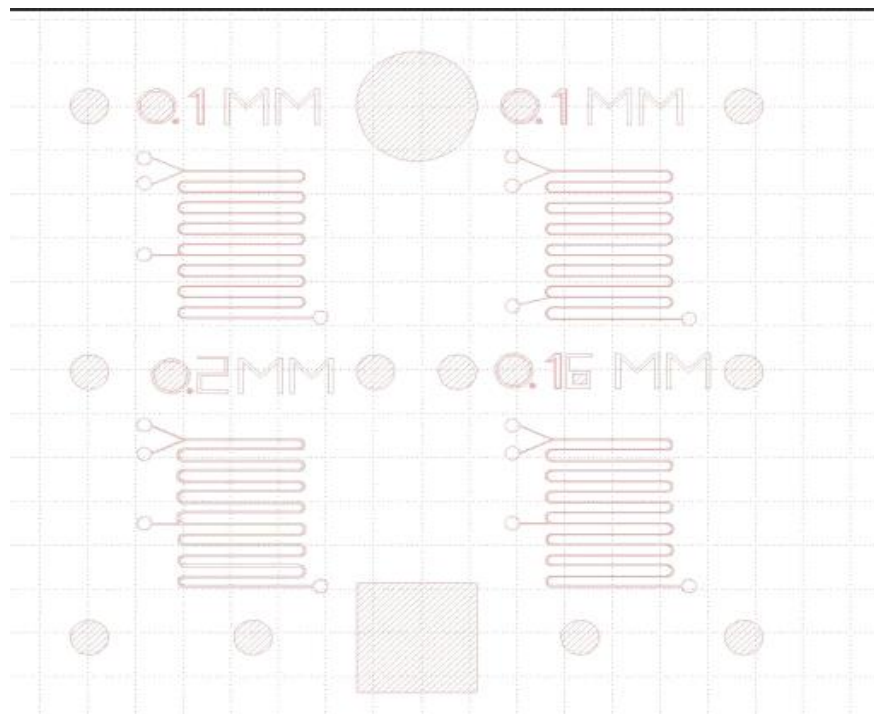


Figure 2.44 Drawing file prepared for mask writing

### 2.6.3.2 Photoresist coating on Silicon Wafer

Spincoating was performed to form the designed patterns. Spincoating is a fast and simple method that allows homogeneous distribution of thin layers in a fluid form on specific surfaces. In general, spin coating is widely used in solvent, photoresist materials and sol-gel production methods.



Figure 2.45 Spin coating working principle[25]

As seen from the above, the photoresist material is poured onto the plate and then spread over the entire surface with increasing rotational speed. With increasing rotational speed, the thickness of the photoresist will decrease. The photoresist AZ40 XT (positive photoresist) we used during microfluidic design was sprayed for 20 seconds at 1500 rpm using a spincoater in the Central Laboratory, shown below, and a coating layer of about 500 microns was obtained.



Figure 2.46 Spin coater used in coating of photoresist on wafer in Central Laboratory

### 2.6.3.3 Develop Process

Since our AZ 40 XT is a photoresist material that we use in our studies, the areas exposed to light by passing UV light through the pattern in the mask will be sensitized by the developer (AZ 400K Developer). The following is the process of forming the desired pattern in the structure after the develop process. In this way, after the develop process, the parts changing the structure due to UV light will be removed from the structure. In our studies AZ 400 K developer from Okyay Energy was used and the SU8 was made ready for mold microfluidic channel production.

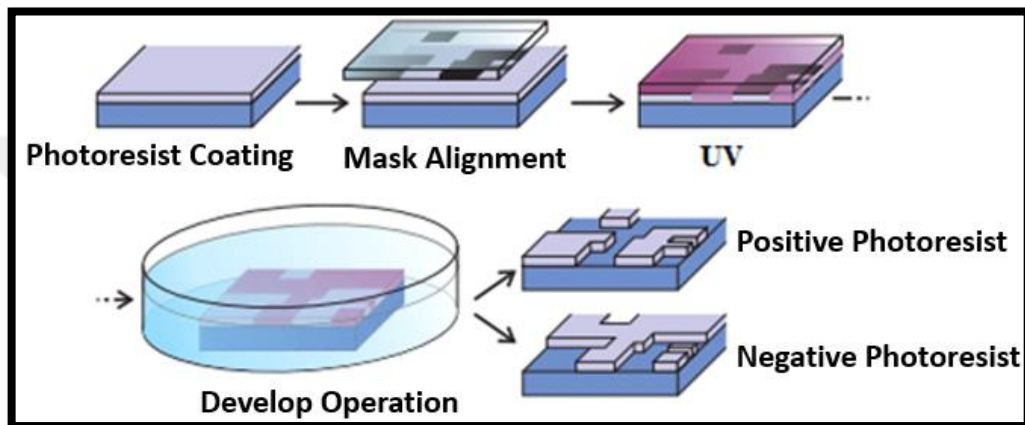


Figure 2.47 Process of obtaining desired patterns after Develop process

### 2.6.3.4 PDMS Preparation Process

Microfluidic channel production is performed with PDMS (Polydimethylsiloxane). A number of pretreatments are required to prepare the PDMS material. The chemistry called PDMS kit consists of Sylgard 184 pre-polymer and a curing agent. For curing, Sylgardar 184 should be mixed with the curing agent in 1/10 ratio. Figure 2. 48 Sylgard 184



prepolymer supplied by the technology company and the curing agent Sylgard 184 are more viscous than the curing agent, so the mixture is carried out in 10-fold increments.

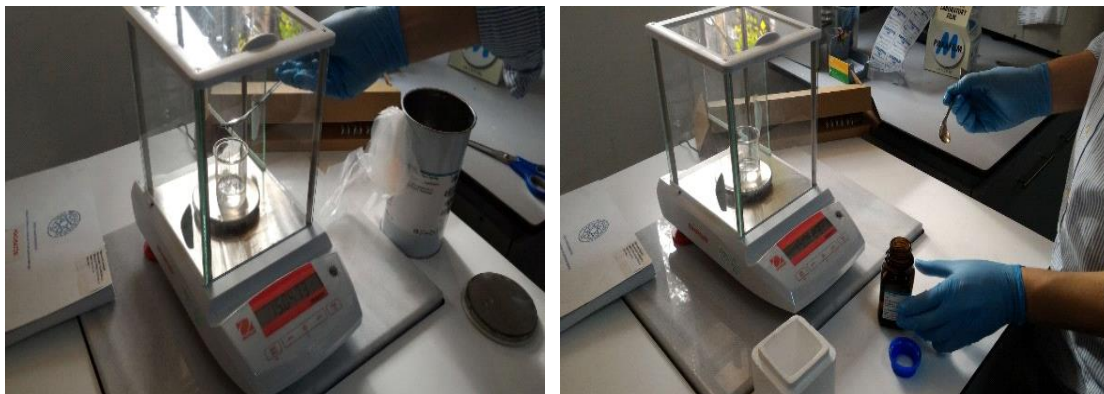


Figure 2.48 Weighing of the curing agent with PDMS at a ratio of 10: 1

Sylgard 184 and curative were weighed and mixed on a precision scale found in the Central laboratory as shown in Figure 2.50. Sylgard 184 weighed 10 to 1 and mixed as shown in Figure 2.49 until a homogenous mixing is achieved in the curing glass beaker.

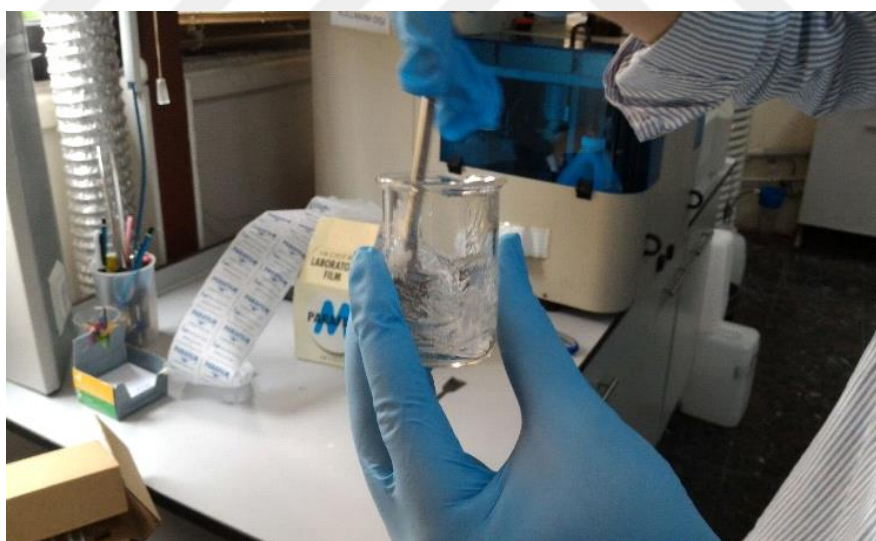


Figure 2.49 Mixing process to homogeneously disperse the curing agent in PDMS

Sylgard 184 forms bubbles in the structure with the curing agent mixing process. Microfluidic chip structure is not required to have any bubbles. For this reason, the air in the desiccator has been evacuated until the bubbles are removed as shown in Figure 2.50.



Figure 2.50 Emptying the air inside the PDMS with the desiccator

It should be seen that no air bubbles remain in the solution removed from the desiccator.

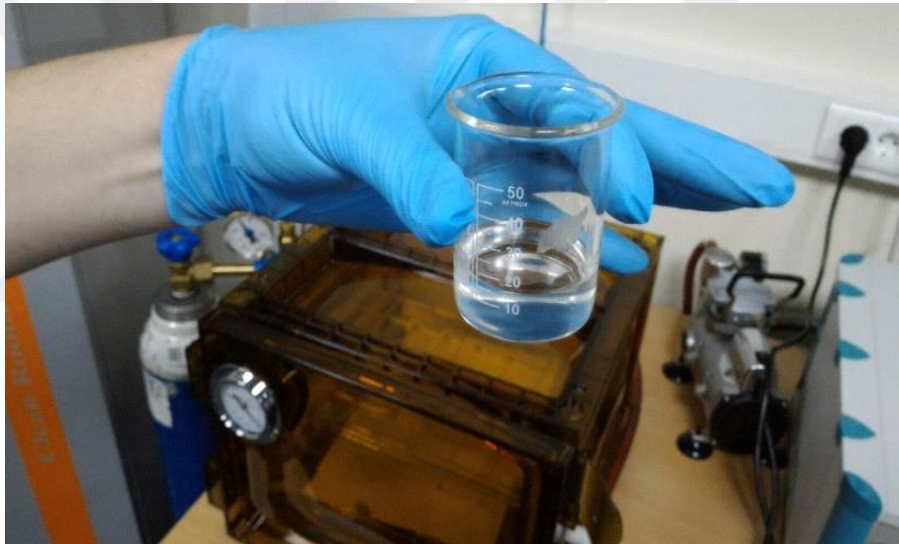


Figure 2.51 Image of the solution from the desiccator

As seen above, the bubbles in the desiccator are removed and the PDMS solution has a clear image. The PDMS material thus prepared is poured onto the prepared mold and is ready to take the shape of the processed pattern.

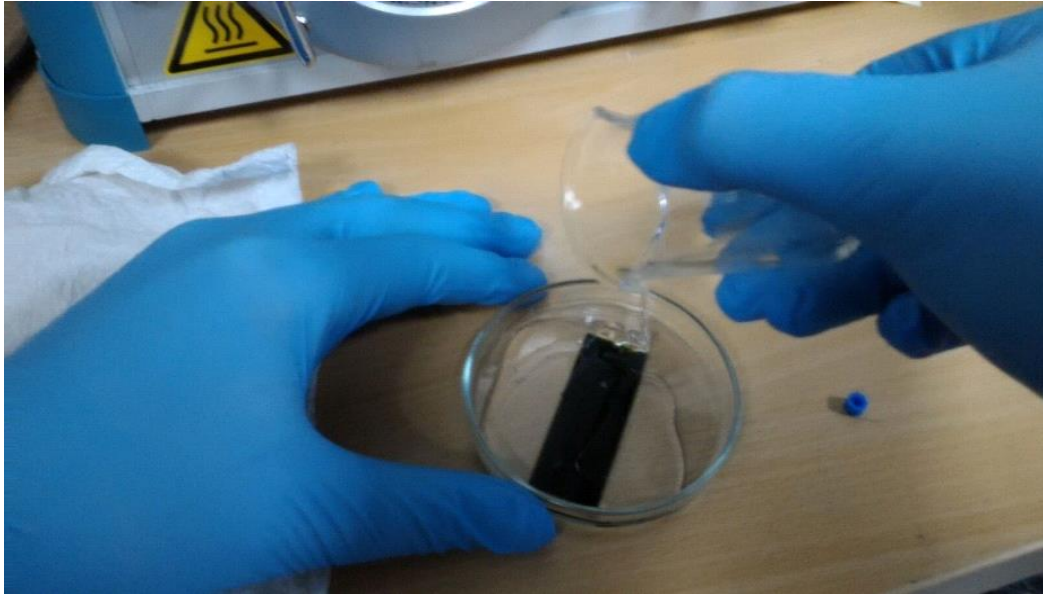


Figure 2.52 Pouring of PDMS prepared on master mold placed in Petri dish

The prepared PDMS is poured onto the mold on which the pattern placed in the petri dish is processed and it should be checked that the air bubble does not remain in the structure during the casting process.



Figure 2.53 Placing the Petri dish in the oven

The Petri dish is placed in the oven and the oven is kept in the oven at 70 °C for 1 hour to complete the curing process. Using the scalpel with the end of the curing, the area where the pattern is treated is cut and separated from the petri dish by holding it with tweezers and edges.



#### 2.6.4 Completion of Micro-fluid Chip Design with Plasma Process

Once the microfluidic structure has been obtained with PDMS, the next step is to attach this structure to the glass slide. Binding was performed using the plasma device. Make sure that the surface of the glass slide is clean. If it is not clean, it should be cleaned with isopropyl alcohol and the drying process should be done by gas blowing with nitrogen gun on the surface. The image of the glass slide is shown as below. Using diamond pens these glasses can be cut to desired sizes.



Figure 2.54 Sliding glass with PDMS on which patterns are processed

After the cleaning process, the glass slide can be glued with the produced PDMS. The adherence of the two materials to each other is provided by a plasma device. The central laboratory has the Diener semi-automatic plasma system as shown below.



Figure 2.55 Plasma apparatus used for bonding PDMS with glass slide

Since the plasma device changed the chemical and physical properties of the surface, it was mentioned in the plasma treatment applied to the polypropylene surface on the non-current nickel coating. In the same way, the oxygen plasma device was used in bonding the PDMS with glass. The PDMS structure contains repeating  $-O-Si(CH_3)_2-$  units. When exposed to oxygen plasma, these silanol groups are combined with the appropriate groups (OH, COOH and ketone) when brought into contact with the other surface. In the case of PDMS and glass, the reaction resultant is Si-O-Si bond as shown below and water is separated from the structure. Contact between the surfaces should be established immediately after the plasma treatment in order for these processes to take place.

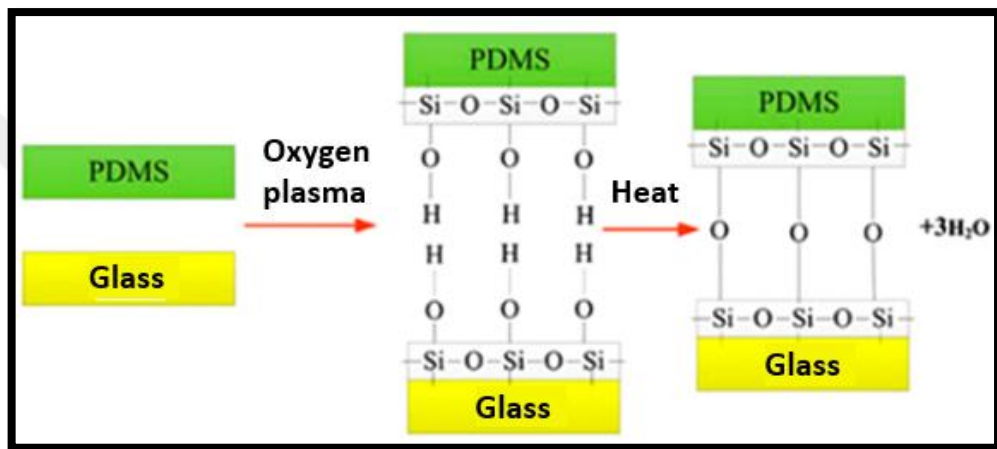


Figure 2.56 Covalent bond between PDMS and glass after plasma treatment

In order to increase bond strength, contact surfaces on hotplate should be kept at 75 C for 5 minutes. As a result of these operations, microfluidic chip production shown below is completed.



Figure 2.57 Image of completed microfluidic chip

The microfluidic chip is fixed with the images taken under the microscope where it is produced with the desired precision in chip design.

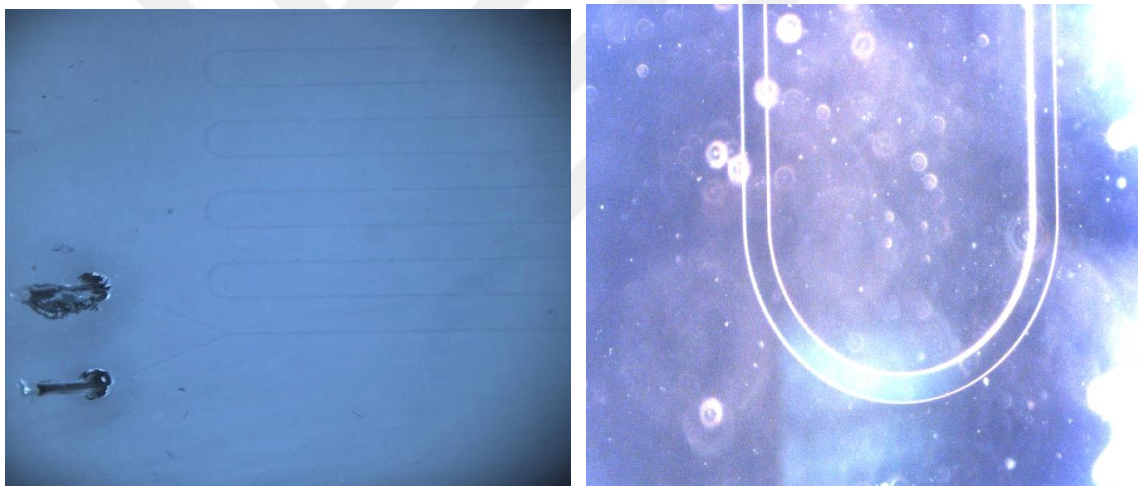


Figure 2.58 Microscopic image of microfluidic chip channels

### 2.6.5 Permanent Magnet Surface Coating

Since most of the micro-robot's target application areas are biomedical applications, the surface of the micro-robot is covered with Polydopamine (PDA), a convenient material for biomedical applications [13]. Accordingly, after adding dopamine dust (100 mg) in 50 ml of purified water, Tris powder (100 mg) was dissolved in the prepared mixture. Together with the beginning of the coating, the color of the solution begins to thicken. With the realization of the coating, the magnet coated with the PDA is separated from the solution by means of another magnet. When the data in Fig. 13 of the pixel obtained from the FTIR spectrum in the magnets 1500-1650  $\text{cm}^{-1}$  and 3200-3600  $\text{cm}^{-1}$  wavelength are

examined, peaks of atomic vibrations of the hydroxyl groups and N-H vibrations in the structure are observed. This demonstrates that the permanent magnet used in the robot's body is successfully coated with PDA for biomedical applications.

### 2.6.6 Microrobot Fabrication

Microrobot production steps are shown in Figure 2.59 AZ 1505, a positive photoresist as a sacrificial layer, is first coated onto the substrate surface as a sacrificial layer (MicroChemicals GmbH). After soft and hard baking, SUEX negative adhesive film was laminated to the surface by rolling 200  $\mu\text{m}$  thick (DJ DevCorp). SUEX was applied by exposure process on film and then pattern development process of micro robot body. Finally, neodymium ( $\text{Nd}_2\text{Fe}_{14}\text{B}$ ) permanent magnet (Supermagnetman) surface of 1 x 0.25 mm in size is coated with PDA, which can be used in medical applications in order to increase biocompatibility, and the presence of coating layer is shown in Figure 2.59. It is confirmed by the FTIR spectrum observed at Z. [13] PDA coated biocompatible permanent magnet micro-robot is placed.

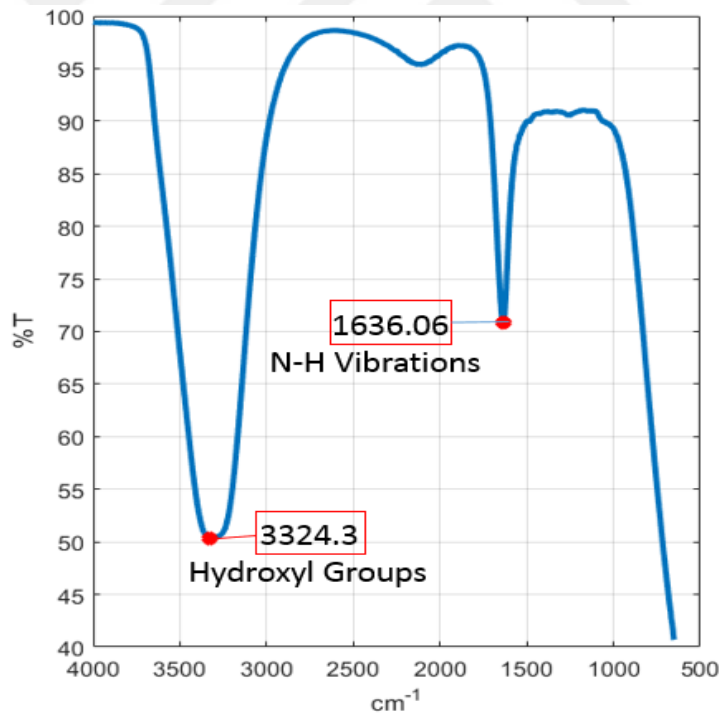


Figure 2.59 FTIR spectrum of magnet coated with PDA. Peak between wavelength of 1500-1650  $\text{cm}^{-1}$  indicates N-H vibrations and peak between wavelength of 3200-3600  $\text{cm}^{-1}$  indicates hydroxyl groups in the structure. This proves successful coating of magnet surface.

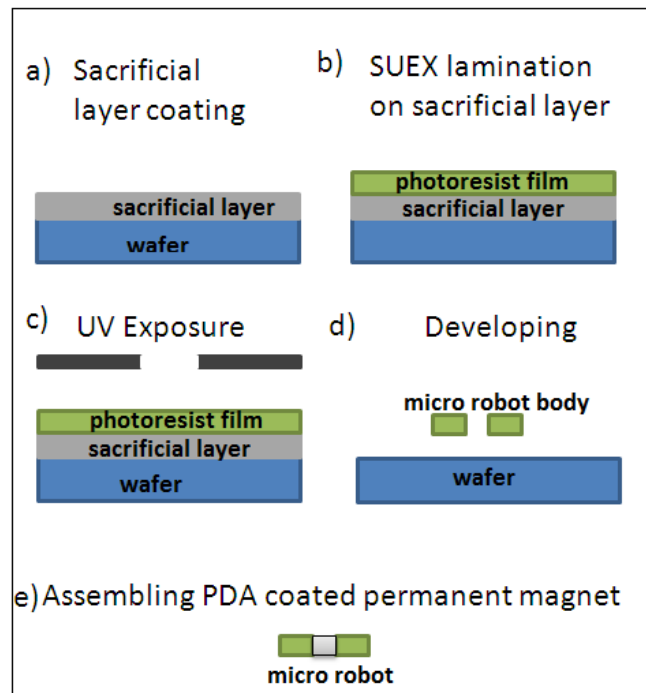


Figure 2.60 Fabrication process of microrobot

#### 3.1 Definiation of Analysis

The effects of the creation of the relevant experimental setup and the results of the mesh selection are shown in the previous section. In this section, all the system analyzes related to the experimental setup which is calculated step by step with numerical calculations are included. Respectively,

- the effect of net magnetic force on the lifting magnet-pyrolytic graphite spacing,
- the effect of changing the levitation height between pyrolytic graphite and micro-robot,
- the fact that the micro-robot is not in the center of the ring magnet (misalignment)
- when the micro-robot is angled rather than parallel to the pyrolytic graphite surface,
- lifting magnet, non-parallel micro robot correction work

are made. In all analyzes, the N-S-N-S representation of the micro-robot and lifting magnet poles and the flux density over them are given in Figure 3.1.

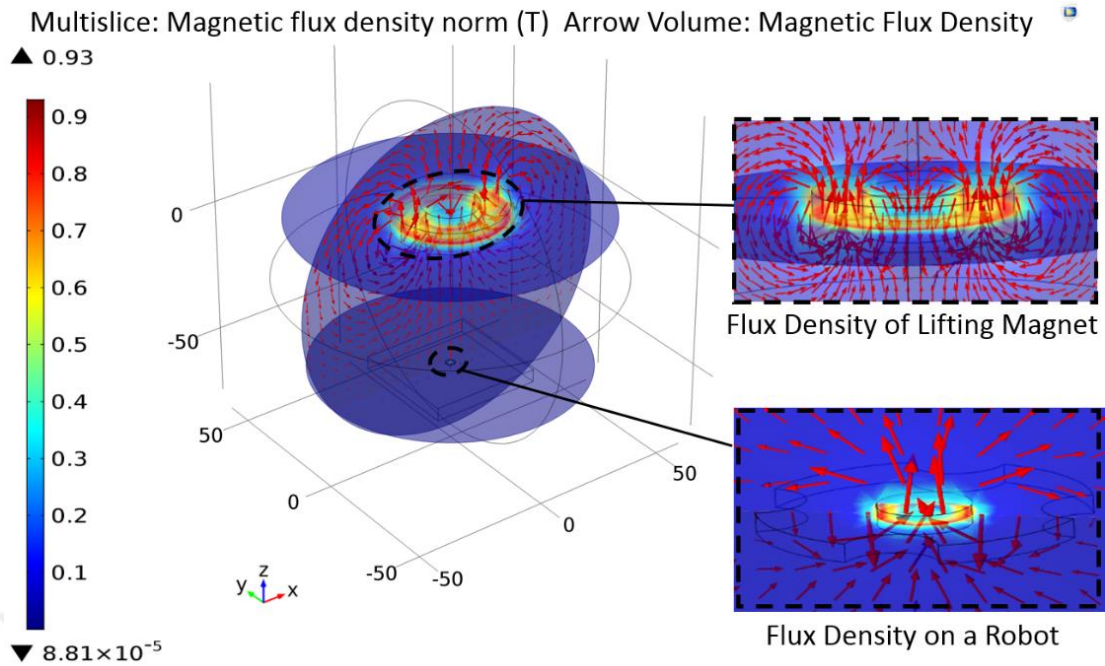


Figure 3.1 The effect of levitation height and lifting magnet distance on net force is calculated. The flux density in the magnet is shown by the [T] unit with the bar on the left side. The distributions of the flux density in the lifting magnet and robot arm are given in detail to the right. The density of the magnets is in the range of 0.7-0.9 T in the corners and middle regions of the magnets themselves. The force lines are frequent in that region because of being more dense in the corner areas. Since the magnet poles are placed in N-S-N-S, it is shown that the corresponding force lines are upwards in the Z-axis.

The distance between lifting magnet and pyrolytic graphite of  $F_{net}$  force value was determined as the result of analysis. At the same time, the effect of levitation distance between pyrolytic graphite and micro-robot was also calculated, depending on the lifting magnet position. The relevant analysis is given in Figure .



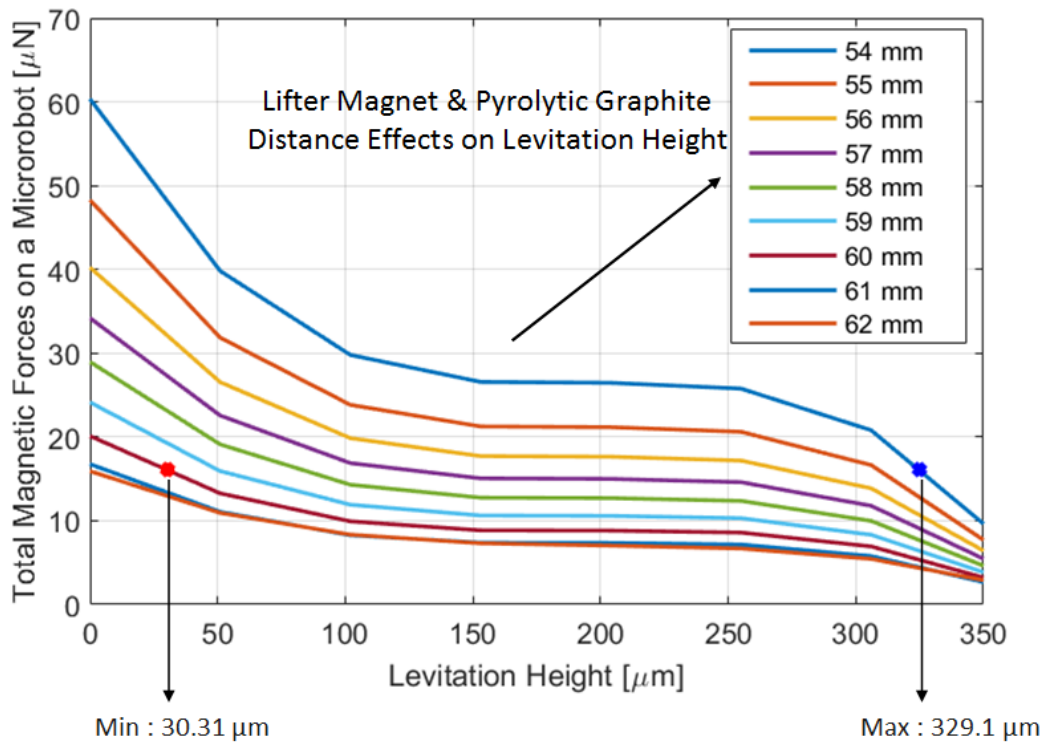


Figure 3.2 According to the analysis made, force graphs are obtained on the micro robot z-axis in the range of 54-58 mm. As expected, a parabolic characteristic has been achieved and the force decreases as the distance increases. At the same time, the Levitation distance in the X-axis showed a decreasing characteristic as the distance increased and a rupture of 0.25-0.3 mm was observed depending on the lifting magnet distance.

As a result of the analysis,  $F_{net}$  shows the point where the forces acting on the robot are zero. In the simulations, lifter magnet heights corresponding to each zero value and levitation height for the robot were obtained.

### 3.2 Z-axis Lifting Magnet Force Calculation via COMSOL

The analysis of the experimental setup was solved using the COMSOL direct solver method to obtain more accurate results. The result of the analysis is calculated by using the maxwell stress tensor and global matrix evaluation method, which effects the robot arm, and the results are the same. The force obtained in the Z direction taken with a 1.201% error by surface fitting is shown in Figure .



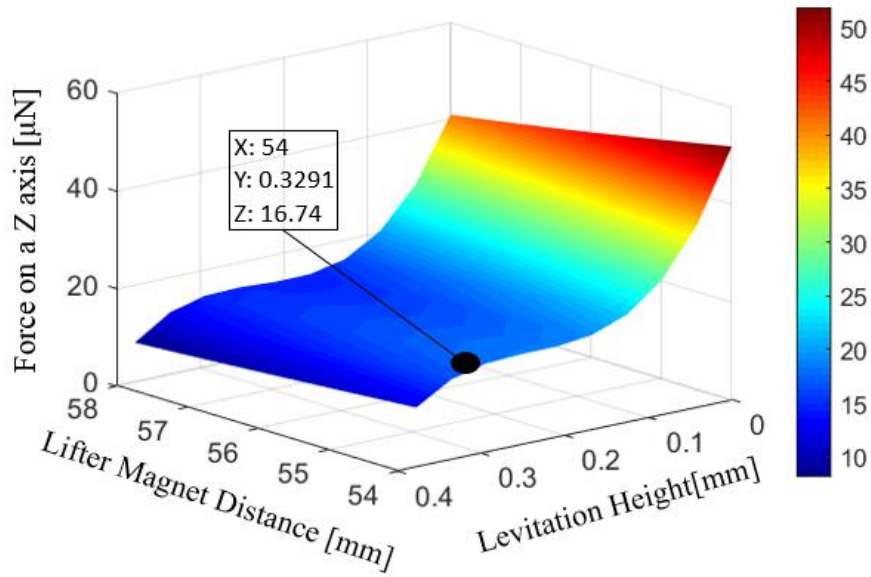


Figure 3.3 According to the parabolic surface graph obtained from the analysis made, when the "Lift Magnet Distance" indicated by Y axis and the "Levitation Height" indicated by X axis increase, the net force generated on the microrobot is reduced. Max: 51.89  $\mu\text{N}$  and min: 8.11  $\mu\text{N}$  force values were calculate

Due to the magnetic flux density, forces are generated in the X and Y axes during the microrobot levitation lower than the Z axis. However, there is no effect for the microrobot levitation besides the force on the Z axis. Thus, the microrobot coming to the same center as the lifter magnet and microrobot will not be able to move in the X and Y directions during levitation. The change in force due to the levitation height for the lifter magnet distance of 55 mm is shown in Figure 3.4.

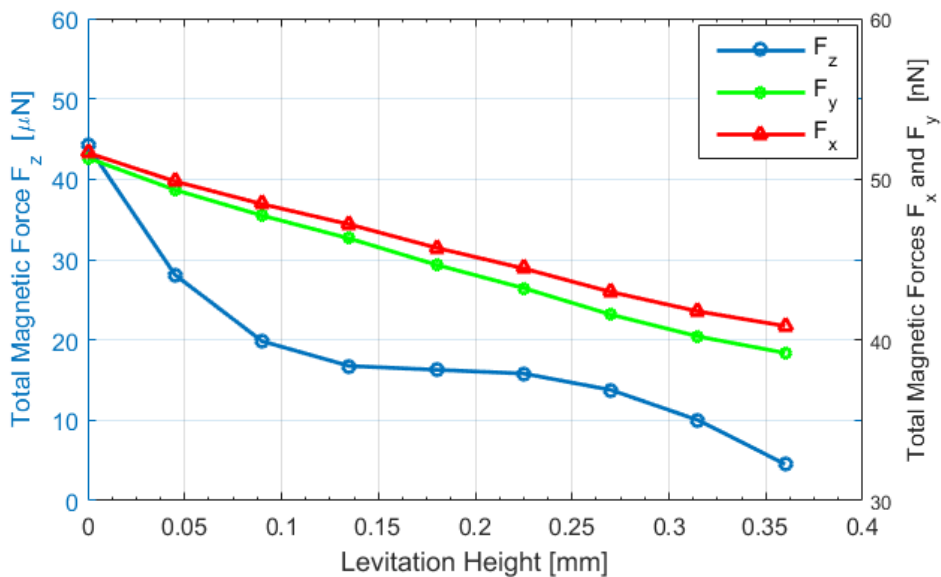


Figure 3.4 It has been shown that the X and Y axis forces are in the 1/1000 ratio according to the force value generated in the Z-axis. Since the acting forces on the X

and Y axes of the microrobot are very small (0.06  $\mu\text{N}$ ), there is no effect on it during the Z-axis levitation.

Along with the drag force obtained, the net force, lift force on the z-axis and microrobot mass act on the microrobot at the same time. Related forces;

$$F_T = F_{\text{net},z} - F_{D,z} + F_{B,z} - F_{r,z} \quad (3.1)$$

and  $F_T$  (total force) are shown as equation (20). In addition, the related force values are given in Table 3.

Table 3.1 Forces action on Microrobot z-axis

Forces	Value	Unit
$F_{D,z}$	0.781	$\mu\text{N}$
$F_{B,z}$	12.788	$\mu\text{N}$
$F_{r,z}$	28.741	$\mu\text{N}$

The required magnetic force  $F_{\text{net},z}$  is calculated as 16.7345  $\mu\text{N}$ . The corresponding force value given in Figure is shown as marked on the surface graph. As a result, the robot is separated from the stabilization point at a levitation height of 329.1  $\mu\text{m}$  according to the analysis. In addition, there is a flat profile with a linear slope at the levitation height: 0.1-0.3 mm. The area outside the region concerned may be called the region of instability; Within this region, the microrobot arm can be stably operated.

### 3.3 Frequency Characteristic

The net force, lift force on the z-axis and microrobot mass act on the microrobot at the same time. Related forces are already expressed in (3.1) and the forces which are exerted on microrobot is shown in Figure 3.5.

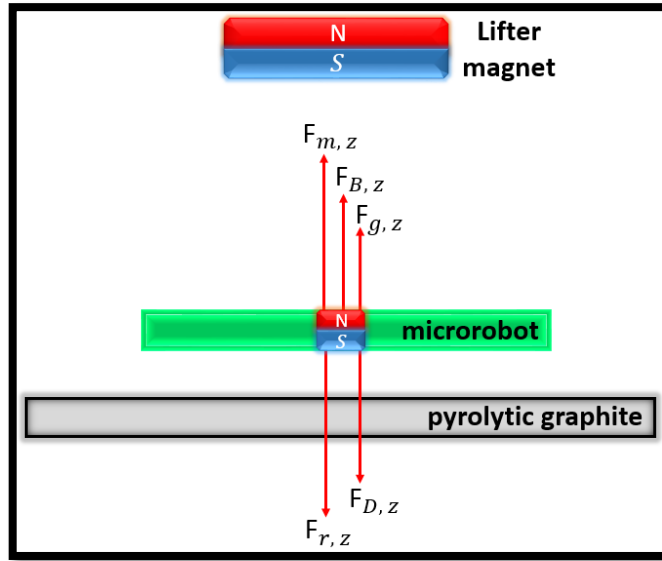


Figure 3.5 Exerted forces on a Z-axis

Depending on the change in the position of the lifter magnet in the Z axis, net force calculated according to the change in magnetic force generated on the microrobot is shown in Figure 3.3.

$$F_T = 0.00113z \quad (3.2)$$

The frequency, which is excited by the vibration due to the 1st order linear equation due to the obtained z position,

$$f_n = \frac{W_n}{2\pi} = \frac{1}{2\pi} \sqrt{\frac{K}{m}} \quad (3.3)$$

For this, the resultant magnetic force linearized around the equilibrium point is shown in Figure 3.6.

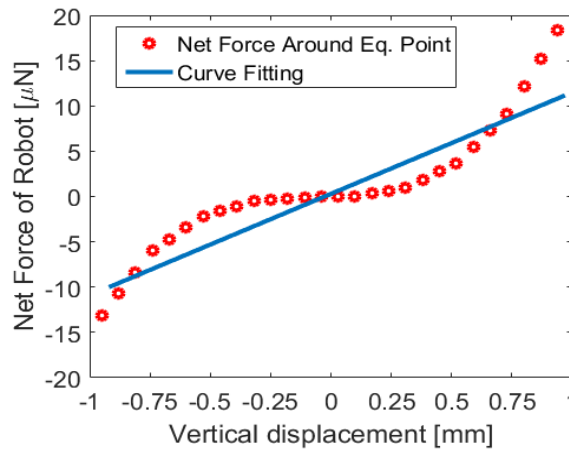


Figure 3.6 Linearization of forces induced by vertical distance change

$K = 1.13$  and  $m = 2,929751 \times 10^{-6}$  put in place together to find natural frequency then  $f_n = 3.1257$  Hz

### 3.4 Head Tilt Analysis

During the movement of the micro-robot, there may be cases where the forces acting on it do not act homogeneously and there is an axial misalignment. This causes the lifting magnet to not be in the same center as the micro-robot. In this case, the magnetic field force lines can not be perpendicular to each other. Thus, according to lifting magnet which is fixed in the first case, micro-robot will not be able to move in parallel to compensate this situation. As a result, the angular movement will show the characteristic instead of parallel movement. On the other hand, the lifting magnet can be considered as moving. In this case, when the micro robot shows head bending due to axial misalignment, the lifting magnet will move angularly to prevent unwanted torque. The corresponding bending and angulation analyzes in these cases are shown in Figure 3.7.

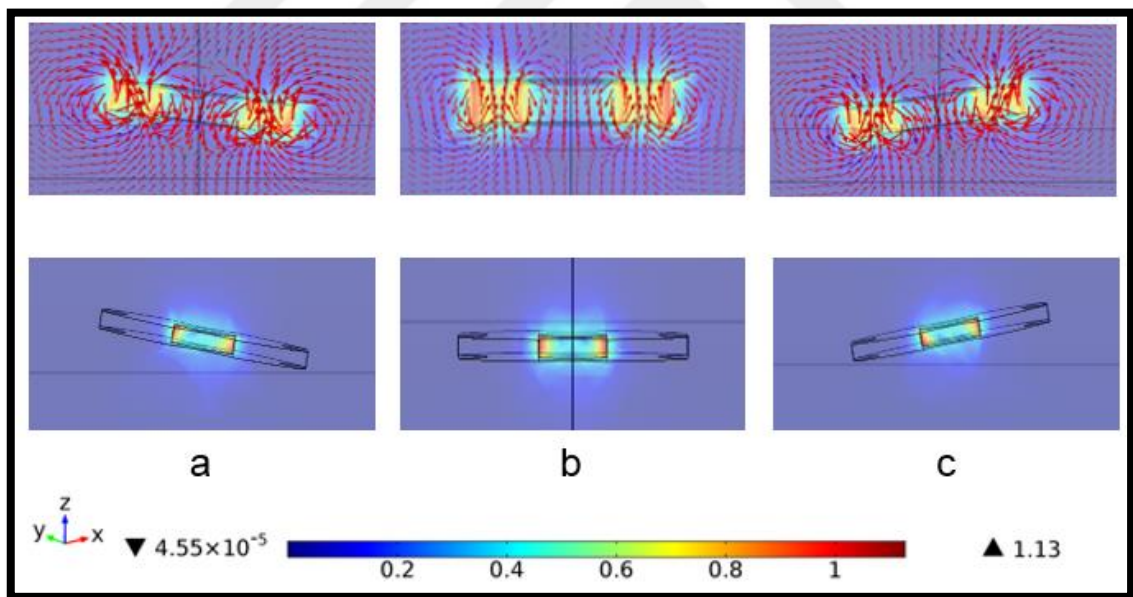


Figure 3.7 (a) Positive angular orientation, (b) Constant, (c) Negative angular orientation. All combinations related to the three cases are calculated parametrically. As can be seen, the flux density is increased in the edge direction where the lifting magnet bends and the force lines become more intense. As expected, the force lines are not symmetrical when compared to (b) in the inclined state. By this feature, it is desired to prevent head tilting by acting on undesired torque in negative direction in micro-robot.

The head tilt analysis in the first case was applied to the micro robot arm for  $\pm 10^\circ$ . In the second case, the lifting magnet is analyzed for its motion. Here, for example, when

the microrobot performs an  $8^\circ$  positive angular orientation, it is calculated that the torque over which the lifting magnet angle is 0. By means of the relevant analysis, it is aimed that the micro robot arm moves parallel to the end of the lifting magnet angle. The two cases and the results are shown in Figure 3.8. Since X and Y axis are symmetrical and their torques are equal, only one axis is shown.

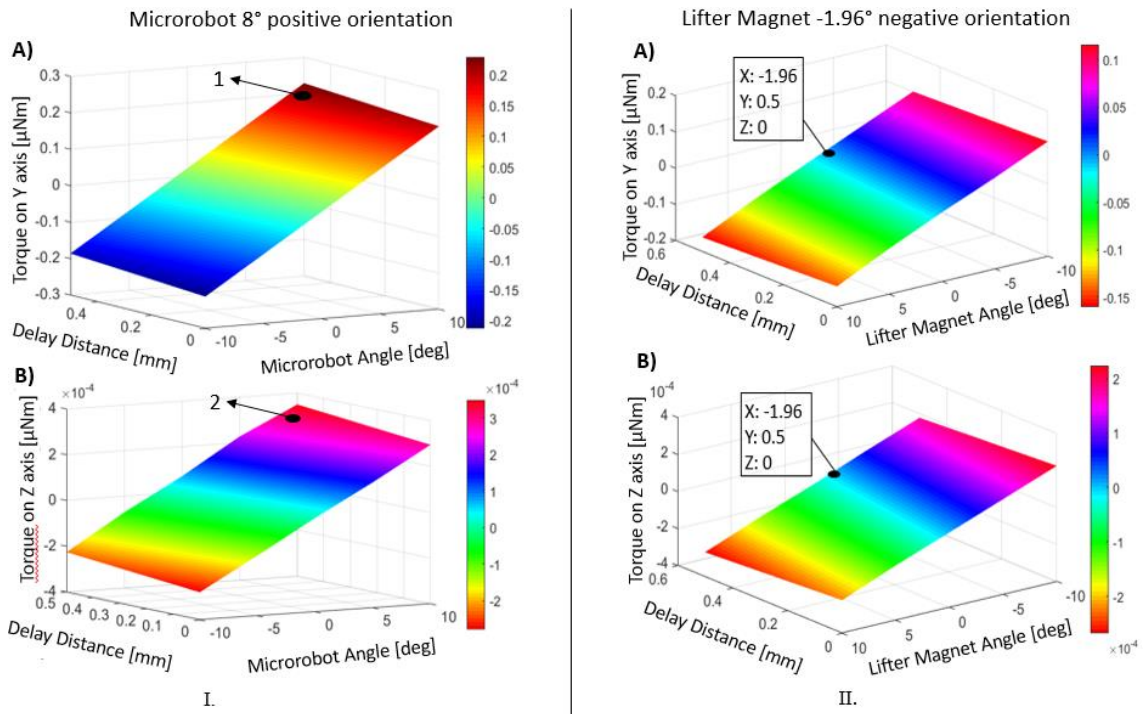


Figure 3.8 I. refers to the torques on the y and z axes, with microrobot  $8^\circ$  positive orientation. In II, the values of the fiber magnet angles, which provide the prevention of undesired torque (0 approach), are also shown for the same axes. It can be seen that symmetrical graphs with linear characteristics and with respect to the  $0^\circ$  axis line show approximately the same torque values in both cases. In this analysis, microrobot torque is calculated when a 0.5 mm misalignment is applied. When the lifter magnet is applied with an angle of  $-1.96^\circ$ , the torque value on the Z axis will be zero and undesired torques will be avoided, as shown in boxes II. (A) and (B)

As a result of the relevant analyzes,

1. The best effective working range of lifter magnet is determined as 56-58 mm.
2. The microrobot's levitation height and detachment points are obtained from figure 11. Accordingly, stable levitation height has been found in the range of 51-306  $\mu\text{m}$  and detachment points is 324.8  $\mu\text{m}$ .
3. Head-tilted motion of a microrobot, it can be controlled by the lifter magnet angular motion.

4. The orientations effects of the lifter magnets are calculated and it shows that microrobot non-parallel motion in the range of  $\pm 10^\circ$  can be controlled by different angular position of the lifter magnet. For example, if the lifter magnet has  $-1.96^\circ$  orientation, it can compensate  $+8^\circ$  tilting of the microrobot.

By discussing all possible situations, the applicability of the relevant design has been demonstrated.



## CHAPTER 4

---

### EXPERIMENTAL STUDIES

Implementation of experimental setup; it contains a microrobot positioned in a DI water container with pyrolytic graphite on its surface. The ring magnet (lifter-magnet) on which the magnetic force required for levitation is obtained is on the vessel. To achieve stable and micro-precision levitation, it is necessary to position the lifter magnet on the DI water tank parallel and rigid. In order to perform levitation and precise position control at the micro level, a PI Micro Stage (M-126.PD2 / 20x20x20 mm) with 3-axis linear micro-movement sensitivity was placed on the Z axis. A manual micro-stage was used to position the DI water container parallel to the floor and to move the 3 axes when necessary. Nano-sensitive laser distance sensor (optoNCDT-ILD2300-50) is preferred for instant measurement of levitation height within the system. At the same time, microscope camera-lens system (Olympus SZX-7 and PointGrey GS3-U3) positioned perpendicularly from the side profile to observe the mechanical contact of the microrobot with the pyrolytic graphite surface. The whole experimental setup where the levitation and motion characterization experiments of the microrobot are performed is shown in Figure .

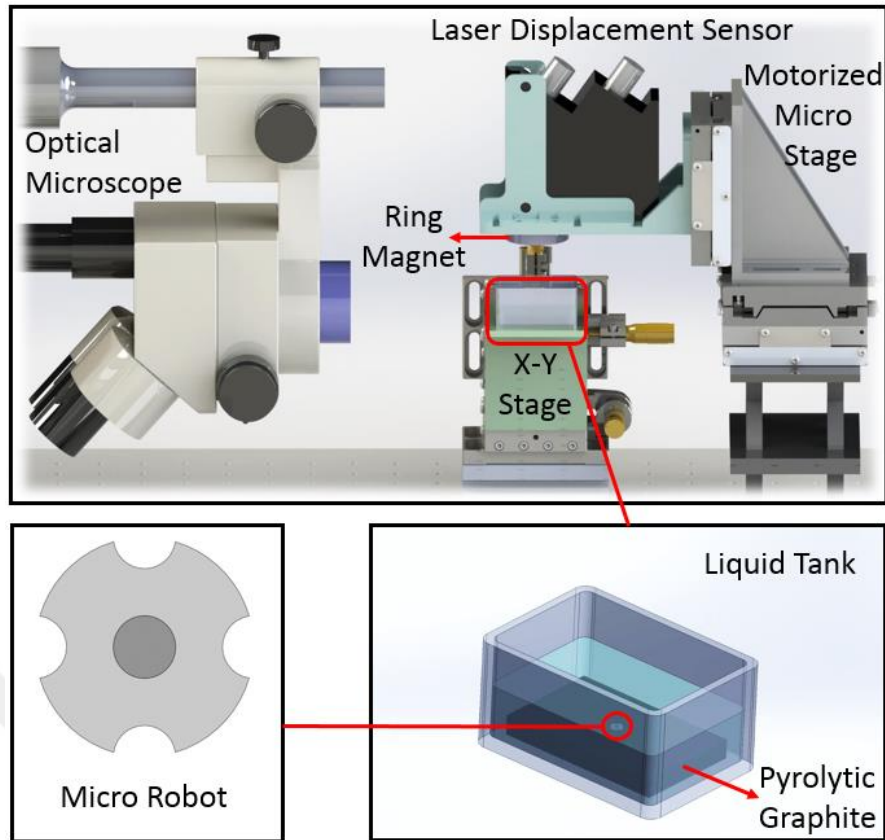


Figure 4.1 The control of the Micro Stage, which performs the motion as a ring magnet 3 axis linear, was realized through an interface created with C#. Camera image is transferred on the same interface. The reading of the data of the laser distance sensor is taken through the laser's own interface.

#### 4.1 Levitation characterization

The microrobot is made levitate by the movement of the lifter magnet in the order of microns along the Z axis. It exhibits a levitation characteristic depending on the magnets and properties used within the system. The reason for using a ring-shaped lifter magnet is that it has a hollow structure required for laser measurement. Because of the gap in the middle of the ring structure (20 mm diameter), the laser is aligned with the microrobot arm in the vertical position. The PI Stage, which we designed through the system interface, was moved by 50  $\mu\text{m}$  on the Z axis, followed by 10  $\mu\text{m}$  steps as the first levitation occurred. When the microrobot is in the levitated state, the behavior of the lifter magnet in the motion range of about 6 mm is observed. The measurements made according to the distance between the different levitation heights and the microrobot positions are given in Figure . In addition, as a result of experiments with a certain height of the obstacle, the robot showed the ability to move 3 axes in a fluid.



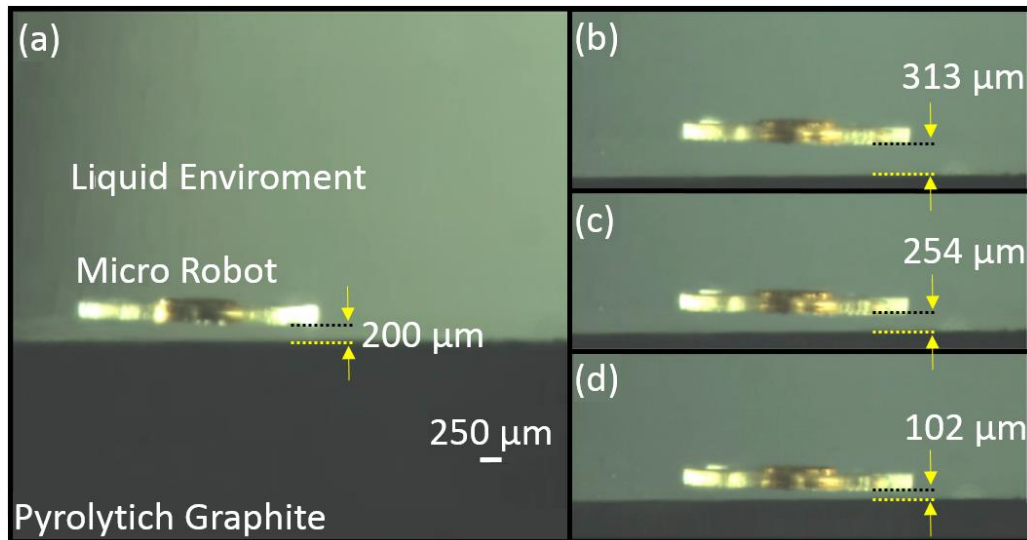


Figure 4.2 The experiment was observed by recording the position data with the laser distance sensor in each movement step. The microrobot has been shown to operate at a maximum stabilization level of 333  $\mu\text{m}$  in the current system. Subsequently, the resultant force acting on the microrobot was acting in the upward direction, indicating that the robot departed from the stable region and moved upwards under the influence of the magnetic force.

In addition, the change in the 6 mm between the lifter magnet and the pyrolytic graphite also affects the levitation height of the microrobot, as shown in Figure 4.3.

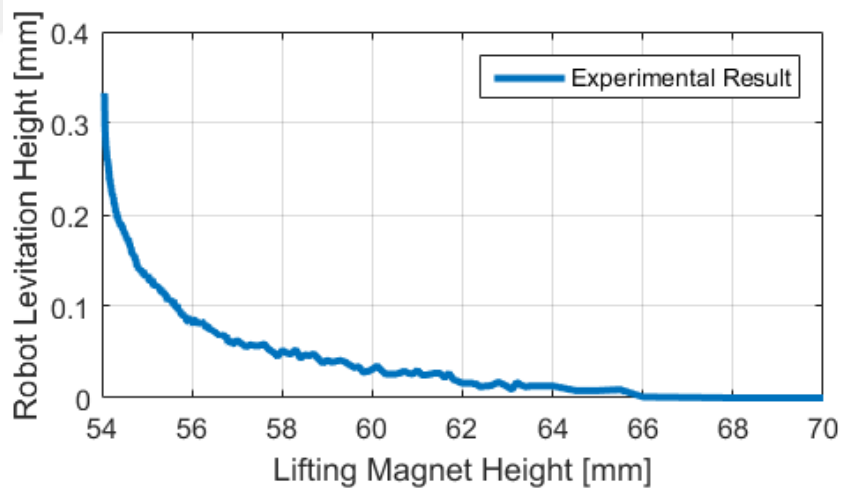


Figure 4.3 Prior to the critical region where the lifter magnet effect increased, the microrobot showed a levitation elevation with linear characteristics similar to the simulation results.

Considering the objects and motion field to be manipulated by the microrobot in lab-on-a-chip applications, the 333  $\mu\text{m}$  levitation height obtained from the experimental results is sufficient. In Figure 4.2, it is a characteristic of our existing system that we have designed. The diamagnetically levitated method we have developed may vary according

to the system requirements to be applied. The proposed manipulation method allows microrobot design and driving magnet properties to be modified to achieve specific levitation intervals for different anticipations.

#### 4.2 Phase difference characterization

As a result of experimental studies and observations made; The microrobot has the ability to precisely move and position in the mechanical non-contact situation. Microrobot performed smooth motion at the desired speeds and ending its movement at the point where it would be coincident with the ring magnet as expected. Thus, the microrobot with diamagnetic levitation proved to have a lossless positioning capability. Although the micro-robot levitated is mechanically non-contact, it is exposed to fluid-induced frictional resistance in the fluid. Besides, it has an inertia originating from its own mass. Because of all these factors, the microrobot follows the motion trajectory in the "X-Y" axes with a delay in relation to the ring magnitude, ie, the enter of the motion in a misaligned manner Figure 4.4. The error state (delay) from this center is defined as "Phase Difference".

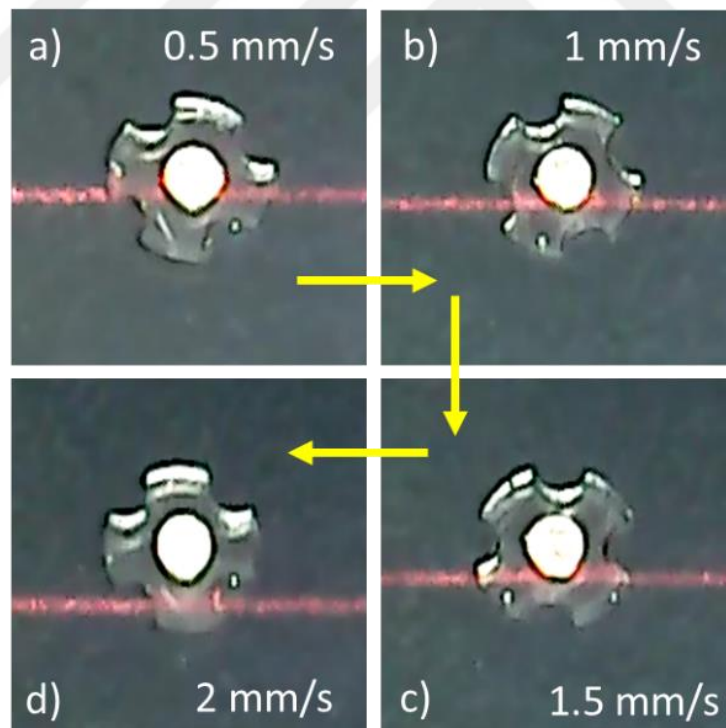


Figure 4.4 Depending on the microstage speed change, the delay is shown. The red line belongs to the laser which is sent from the center of the lifter magnet. Acceleration has been shown to increase with delay as expected.

The phase difference is a parameter that is controlled by the system interface and depends on the speed of the moving magnet on the micro stage. As the speed of progression increases, the phase difference increases as a result of experiments. The fact that the phase difference on the move does not cause a situation to prevent precise speed and position control of the microrobot. The robot follows the same trajectory at the same speed as the ring magnet during its movement. After the motion is finished, the microrobot ends its movement in the concentric state with the ring magnet. The amount of delay due to the microstage speed is experimentally determined and shown in Figure 4.5.

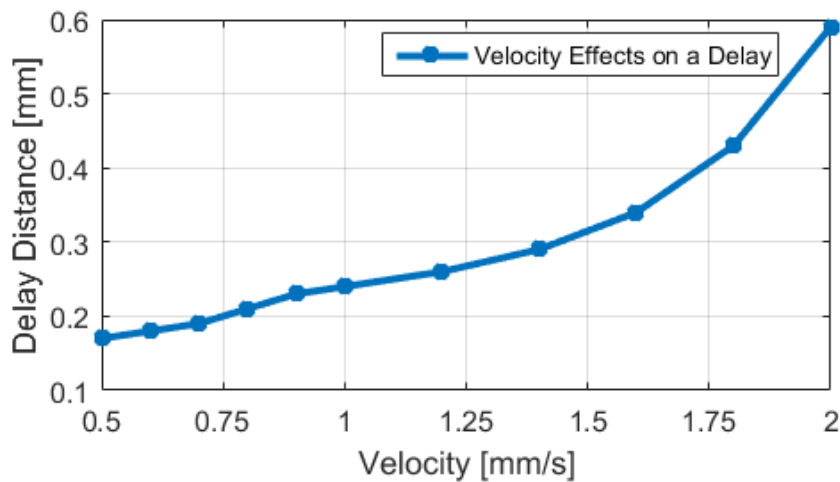


Figure 4.5 At higher velocities of about 1.4mm / s, the phase difference is characterized by an exponential increasing trend and at lower speeds with linearized phase difference characterization as expected. It is obvious that the phase difference falls below 150 $\mu$ m as the same linear change is likely to continue even at small speeds of 0.5mm / s. This is an indication that non-delayed positioning can be performed by neglecting the phase difference at the speed requirements of the nanometer range, which will be needed especially in lab-on-a-chip applications.

### 4.3 Pre-defined Trajectory Tracking

The movement of the micro-robot in a mechanical non-contact manner is observed in the "X-Y" axes at a constant levitation height. Accordingly, the system interface has been coded into sinusoidal, circle motion orbitals in which necessary variables can be adjusted and experimentally applied in Figure 4.6.

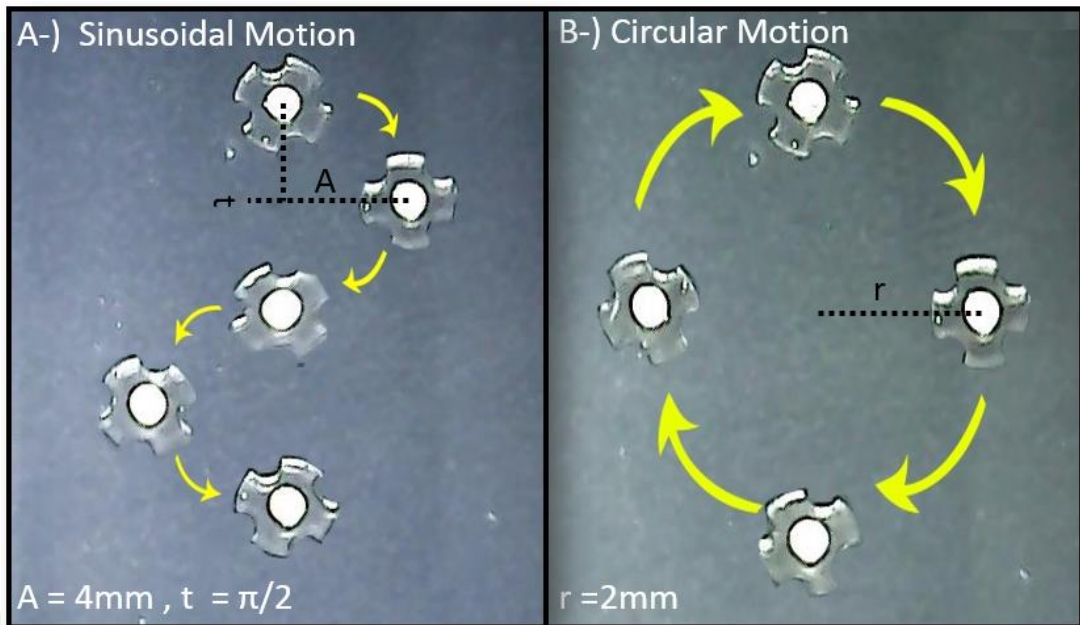


Figure 4.6 The sinusoidal and circular orbit levitation elevation has been successfully tracked to remain constant. A) shows the sinusoidal trajectory followed by the signal input given as amplitude  $A = 4\text{ mm}$  and  $t = \pi/2$ . B) a circular orbit with a radius of  $2\text{ mm}$  was followed.

In addition, the vision of being able to move precisely without interference from an obstacle is shown in Figure 4.7.



Figure 4.7 The robot has started to move at the same height from the point of the block. Then it is raised upwards by being levitated on the Z axis precisely. By passing over the micro robot as parallel to the obstacle; At point D, it is lowered again in the Z axis.

#### 4.4 Head-Tilting Reaction

The resulting phase difference causes vectorwise directional changes in the resultant magnetic field forces acting on the micro-robot. As a result of observations we made during experimental studies; It was observed that the micro-robot performed a head ending motion in the direction of movement in the case of phase difference occurrence Figure 4.8.

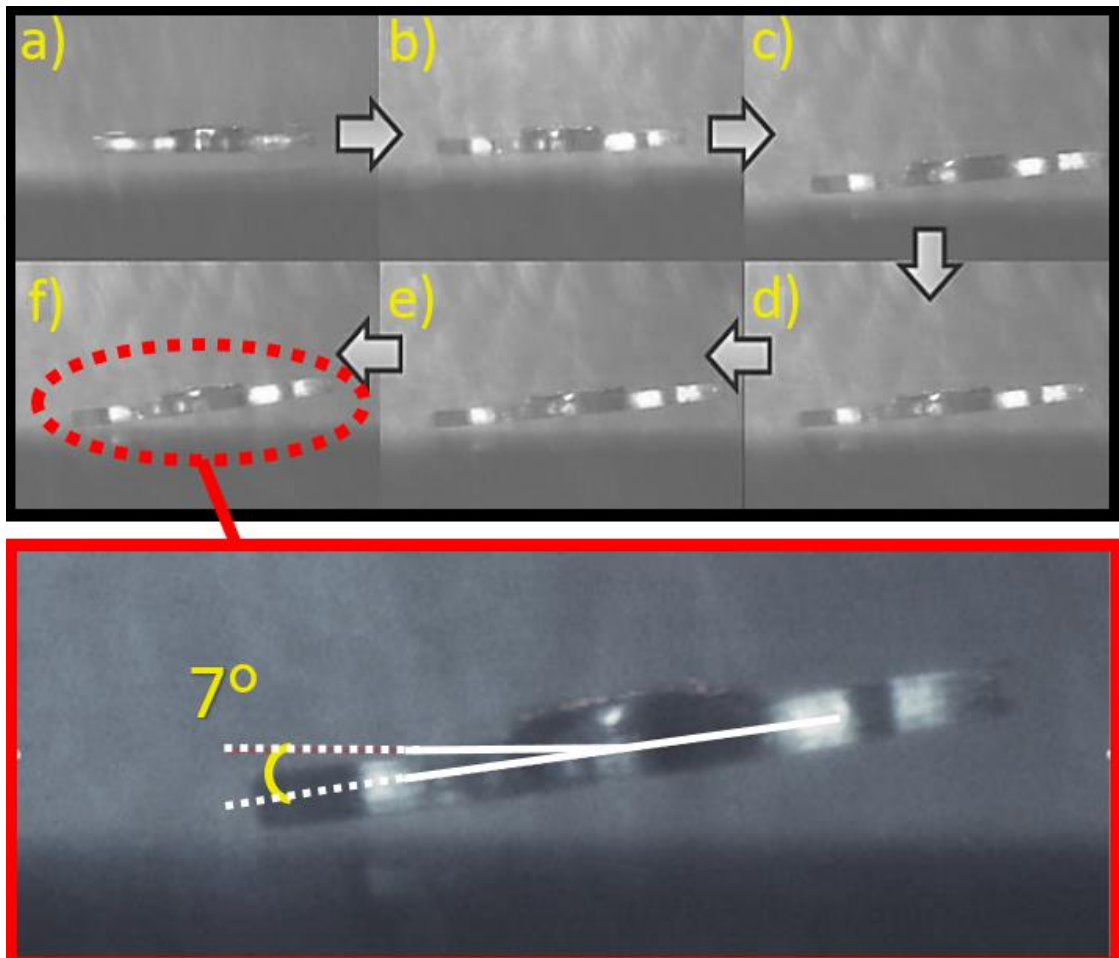


Figure 4.8 The cause of the head tilt reaction is to suspend the directional changes of the vector field forces acting on the microrobot. The head tilt angle is a parameter proportional to the phase difference. The increase in phase difference also causes an increase in head tilt angle. As can be seen in figure, in the experimental studies performed, the head tilt angle of  $7^\circ$  is displayed.

### DISCUSSION and CONCLUSION

#### A. General

In this system, which we designed with our team, we offer an innovative micro-UFO working mechanism suspended by diamagnetic levitation, unlike other studies. In the system we designed, the micro-UFO was able to successfully track the maximum range of motion of the PI stage at 500 nm through the lifter magnet after it was suspended at certain heights. With the use of nano-positioner with higher motion sensitivity, it is obvious that higher resolution position capabilities can be achieved successfully. Another innovative feature of the designed micro-UFO, which is different from micro-UFOs providing permanent magnet motion, is that it has a more suitable design for biomedical applications. PDA coated micro-UFO also have the ability to prevent contamination.

#### B. Levitation on Z-axis

It is possible to control the movement of X-Y-Z axes within the microfluidic channel of the micro-UFO. By means of finite element analysis in COMSOL, the levitation height limits of the micro-UFO were successfully determined and compared with the experimental results. Magnetic analysis showed that the micro-UFO showed linear surface behavior in the range of 90-280 $\mu$ m according to surface force graph on Z axis direction. Experimentally, it was determined that the current micro-UFO levitation characteristic has an unstable structure in the range of 0 to 30 microns and 290 to 333 microns and the stable working range of the system is in the range of 30 to 290 microns. Accordingly, when compared with the experimental results, the analysis results were found to be within the experimental limits. If the analytical findings obtained are used on the system, it has been proved that safe and linear behavior range can be studied.

### **C. Drag Force - Lifter Magnet Effects**

The distance between the lifter magnet and the pyrolytic graphite is calculated numerically as well as the range of the levitation work. Compared to the experimental results, it has been shown that the working range of 54-58 mm is common with current experimental setup. Although the micro-UFO can be controlled beyond this range, it has been shown that the linear zone is the optimal working range. As shown in the experimental results, the numerical analysis result showed that the micro-UFO in the determined range has more stability characteristic. The result of the drag force analysis is that the viscous effect of the water is not much higher than micro-UFO. It is calculated that the drag force max value is about 5% of the force required to levitate the robot. If micro-stages' operating speed range is set to  $\pm 2$  (mm / s), It is estimated that the drag force will be less than 0.75%. Thus, we can say that the drag force can be neglected and the system can be linearized as a result of neglecting the drag force effect. For the future studies, a linear controlling technique can be potentially utilized in this application.

### **D. Center Alignment**

Precise position control is also provided on the x and y axes of the micro-UFO in the direction of the experimental data. The mobility of the micro-UFO has been tested in motion trajectories that may be encountered in different scenarios and work areas. For this purpose, the micro-UFO has followed the sinusoidal and circular orbits with high success, besides the linear motion. As you can see in COMSOL analysis, during the levitation of the micro-UFO; it is calculated that forces generated in the X and Y directions is about 1/1000 less than Z axis. Therefore, predominant Z axis force can not be effected by X and Y axes forces dramatically and levitation height is not change during motion of the micro-UFO. Furthermore, it always centralized with lifter-magnet poles that provides different movement characteristics and trajectory tracking.

### **E. Phase Difference**

According to levitation characteristics with the help of motorized microstage motions, the phase difference during the movements is seen as a factor that will force us to do real-time position control. On the other hand, for many biomedical applications, nanometric speeds are being used. In this case, the phase difference was found to be in negligible level, as a result of our experimental studies. According to the analysis and experimental results regarding the phase difference, the respective torque and force values remained

almost same and were not affected. The microstage is moving at a maximum speed of 2 mm / s. In this case, a delay of 0.6 mm is calculated and shown in figure14. It can be seen that the calculated phase difference is very small ( $1/80$ ) compared to the lifter magnet size. Thus, it is observed that there will be no effect on the magnetic force and torque produced. In addition, when the phase difference is high, the head tilting reaction observed at the significant levels is likewise observed at negligible levels within the operating speed requirements of the applications. However, the possibility of giving capillary damage to the surface boundaries of the head tilt reaction can not be overlooked especially in low run-up working conditions. In this regard, in future studies, control-based studies will be carried out to prevent the head tilt reaction.





## **CHAPTER 6**

---

### **FUTURE WORKS**

It is aimed to perform autonomous control in addition to the analysis studies made. These results will be expressed mathematically for the system which affects force and torque values such as changing lifting magnet distance, levitation distance, bending angles in the analysis. According to the mathematical expression, systematic mathematical model will be created and dynamic effects will be calculated. Depending on the lifting magnet distance that can be selected as the control input, advanced control techniques will be tested on the system. It is aimed to demonstrate the controllability of the system by comparing the results of numerical calculations as a result of the force signal.

## REFERENCES

---

- [1] Fusco, S., Sakar, M. S., Kennedy, S., Peters, C., Bottani, R., Starsich, F., Mooney, D. (2014). "An Integrated Microrobotic Platform for On-Demand, Targeted Therapeutic Interventions", *Advanced Materials*, 26(6): 952-957.
- [2] Squires, T. M., and Quake, S. R. (2005). "Microfluidics: Fluid physics at the Nanoliter Scale", *Reviews of Modern Physics*, 77(3): 977.
- [3] Hagiwara, M., Kawahara, T., Yamanishi, Y., and Arai, F. (2010). "Driving Method of Microtool by Horizontally Arranged Permanent Magnets for Single Cell Manipulation", *Applied Physics Letters*, 97(1): 013701.
- [4] Zhang, T., Zhang, M., and Cui, T. (2011). "Microfluidic Valves Based on TiO<sub>2</sub> Coating With Tunable Surface Wettability Between Super Hydrophilic And Super Hydrophobic", In *Solid-State Sensors, Actuators and Microsystems Conference (TRANSDUCERS)*, 5-9 June 2011, Beijing, China, 306-309.
- [5] Nelson, B. J., Kaliakatsos, I. K., and Abbott, J. J. (2010). "Microrobots for Minimally Invasive Medicine", *Annual Review of Biomedical Engineering*, 12: 55-85.
- [6] Feng, L., Ichikawa, A., Arai, F., and Hagiwara, M. (2012). "Continuous Eucleation of Bovine Oocyte by Microrobot with Local Flow Distribution Control", In *Manipulation, Manufacturing and Measurement on the Nanoscale (3M-NANO)*, 29 Aug.-1 Sept. 2012, Shaanxi, China, 59-64.
- [7] Zhang, L., Abbott, J. J., Dong, L., Kratochvil, B. E., Bell, D., and Nelson, B. J. (2009). "Artificial Bacterial flagella: Fabrication and Magnetic Control", *Applied Physics Letters*, 94(6):064107.
- [8] Gultepe, E., Randhawa, J. S., Kadam, S., Yamanaka, S., Selaru, F. M., Shin, E. J., and Gracias, D. H. (2013). "Biopsy with Thermally-Responsive Untethered Microtools", *Advanced materials*, 25(4):514-519.
- [9] Tabatabaei, S. N., Lapointe, J., and Martel, S. (2011). "Shrinkable Hydrogel-Based Magnetic Microrobots for Interventions in the Vascular Network", *Advanced Robotics*, 25(8):1049-1067.
- [10] Zhao, X., Kim, J., Cezar, C. A., Huebsch, N., Lee, K., Bouhadir, K., and Mooney, D. J. (2011). "Active Scaffolds for On-Demand Drug and Cell Delivery", *Proceedings of the National Academy of Sciences*, 108(1):67-72.

- [11] Zhang, X. Z., Lewis, P. J., and Chu, C. C. (2005). "Fabrication and Characterization of a Smart Drug Delivery System: Microsphere in Hydrogel", *Biomaterials*, 26(16):3299-3309.
- [12] Ichikawa, A., Arai, F., Yoshikawa, K., Uchida, T., and Fukuda, T. (2005). "In Situ Formation of a Gel Microbead for Indirect Laser Micromanipulation of Microorganisms", *Applied Physics Letters*, 87(19):191108.
- [13] Fukuda, T., Kawamoto, A., Arai, F., and Matsuura, H. (1994). "Mechanism and Swimming Experiment of Micro Mobile Robot in Water", In *Micro Electro Mechanical Systems*, 8-13 May 1994, San Diego, CA, USA, 273-278.
- [14] Yesin, K. B., Vollmers, K., and Nelson, B. J. (2006). Modeling and control of untethered biomicrobots in a fluidic environment using electromagnetic fields. *The International Journal of Robotics Research*, 25(5-6), 527-536.
- [15] Pawashe, C., Floyd, S., and Sitti, M. (2009). "Modeling and Experimental Characterization of an Untethered Magnetic Microrobot", *The International Journal of Robotics Research*, 28(8):1077-1094.
- [16] Hosseini, S., Mehrtash, M., and Khamesee, M. B. (2011). "Design, Fabrication And Control of a Magnetic Capsule-Robot for the Human Esophagus", *Microsystem technologies*, 17(5-7):1145-1152.
- [17] Hagiwara, M., Kawahara, T., Yamanishi, Y., Masuda, T., Feng, L., and Arai, F. (2011). "On-chip Magnetically Actuated Robot with Ultrasonic Vibration for Single Cell Manipulations", *Lab on a Chip*, 11(12):2049-2054.
- [18] Pelrine, R., Wong-Foy, A., McCoy, B., Holeman, D., Mahoney, R., Myers, G., and Low, T. (2012). "Diamagnetically levitated robots: An approach to massively parallel robotic systems with unusual motion properties". In *Robotics and Automation (ICRA)*, 14-18 May 2012, Saint Paul, MN, USA, 739-744.
- [19] Peyer, K. E., Zhang, L., and Nelson, B. J. (2013). "Bio-inspired Magnetic Swimming Microrobots for Biomedical Applications", *Nanoscale*, 5(4):1259-1272.
- [20] Katz, V. J. (1979). "The history of Stokes' Theorem", *Mathematics Magazine*, 52(3):146-156.
- [21] S. N. Bhatia ve d. E. Ingber, "Fabrication Methods for Microfluidic Chips, [http://www.nature.com/nbt/journal/v32/n8/fig\\_tab/nbt.2989\\_f1.html](http://www.nature.com/nbt/journal/v32/n8/fig_tab/nbt.2989_f1.html), 12 January 2017.
- [22] Pattern transfer, <https://www.memsnet.org/mems/processes/lithography.html>, 17 February 2017.
- [23] Mask illustration, [https://upload.wikimedia.org/wikipedia/commons/thumb/5/5e/mask\\_illustration.svg/2000px-mask\\_illustration.svg.png](https://upload.wikimedia.org/wikipedia/commons/thumb/5/5e/mask_illustration.svg/2000px-mask_illustration.svg.png), 19 February 2017.
- [24] Masks in Lithography, <https://www.ptb.de/cms/en/ptb/fachabteilungen/abt5/fb-52/ag-522/masken522.html>, 22 January 2017.
- [25] F. Chollet ve H. Liu, "A Short Introduction to MEMS, <http://memscyclopedia.org/document/intromems.pdf>, 27 December 2016.

## CURRICULUM VITAE

---

### PERSONAL INFORMATION

**Name Surname** : Ali Anıl DEMIRCALI

**Date of birth and place** : 29.01.1991, SAMSUN

**Foreign Languages** : English

**E-mail** : anildemircali1@gmail.com

### EDUCATION

DEGREE	DEPARTMENT	UNIVERSITY	DATE OF GRADUATION
Master	Mechatronics Engineering	Yildiz Technical University	2017
Undergraduate	Mechatronics Engineering	Yildiz Technical University	2015
High School	Science	Mustafa Kaynak Anatolian High School	2009

### WORK EXPERIENCE

Year	Corporation/Institute	Enrollment
2016-current	Kultur University	Teaching Assistant

2016-current	TUBITAK 1001 MicroRobot	Project Expert
2015-1 Month	YTU-PCB LABROTARY	Intern
2014-1 Month	Mercedes-Benz Turk A.S	Intern
2014-16 Months	Yildiz Technical University	Student Assistant
2013-1 Month	Ferro Dokum A.S	Intern



## **PUBLISHERMENTS**

### **Conference Papers**

1. Demircali A., Uvet H., Erkan K. (2017). "A High Accurate Positioning And Manipulation Technique for Untethered Microrobots". 3-7 May, Budapest, Hungary, ICENS
2. Uvet H., Demircali A., Kose T., Kahraman Y., Erkan K. (2017). "Highly Precise Micro-Robot Manipulation Techniques for Lab-on-a-Chip Systems". 3-7 May, Budapest, Hungary, ICENS
3. Aydin S., Demircali A., Uvet H. (2017). "Algorithm Analysis with the Help of Holographic Interferometry". 8-10 April, Ankara, Turkey, ICEEE
4. Abali B., Demircali A., Uvet H. (2017). "The Observation of Imperfections in Medical Implants by Holographic Interferometry and the Comparisons of These Observations to Other Methods". 8-10 April, Ankara, Turkey, ICEEE
5. Demircali A., Uvet H. (2017). "A study of Unmanned Glider Design, Simulation, and Manufacturing". 22-24 March, Prague, Czech Republic, CBUIC
6. Demircali A., Uvet H., Kahraman Y., Kose T., Sisu S., Erkan K. (2017). "Precise Positioning of Diamagnetically Levitated Micro Robot". 22-24 March, Prague, Czech Republic, CBUIC
7. Sisu S., Karatas N., Kose T., Demircali A., Uvet H. (2017). "Mikrorobot Kolu Tasarimi, Uretimi, Uygulamasi ve Nano Hassasiyette Konumlandırılması". 09-10 March 2017, İstanbul, Turkey, NANOKON
8. Demircali A., Esemen C., Yahsi F., Uvet H. (2016). "Planör Tipi Katlanabilir İnsansız Hava Aracı". 02-03 November 2016, İstanbul, Turkey, TORK

### **Projects**

1. Micro robotic arm design, production, and contactless manipulation with visual feedback (TUBITAK 1001)
2. Flapping Wing UAV Design, Simulation, and Manufacturing Inspired by Eagles Supported by The Scientific and Technological Research Council of Turkey (TUBITAK) (05/2016 - )
3. Precise Motion and tracking Control of a sphere ball on a hexapod(6x6) system
4. Design and Implementation of Non-Destructive Testing Device for Concrete Structures
5. Nonlinear Robotic 2 Link Arm Control via Adaptive, Robust, and Sliding Mode Simulations
6. Nonlinear Dynamic Magnetic Ball Suspension System via Backstepping Control

## **AWARDS**

1. High Honor Student
2. NANOKON 2017 - Best Article 2<sup>nd</sup> Price

